Space Sci Rev (2015) 195:199–256
DOI 10.1007/s11214-015-0175-6

MAVEN SupraThermal and Thermal Ion Compostion (STATIC) Instrument

J.P. McFadden[1] · O. Kortmann[1] · D. Curtis[1] · G. Dalton[1] · G. Johnson[1] · R. Abiad[1] · R. Sterling[1] · K. Hatch[1] · P. Berg[1] · C. Tiu[1] · D. Gordon[1] · S. Heavner[1] · M. Robinson[1] · M. Marckwordt[1] · R. Lin[1] · B. Jakosky[2]

Received: 6 August 2014 / Accepted: 11 June 2015 / Published online: 23 November 2015

Abstract The MAVEN SupraThermal And Thermal Ion Compostion (STATIC) instrument is designed to measure the ion composition and distribution function of the cold Martian ionosphere, the heated suprathermal tail of this plasma in the upper ionosphere, and the pickup ions accelerated by solar wind electric fields. STATIC operates over an energy range of 0.1 eV up to 30 keV, with a base time resolution of 4 seconds. The instrument consists of a toroidal "top hat" electrostatic analyzer with a 360° × 90° field-of-view, combined with a time-of-flight (TOF) velocity analyzer with 22.5° resolution in the detection plane. The TOF combines a −15 kV acceleration voltage with ultra-thin carbon foils to resolve H^+, He^{++}, He^+, O^+, O_2^+, and CO_2^+ ions. Secondary electrons from carbon foils are detected by microchannel plate detectors and binned into a variety of data products with varying energy, mass, angle, and time resolution. To prevent detector saturation when measuring cold ram ions at periapsis ($\sim 10^{11}$ eV/cm^2 s sr eV), while maintaining adequate sensitivity to resolve tenuous pickup ions at apoapsis ($\sim 10^3$ eV/cm^2 s sr eV), the sensor includes both mechanical and electrostatic attenuators that increase the dynamic range by a factor of 10^3. This paper describes the instrument hardware, including several innovative improvements over previous TOF sensors, the ground calibrations of the sensor, the data products generated by the experiment, and some early measurements during cruise phase to Mars.

Keywords MAVEN · Space plasma instrument · Composition · Calibrations · Electrostatic analyzer · Time-of-flight

1 Introduction

The MAVEN (Mars Atmosphere and Volatile EvolutioN) mission was designed to measure the loss of volatiles from the Mars atmosphere to space, and to combine these observations

✉ J.P. McFadden
mcfadden@ssl.berkeley.edu

[1] University of California, Space Sciences Laboratory, 7 Gauss Way, Berkeley, CA 94720, USA

[2] University of Colorado, LASP, 1234 Innovation Drive, Boulder, CO 80303, USA

with modeling to understand the histories of Mars' atmosphere and climate, liquid water, and planetary habitability. MAVEN will directly measure the current state of the upper atmosphere and ionosphere, its interactions with the solar wind, the rates of escape of atomic and molecular ion species to space, and the processes controlling these losses. MAVEN was launched Nov 18, 2013 and arrived at Mars on September 22, 2014. Its elliptical orbit of 6200 km × 150 km allows it to sample both the collisional ionospheric plasma and the accelerated pickup ions in the solar wind. In addition at several phases of the mission, periapsis is lowered to ∼ 125 km in order to sample down to the homopause during a week of deep-dip orbits. The nominal 4.5 hour orbital period, combined with orbital precession, variations in solar wind magnetic field direction, and the Mars orbit around the sun, provides a comprehensive sampling of the volatile ion and neutral losses as a function of local time, solar and solar wind conditions, latitude, and altitude (Jakosky et al. 2015).

In order to effectively model the loss of Martian ions, MAVEN needs to measure the source density of ions in the collisional lower ionosphere, the creation of a suprathermal tail of these ions as the spacecraft transitions above the collisional regime, and the eventual acceleration of these ions to escape velocity by solar wind electric fields and other processes. These measurements will be provided by the SupraThermal And Thermal Ion Compostion (STATIC) instrument described in this paper. STATIC is mounted on the Articulated Payload Platform (APP), a 2 m boom which directs STATIC's field-of-view into the ram direction at periapsis (Fig. 1). The APP also points the Neutral Gas and Ion Mass Spectrometer (NGIMS, Mahaffy et al. 2015) which provides high-mass-resolution composition in the dense, collisional ionosphere. At higher altitudes, the APP orientation is time shared between STATIC and the Imaging UltraViolet Spectrometer (IUVS, McClintock et al. 2015). On orbits when STATIC has priority, the APP is oriented to optimize STATIC's ability to detect Martian pickup ions (Lundin et al. 1990). MAVEN carries several other instruments with overlapping plasma sensitivity. These include the Solar Wind Ion Analyzer (SWIA, Halekas et al. 2013), the Solar Wind Electron Analyzer (SWEA, Mitchell et al. 2015) and the Langmuir Probe and Wave experiment (LPW, Andersson et al. 2015). STATIC data analysis will also utilize observations from the Magnetometer (Connerney et al. 2015) for contextual, pickup ion and related wave analysis, and the Solar Energetic Particle experiment (SEP, Larson et al. 2015) for determining background from penetrating radiation.

The science objectives that shaped STATIC's design are derived from atmospheric loss mechanisms that involve ionization and ion chemistry in the upper atmosphere, ion transport and heating, and eventual ion loss via bulk transport and pickup mechanisms. The Martian ionosphere is a complex laboratory of molecular and atomic chemistry and photo-chemistry (Matta et al. 2013) with primary energy inputs from solar radiation, the solar wind, solar energetic particles, pickup ion sputtering, and meteoric dust. Although neutral atmosphere and ionospheric modeling is quite complex and sophisticated (Fox 2009; Matta et al. 2013; Gonzalez-Galindo et al. 2013), observational tests of the models are few. Viking observations using retarding potential analyzers (RPAs) have provided the primary in situ measurements of ionospheric composition and density with altitude (Hanson et al. 1977), with significant differences in ionospheric structure observed for two descents. The structure inferred from these data is rather limited not only because the observations were restricted to a single solar zenith angle, but also because RPAs have difficulty resolving minor ions below the O_2+ ram energy.

Radio occultation experiments on the Mariners (6, 7, 9), Mars (2, 3, 4, 6), Viking, Mars Global Surveyor and Mars Express (MEX) have also probed the ionosphere. The MARSIS instrument on the MEX mission has provided additional estimates of the ionospheric density profiles using radar sounding (Gurnett et al. 2008), but without composition the model

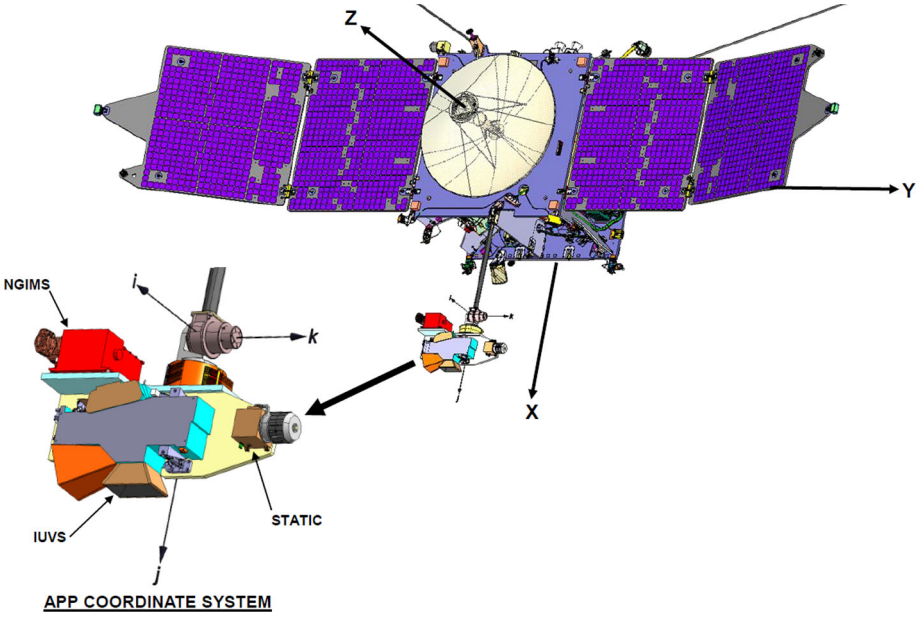

Fig. 1 The STATIC sensor is mounted to the Articulated Payload Platform (APP) attached to a 2 m boom along with the NGIMS and IUVS sensors. The APP provides optimal orientation for STATIC to view ram and pickup ions. Ram direction is opposite to the i-vector on the APP

testing is incomplete. STATIC and NGIMS will provide high spatial resolution ($\sim$ 10 km) ionospheric composition versus altitude ten times each day, with STATIC also resolving flows (ion winds) and ion temperatures. Between these two instruments, the primary unresolved species will be neutral hydrogen. However, STATIC can measure the cold ionospheric hydrogen ions (H^+, H_2^+ and H_3^+) which provides a test of Martian ionospheric chemistry including the production of hydrogenated ions such as OH^+, HCO^+, ArH^+, and HCO_2^+ (Matta et al. 2013). These measurements could be used as a proxy for modeling neutral hydrogen (H, H_2) which is important for atmospheric chemistry and transport, and quantifying various loss mechanisms (Fox 2003).

At the interface between the ionosphere and solar wind, a plethora of acceleration and mixing mechanisms act that enhance the atmospheric loss processes. Bulk escape processes associated with Martian crustal fields (Brain et al. 2006), trans-terminator flows (Fraenz et al. 2010), shear flows at boundaries (Penz et al. 2004), and the Martian magnetotail (Dubinin et al. 1993; Fedorov et al. 2006) may provide significant ion loss. Bulk escape may be the primary source of plasma into the Martian plasma sheet, whereas ambipolar fields may be the primary driver for polar wind outflows of protons into the tail lobes (Dubinin et al. 2011) and from other regions magnetically 'open' to interplanetary space. Magnetic reconnection may play a role in these loss mechanism (Eastwood et al. 2008; Dubinin et al. 2012). STATIC will provide the primary measurements of bulk ionospheric losses for the MAVEN mission, using composition to identify ionospheric components and resolving the transition from cold ionospheric ions to heated outflows.

In addition to processes that mix or inject ionospheric ions into the solar wind, photoionization, solar wind electron impact, and solar wind proton charge exchange in the high altitude atmosphere and neutral corona can result in the production and escape of pickup

ions. Due to the draping of the interplanetary magnetic fields (IMF) over the Martian ionosphere, solar wind electric fields in the vicinity of the planet are determined to first order by the IMF clock angle. The result is a preferred pickup ion acceleration that forms a crest or plume of newly created ions that flow out from the hemisphere aligned with the interplanetary electric field. These asymmetric features were first observed by Phobos (Lundin and Dubinin 1992) and later quantified by Mars Express (MEX, Barabash et al. 2006) which provided a more complete set of measurements. The MEX Ion Mass Analyzer (IMA) provided compositional information on losses, however, those measurements were generally limited by time resolution and by a lower energy cutoff (> 10 eV). Several estimates of total ion loss rates have been made (Lundin et al. 1990; Carlsson et al. 2006; Barabash et al. 2007; Fang et al. 2010; Ramstad et al. 2013) with significant variations. The composition of escaping plasma measured with MEX IMA indicates comparable outflows of O+ and O_2+, inferred by model fitting to the to the heavy ion mass peak. STATIC's mass resolution provides a cleaner separation of O+ and O_2+ to quantify losses, and its higher time resolution resolves the structure in the outflows. For more tenuous ion outflows, such as C+ and CO_2+, fitting similar to that performed for IMA may be required. STATIC is also able to resolve cold ion outflows to much lower energy (< 1 eV).

In order to characterize the Martian ionosphere and its loss mechanisms, STATIC measures the distribution function and composition of ions from as low as ~ 0.1 eV at periapsis, to 30 keV at apoapsis. Through the use of mechanical and electrostatic attenuators, STATIC handles a wide range of ion populations from cold, nearly-stationery ionospheric plasma with densities as high as 10^5 cm^{-3}, to relatively fast but tenuous pickup ions ($\sim 10^3$ eV/cm^2 s sr eV) in the solar wind. During routine on-orbit operations, STATIC adjusts its energy range (0.1–50 eV at periapsis, 0.1–500 eV in the upper ionosphere, and 1–30,000 eV in the solar wind) and time resolution (highest at periapsis) commensurate with science goals and particle event rates during an orbit. STATIC's basic measurement cadence is 4 s, however data transmission limitations prevent the bulk of its 4-dimensional measurement array (energy-phi-theta-mass) from being downlinked. Instead the Particle and Fields Data Processing Unit (PFDPU) builds a set of telemetry packets that maintain 4 second resolution in some measurement dimensions, while averaging larger dimensional data arrays (3-D and 4-D) in time. A subset of higher time resolution ('burst mode'), 3-D or 4-D arrays can also be downlinked, depending on the availability of telemetry.

The PFDPU provides the interface between the MAVEN spacecraft bus and the seven instruments in the Particle and Fields instrument suite. The PFDPU provides a programmable layer for instrument operations and monitoring, and a flexible data flow system that adjusts for downlink limits (Mars' proximity to the Earth) while maximizing data throughput. The PFDPU controls power to STATIC, loads its look-up tables (LUTs), controls its high voltage turn-on, monitors housekeeping, 'safes' the instrument if currents are out of range, commands STATIC into various science modes selecting energy range and data resolution, collects STATIC's data packets which it averages and sorts into telemetry packets for transmission to the ground, monitors STATIC's event rates, and controls STATIC's attenuators to prevent detector saturation. The PFDPU uses a serial data interface with clock, command and data lines to control STATIC, along with +28 V power and mechanical attenuator power. The 'High Voltage On' sequence includes a pair of enable commands that are only uploaded after launch to prevent accidental HV turn-on during ground testing. Science data averaging and compression is flexible and includes 19 bit to 8 bit raw data compression (lossless under 32 counts, and < 3 % errors for larger values), data averaging into 21 separate science telemetry packet types with programmable $2^N \times 4$ s averaging, and lossless Huffman-encoding that provides data compression factors between two and five. In addition,

the PFDPU directs high-rate 4-dimensional science data products into Archive memory (~ 2 weeks storage) where a subset can be later retrieved by ground command after the standard data have been examined. STATIC also receives support from the MAVEN spacecraft bus which monitors STATIC's temperature, provides survival heater power, actuated the one-time cover mechanism that sealed STATIC from contamination at launch, and controls the APP orientation.

MAVEN includes several other instruments with overlapping sensitivity which will provide data for cross-calibration once the spacecraft reaches Mars. These instruments include the SWIA (Halekas et al. 2013), which will provide non-compositional information about the hot plasma, and NGIMS (Mahaffy et al. 2015) which can provide neutral and ion high-mass-resolution composition in the dense, collisional ionosphere. STATIC observations will also be cross-calibrated with plasma densities determined by SWEA (Mitchell et al. 2015) and LPW (Andersson et al. 2015). STATIC's inflight calibration data analysis will also utilize observations from the other MAVEN sensors including the Magnetometer (Connerney et al. 2015) for pickup ion analysis, and LPW for analyzing ion heating and spacecraft potential.

2 Instrument description

The STATIC instrument uses an electrostatic analyzer (ESA) and time-of-flight (TOF) velocity analyzer to resolve ion energy per charge, direction, and velocity per charge. When combined with knowledge of charge state (nearly all ions at Mars are singly charged except solar wind alphas), STATIC resolves the distribution function of all major ion species in the Martian plasma. As shown in the block diagram of Fig. 2, ions are selected for energy/charge by a top-hat electrostatic analyzer, then accelerated by -15 kV into the TOF analyzer. Ions entering the TOF penetrate Start and Stop carbon foils, producing secondary electrons that are deflected and accelerated to microchannel plate (MCP) detectors. The short delay (10–100 ns) between Start and Stop signals as the ion transits the 2 cm gap provides information on the accelerated ion's velocity. The detection electronics use discrete anode delay line techniques to determine both event location and time-of-flight. The energy analyzer also includes electrostatic deflectors at the entrance which expand the nominal $360^\circ \times 6^\circ$ field-of-view (FOV) to $360^\circ \times 90^\circ$. The dynamic range of the instrument is expanded by a both mechanical and electrostatic attenuators located near the ESA entrance aperture. STATIC differs from previous TOF mass spectrometers both in its compact design (~ 3.3 kg), its large dynamic range in both energy and particle flux, and in its simplified electronics that does not require floating detectors at the TOF acceleration potential of -15 kV. Details of the instrument subsystems are described below.

STATIC's toroidal top-hat electrostatic analyzer geometry (McFadden and Carlson 1998) was designed for the Cluster mission (Rème et al. 1997), was first utilized on the FAST satellite (Klumpar et al. 2001), and was later included in the reconfigured Cluster II mission. Top-hat designs provide large geometric factor, large field-of-view, and moderate energy resolution (dE/E ~ 15 %) while maintaining good optical imaging of particles onto the analyzer exit plane (Carlson and McFadden 1998). For typical spherical electrostatic analyzers (ESAs), fringing field aberrations at the entrance aperture result in optimal ion focusing after about 75° deflection within the analyzer. In order to incorporate TOF optics and optimize particle throughput, it is desired to shift the electrostatic focal point past the exit of a 90° deflection analyzer. To shift this focal point, a toroidal analyzer design was chosen that moves

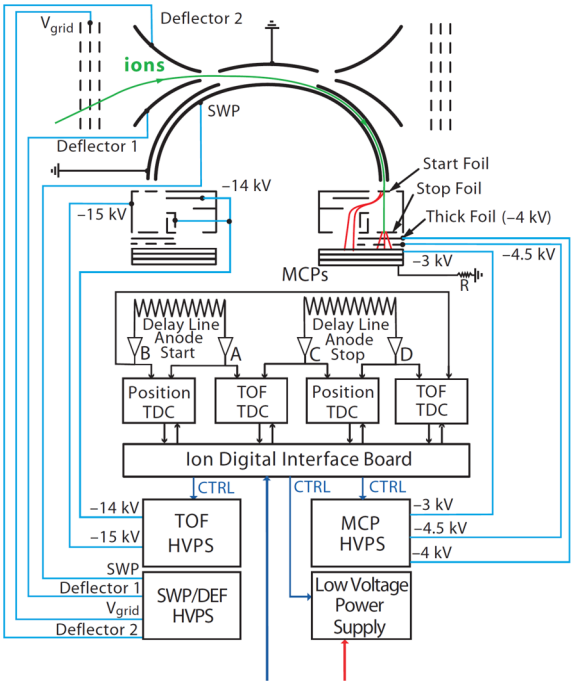

Fig. 2 Block diagram of the STATIC sensor. Ions are selected for direction by deflectors, and for energy/charge and direction by a toroidal top-hat electrostatic analyzer (ESA). The sensor includes an electrostatic attenuator (Vgrid) and a mechanical attenuator (not shown). After passing through the ESA, ions are accelerated by −15 kV into the time-of-flight (TOF) velocity analyzer where they pass through Start and Stop ultra-thin carbon foils. Secondary electrons from the Start foil (*red*) are deflected by the −14 kV supply (actually −13.75 kV, or +1.25 kV relative to the foil potential) and focused to an inner ring of the microchannel plate (MCP) detector, while Stop foil secondary electrons (*red*) are accelerated to the thick foil with enough energy to allow them to pass through and strike the MCP detector. MCP charge pulses are split on discrete delay-line anode chains, amplified, and fed into four time-to-digital converters (TDC) which determine event position and the time-of-flight in the 2 cm gap between Stop and Start carbon foils

the focal point to just past the analyzer exit, where the ions are accelerated by the −15 kV TOF potential.

Figure 3 shows the mechanical parameters and a cut-away design of the STATIC sensor, and Table 1 summarizes instrument parameters. The inner hemisphere of the ESA can be biased from 0 to −4 kV, providing energy selection up to ∼ 30 keV. Outside the analyzer are a pair of deflectors which can be biased up to +4 kV providing +/ − 45° of FOV deflection at energies up to ∼ 4 keV, with smaller deflections at higher energy. To reduce contamination by scattered particles and UV sunlight, the outer surfaces of the ESA were scalloped and all internal surfaces were coated with Ebanol-C. Leakage fields from the TOF high voltage (HV) into the ESA were minimized by a pair of grids at the ESA exit. Leakage fields, as discussed in McFadden et al. (2008), result in variations in the geometric factor at low energy with a single grid. Remaining fringing fields at the exit grids (90 % open area) produce an energy-dependent transmission through these grids, with the lowest energies having ∼ 20 % higher transmission.

STATIC was designed with two attenuators to increase its flux dynamic range by three orders of magnitude. A mechanical attenuator (Fig. 4) is located just outside the ESA aperture,

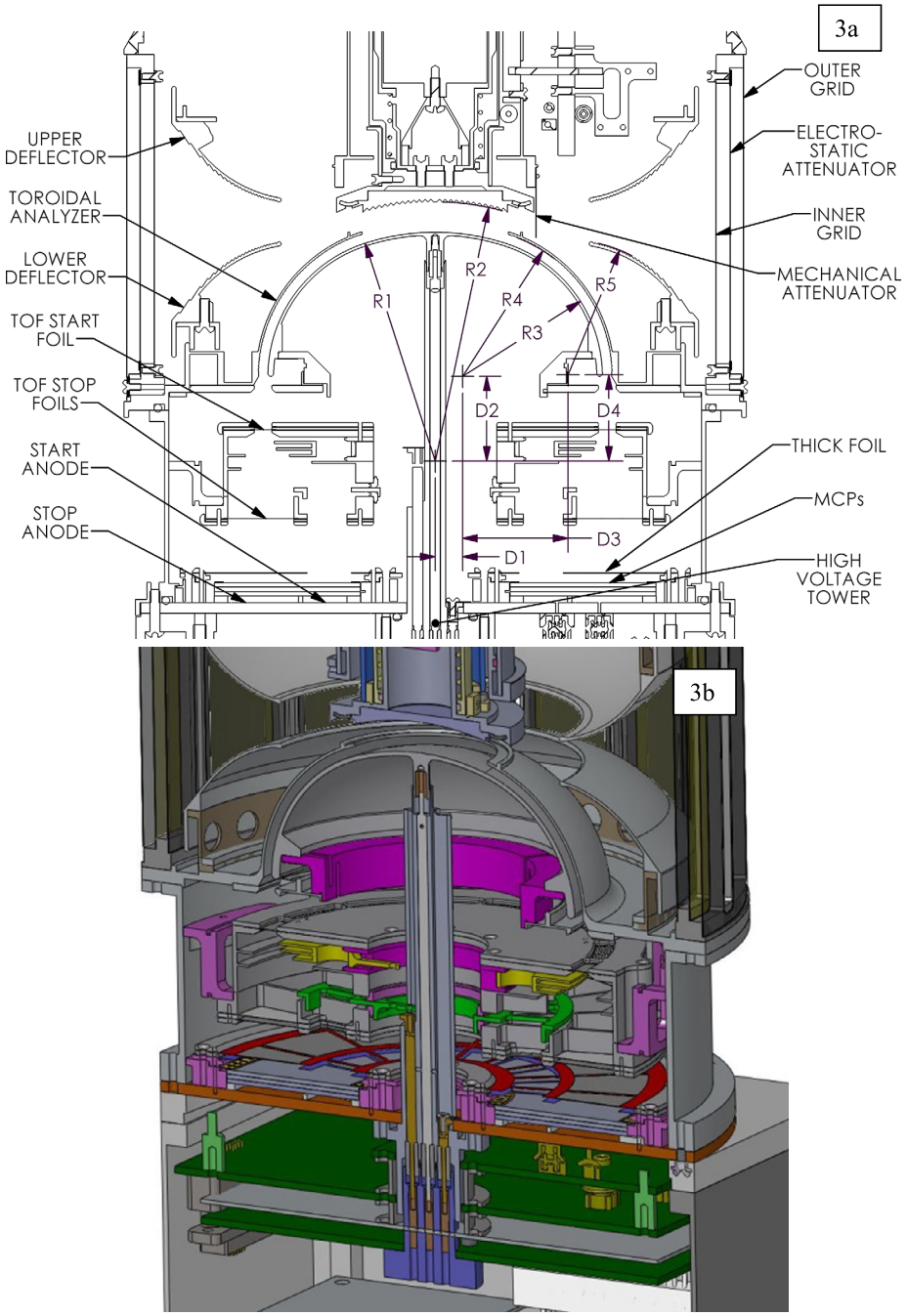

Fig. 3 (**a**) STATIC mechanical cross section, dimension in mm, R1 = 51.90, R2 = 58.78, R3 = 31.68, R4 = 33.77, R5 = 30.63, D1 = 6.22, D2 = 19.24, D3 = 23.88, D4 = 19.54, (**b**) Cutaway of STATIC sensor

Table 1 STATIC instrument specifications

Parameter	Value	Comments
Electrostatic Analyzer		Toroidal top-hat
$\Delta R/R$	0.064	37.5 mm inner hemisphere radius
Analyzer constant	7.8	Energy/Voltage, 0 to 4 kV HV sweep
Deflector Constant	6.4	Deflector/(Inner Hemisphere) voltage ratio for 45° deflection
Energy Range	0.1 eV to 30 keV	
Analyzer Energy Resolution	16 %	$\Delta E/E$ measured
Measurement Energy Resolution	11 %–16 %	Ram and Pickup Modes
Energy Sweep Rate	0.25 Hz	64 energies in 4 sec
Deflector Sweep Rate	16 Hz	16 deflection steps each 61 ms
Instantaneous Field of View	360° × 6° FWHM	Planar w/o deflection
Field of View with Deflection	360° × 90°	Conical
Simulation Geometric Factor	0.016 cm^2 sr E	Excluding grids/posts/efficiencies
ESA Geometric Factor	0.0031 cm^2 sr E	Including grids/posts at high energy
	0.0044 cm^2 sr E	Including fringing fields at low energy
ESA-TOF Total Sensitivity	0.0015 cm^2 sr E	Highest for molecular H_2^+
	0.0010 cm^2 sr E	Nominal for H^+ He^+ N^+ N_2^+ at low energy
	0.0005 cm^2 sr E	CO_2^+ has lowest sensitivity
Attenuation Factors	1, 10, 100, 1000	Selectable attenuation of cold ram ions
Time-of-Flight Analyzer		
Post ESA Acceleration	−15 kV	
Carbon Foil Thickness	< 1.0 μg/cm^2	Nominal, varies with anode angle sector
Carbon Foil grid frames	333 lines/inch	∼ 62 % transmission
TOF gap between Start/Stop	2.00 cm	+/ − 0.005 cm
Proton time of flight	12 to 7 ns	0 to 30 keV initial energy
Anode detection resolution	22.5°	
Thick Foil	500 nm kapton	50 nm Al coatings
MCP Detectors	Z-stack	
Anode Rejection	∼ 25 %	Cross talk events rejected in electronics
Start Efficiency	60 %–80 %	Mass dependent, excludes grid frame losses
Stop Efficiency	20 %–60 %	Mass, molecular, & energy dependent includes grid frame loss (∼ 62 % transmission)
Electronics		
Preamp shaping	8 ns	
CFD timing jitter	< 1 ns	
TDC resolution	< 0.2 ns	
Accumulation time	3.8 msec	No accumulation during energy changes
Accumulation intervals per sweep	1024	64 energy × 16 deflection intervals
Typical Data Products		
Energy spectra	64E × 2M	4 sec resolution
Energy-Mass spectra	32E × 64M	4 sec resolution
Energy-Deflection spectra	32E × 16D	4 sec resolution
Energy-SolidAngle spectra	16E × 64Ω	4 sec resolution
Energy-Mass-Deflector	32E × 32M × 8D	16 sec resolution, Ram Mode
Energy-Mass-SolidAngle	16E × 16M × 64Ω	32 sec resolution, Conic Mode
Energy-Mass-SolidAngle	32E × 8M × 64Ω	128 sec resolution, Pickup Mode
Mass Histogram Array	1024 TOF bins	4 to 256 sec resolution, 1 ns = 5.8 bins

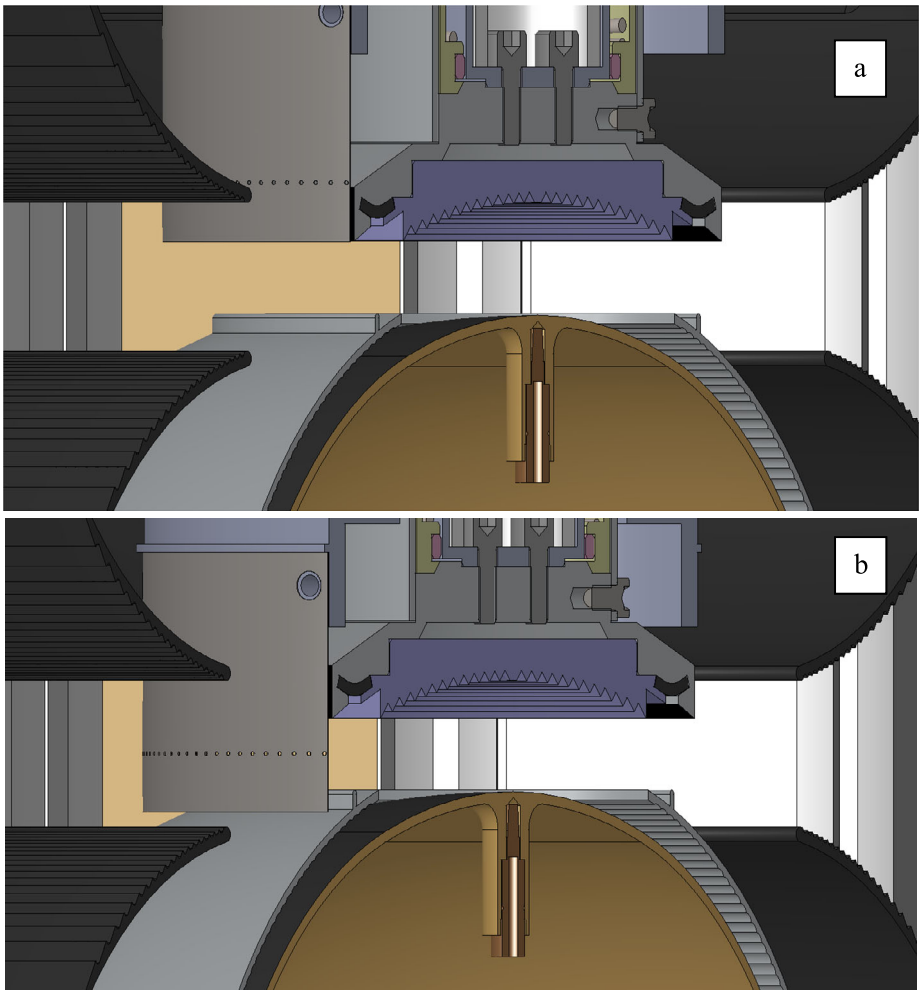

Fig. 4 Cut-away of STATIC's mechanical attenuator showing the (**a**) open and (**b**) closed configuration. The mechanical attenuator uses a set of pin-holes to reduce the flux in the ram direction by a factor of 100. The attenuator only extends over 180° of the 360° field of view. At launch, the ESA top-cap (*purple*) sits against the outer hemisphere on a conducting gasket and the attenuator is caged to prevent damage under vibration

and is an integral part of the aperture opening mechanism. The STATIC entrance aperture is closed and the sensor is sealed under nitrogen purge at launch. A conductive gasket provides a compliant seal that prevents both detector contamination and acoustic damage to the carbon foils during launch and early orbit. Several weeks after launch, a one-shot TiNi actuator opens the cover allowing the sensor to fully outgas. Until the aperture is opened, the mechanical attenuator is caged to prevent damage during vibration, and its circuits are electrically disabled. Once opened, the mechanical attenuator, utilizing nano-muscle shaped metal alloy actuators, can move a multi-pinhole attenuator into and out of the main aperture (Fig. 4). The pinholes reduce the flux by a factor of 100 centered on the ram direction. The attenuator only covers half the sensor's 360° FOV, leaving the anti-ram direction at full sensitivity. The mechanical attenuator is under software control which monitors the sensor's

counting rates and actuates the attenuator when a threshold count rate has been exceeded for a programmable time interval. To assure complete thermal relaxation of the nano-muscle actuators between motions, and thereby prevent stressing the actuators, software enforces a 5 minute timeout between motions.

STATIC also contains an electrostatic attenuator located at the outer surface of the analyzer housing. The analyzer support structure contains 16 primary entrance windows, each containing three 92 % transmission grids. These grids serve a dual purpose, reducing leakage fields from the deflectors and providing an electrostatic shutter to close the windows to low energy ions. The inner grid of the triplet grids can be biased at up to +28 V, preventing ions less than $\sim$ 18 eV from entering the sensor. When the electrostatic attenuator is activated, ions can still enter the sensor through a set of 16 slits in the posts that support the upper housing (Fig. 5a). The slits have 10 % of the open area of the primary entrance windows including grid attenuation. The slits are located at a radius that guarantees near uniform response as a parallel beam is rotated in azimuth (Fig. 5b) about the symmetry axis, with adjacent slits picking up the beam as it rotates out of any initial slit aperture. The combined mechanical (M) and electrostatic (E) attenuators provide four different geometric factor states: "ME = 00"-no attenuation, "ME = 01"-factor of 10 attenuation, "ME = 10"-factor of 100 attenuation, "ME = 11"-factor of 1000 attenuation. Attenuation is only needed in the high ram fluxes at periapsis, so a typical orbit will cycle to maximum attenuation and back to no attenuation once an orbit. Hysteresis is built into the software algorithm to prevent rapid transitions. These factor-of-10 changes in sensitivity guarantee relatively good statistics for particle data while simultaneously preventing detector and electronic saturation.

Unlike most TOF analyzers that use a single Start carbon foil and require ions to strike a STOP detector that is often floated at the TOF's HV, STATIC uses carbon foils to generate both START and STOP signals. This design simplifies the detection electronics by allowing the MCP HV supply to be independent of the TOF's −15 kV supply. In order for CO_2^+ ions, the heaviest ions expected at Mars, to penetrate two carbon foils with adequate efficiency, STATIC was required to use ultra-thin foils (< 1 μg/cm^2) and have a post-acceleration voltage of −15 kV. TOF optics simulations shown in Fig. 6 illustrate the path of secondary electrons produced on the Start foil. The TOF HV supply (0 to −15 kV, programmable), has a secondary tap with 11/12 of the full voltage (−13.75 kV), which produces the deflection optics that focus Start electrons to a smaller radius at the exit of the TOF analyzer. Simulations were performed with 3-D optics to guarantee that out-of-plane motion of electrons retained the 22.5° resolution of the detection anodes. The TOF optics has 16-fold symmetry (22.5°) and includes baffles to prevent scattered ions from crossing over to adjacent sectors. Start and Stop electrons are accelerated by $\sim$ 12 kV before striking the MCP detectors. Start and Stop foils are shielded by grids to suppress field-emission by small tears in the foils.

A potential problem with using Start and Stop carbon foils to decouple the HV electronics, is the creation of ghost peaks in the mass spectra. Ghost peaks are signals outside the nominal mass peak. They are generally caused by the lack of a valid Stop pulse, followed by a delayed Stop due to the same particle. Ghost peaks are especially prominent in isochronous TOF instruments (Young et al. 2004). For the STATIC design, ions have a finite probability ($\sim$ 20–30 %) of penetrating the Stop carbon foil without producing a Stop electron. These particles could produce a delayed Stop signal, and therefore an invalid TOF, should the particle strike the MCP detector or reflect and strike the carbon foil a second time. Most of the particles emerging from the Stop foil are neutrals ($\sim$ 90 %) and could therefore reach the MCP detectors producing a delayed Stop pulse. Smaller ghost peaks could result from ions emerging with negative charge and accelerating to the MCP detector, or from ions emerging

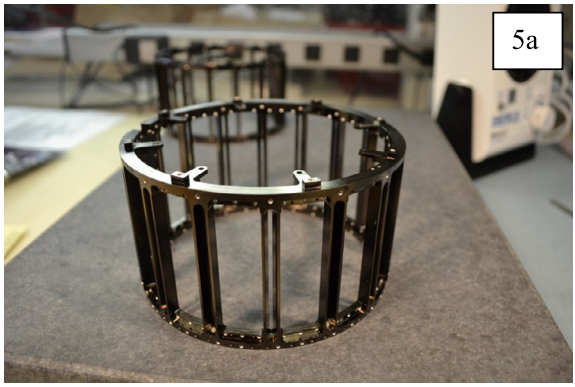

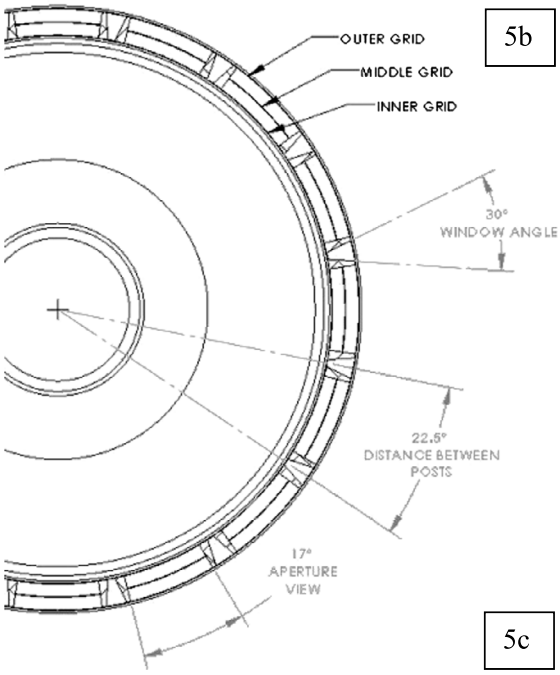

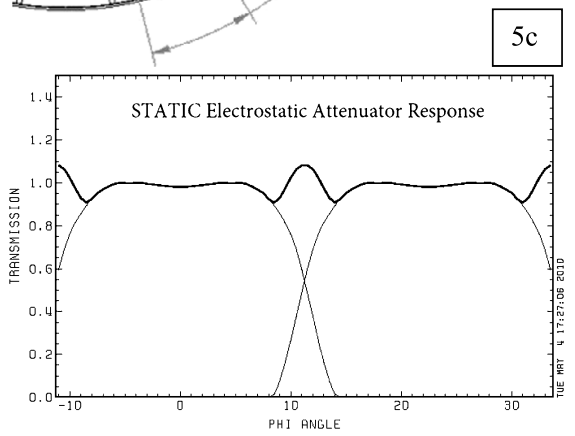

Fig. 5 (**a**) STATIC outer housing showing entrance slits in the support posts between the primary entrance apertures, (**b**) cut-away of STATIC outer housing illustrating the geometry of the support posts, (**c**) simulation showing response overlap of two slits illustrating a relatively uniform total responses (*thick line*)

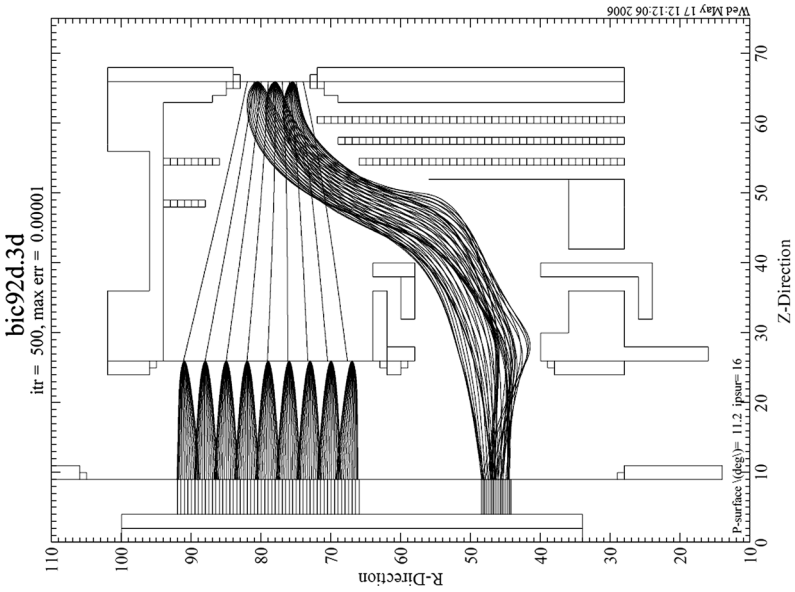

Fig. 6 3-D simulation of STATIC time-of-flight (TOF) velocity analyzer illustrating the trajectory of secondary electrons produced in the Start (Z = 67) and Stop (Z = 26) carbon foils. *Straight lines* are ion trajectories. All *other curves* are secondary electron trajectories for a variety of initial velocities. Only a single internal bias voltage is required to focus the Start foil secondary electrons to the inner radius of the detector

with positive charge, reflecting, and producing a delayed strike on the carbon foil. A method of suppressing ghost peaks is essential for a clean separation of mass peaks.

For STATIC the ghost peak problem was solved by the introduction of a thick foil (aluminized kapton) located just above the Stop portion of the MCP detectors. The kapton was modeled with TRIM simulations and chosen to be thick enough to stop 45 keV protons while still allowing the bulk of Stop electrons to reach the detectors. The thick foil is nominally floated between −4 kV and −5 kV guaranteeing that Stop electrons have enough energy (> 10 keV) so the majority penetrate the thick foil. Electron penetration of the thick foil was modeled with CASINO, and transmission as function of energy is shown in Table 2. All neutrals and negative ions with mass larger than protons are easily stopped by the thick foil. In addition low mass particles, such as H and He, that lose less than 4 keV to the carbon foils and emerge as positive ions (∼ 5 %), will also strike the thick foil rather than reflecting, therefore avoiding tenuous ghost peaks at higher mass. As will be shown, molecular H_2^+ does produce a ghost peak. Heavier ions should produce some delayed signals, however these are negligible as will be shown later. A more general discussion of ghost peaks, background and noise the mass spectra will be addressed in Sect. 3.

The carbon foils used in STATIC were obtained from ACF-Metals and came mounted on both glass and mica slides. They were floated using a standard warm-water surfactant solution and captured on stainless frames with grid mesh attached. After mounting, the foils were dried, then baked to increase bonding to the grids. Several grid styles were tried including higher-transmission hexagonal grids and standard 333 line/inch mesh. Although ultra-thin carbon foils were found to survive vibration testing for some hexagonal grids, lower grid yields combined with schedule constraints led to selection of 333 line/inch rectangular grids for STATIC. Grids were evaluated before and after vibration testing using an optical scanner

Table 2 Thick foil transmission of TOF Stop Electrons

Initial energy (keV)	% transmission	Average energy (keV)	Peak energy (keV)	Max energy (keV)
5	0			
6	3	1.19	1.27	1.91
7	31	2.86	3.23	3.88
8	61	4.48	4.99	5.34
9	72	5.98	6.52	6.66
10	82	7.30	7.82	7.90
11	87	8.56	9.02	9.09
12	91	9.79	10.2	10.2
13	93	11.0	11.3	11.3

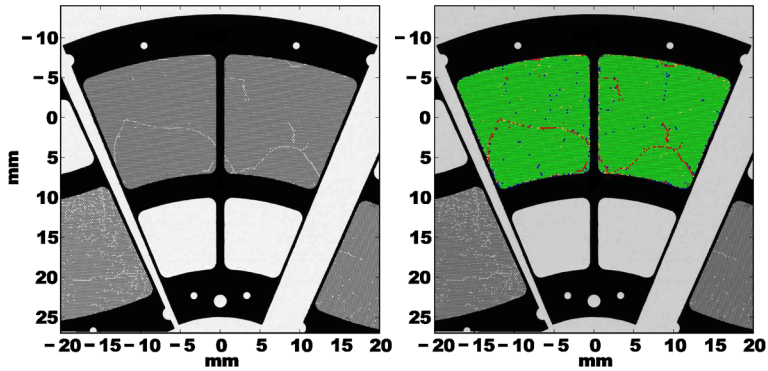

Fig. 7 Optical scan of a 200 hex (200 μm cell spacing) STOP foil (*left*) and a false color software evaluation of the transmitted light. *Red* identifies holes and *blue* identifies double thick foil. Double thick foil pixels are caused by fragmentation of the foils during mounting. Individual grid cells were automatically evaluated for transmission coverage and compared before and after a vibration qualification

and pixel evaluation software. Figure 7 illustrates the evaluation method for a 200 hex grid (200 μm cell spacing) showing the scanner image and a false color automated evaluation of pixels. The software could identify both holes and instances of pixels with double foils due to fragmentation of foils during mounting. Foils were evaluated for coverage prior-to and after a vibration qualification test. The software also provided an estimate of foil thickness which could be compared with those from ACF-Metals. The foil selection process also included testing in a TOF unit where actual energy loss could be evaluated from shifts in the mass peaks. Final foil selection was based on both foil thickness and foil coverage (> 90 %, most with ~ 95 %).

STATIC detects the Start and Stop foil electrons with Z-stack 40:1 (length:diameter ratio) MCP detectors whose gain is nominally ~ 2–3×10^7. The MCP bias voltage is software controlled and gain is monitored using an adjustable threshold in the detection electronics. Charge pulses are collected by 16 Start and 16 Stop discrete anodes. The Start and Stop anodes form two independent anode chains linked by 2 ns discrete delay line chips. Charge pulse events split and propagate to both ends of the delay line where they feed discrete component preamplifiers that contain compensation for uniform gain over temperature. The four preamplifiers shape (~ 7 ns) and feed these signals to the time-

to-digital-converter (TDC) board which contains constant fraction discriminators (CFDs) with sub-nanosecond timing. The four CFD timing outputs, TA TB TC TD, are used to evaluate event time-of-flight (TDC1 = TA-TC and TDC2 = TB-TD) and event position (TDC3 = TA-TB and TDC4 = TC-TD). Redundant position determination allows rejection of events where Start and Stop location do not match (due to foil electron scattering) and redundant TOF outputs allow selection of the timing circuit with the smallest propagation delay, and therefore slightly better timing resolution. Timing signals of the CFDs are digitized using discrete-component TDC electronics that use a constant current source to charge a capacitor for an interval between pulses. This charge is then measured with four ADCs, which operate in parallel and are read by the Digital Interface Board (Fig. 2). Timing events are 10 bits (0–1023) with a full range measurement of $\sim$ 176 ns for TOF and $\sim$ 59 ns for anode position.

The Digital Interface Board (DIB) controls the TDC event readout and electronics deadtime, determines event validity, collects various event rates and raw events for diagnostics, sorts valid events into several data arrays with varying resolution in a mass-energy-direction array, and sends collected data to the Particle and Fields Digital Processing Unit (PFDPU). For event compression in the mass dimension (TOF), the DIB utilizes a pseudo-log TOF compression from 1024 to 256, followed by a mass-look-up-table (MLUT) to compress 256 to a more moderate 64 bin pseudo-logarithmic mass array. MLUTs are 256-TOF $\times$ 64-Energy arrays so that the mapping can account for variations in TOF with initial ion energy. For some final data products, these 64 mass bins are further compressed by factors of 2 in order to fit into the STATIC data allocation. The DIB also controls the sensor energy and deflector sweeps, collects housekeeping, controls HV, and includes a test pulser for electronics testing. The test pulser circuit provides variable Start and Stop test pulse amplitudes, variable Start-Stop time delays, and variable counting rates that can be synced to energy sweeps rates. This variability allows a complete checkout of the low voltage electronics without HV. The DIB includes a daughter card with an FPGA (field programmable gate array) that controls the sensor. The daughter card allowed flexible testing with inexpensive, reprogrammable FPGAs during sensor development, prior to burning the flight FPGA.

STATIC contains two HV boards which provide 9 high voltages and one low voltage, all controlled by the DIB. The TOF-MCP HV board generates voltages for the TOF analyzer (-15 kV, -13.75 kV) and the MCP-Thick Foil-Grid stack (programmable to -3.4 kV, -4.6 kV and -5.1 kV). The Grid HV output was included in the design to suppress secondary electrons from the MCP side of the thick foil, but was deemed not needed for the final configuration. The thick foil was ultimately attached to the Grid HV tap to increase the gap between the TOF analyzer and the thick foil. For ground calibrations and early operations the MCPs and thick foil were set at -2.7 kV and -4.0 kV, respectively. The Sweep (SWP) HV board generates HV for the ESA inner hemisphere (0 to -4 kV), the two deflectors (0 to $+4$ kV) and a low voltage for the attenuator grid (0 to $+28$ V). SWP HV electronics utilize Amptek HV801 opto-couplers to generate fast sweeps from a pair of raw supplies ($+4.5$ kV and -4.5 kV). To meet the low energy requirement, we used the LTC2054 zero drift OpAmps which have only ~ 1 μV input offset voltage. In addition, the sweep/deflector HV supplies included circuitry for monitoring changes in OpAmp offsets (due to radiation), and circuitry for correcting for any changes during the mission. It is this ability to monitor OpAmp drift allows STATIC to have a reliable dynamic energy range of 3×10^5. Sweep DAC dynamic range is achieved with a pair of DACs, where the first DAC controls the reference voltage for the second DAC. The TOF, MCP and Sweep high voltages are fed to the sensor with a custom-designed connector on the sensor's center axis (see Fig. 2). To prevent capacitive cross-talk to the inner hemisphere voltage (required to be extremely stable

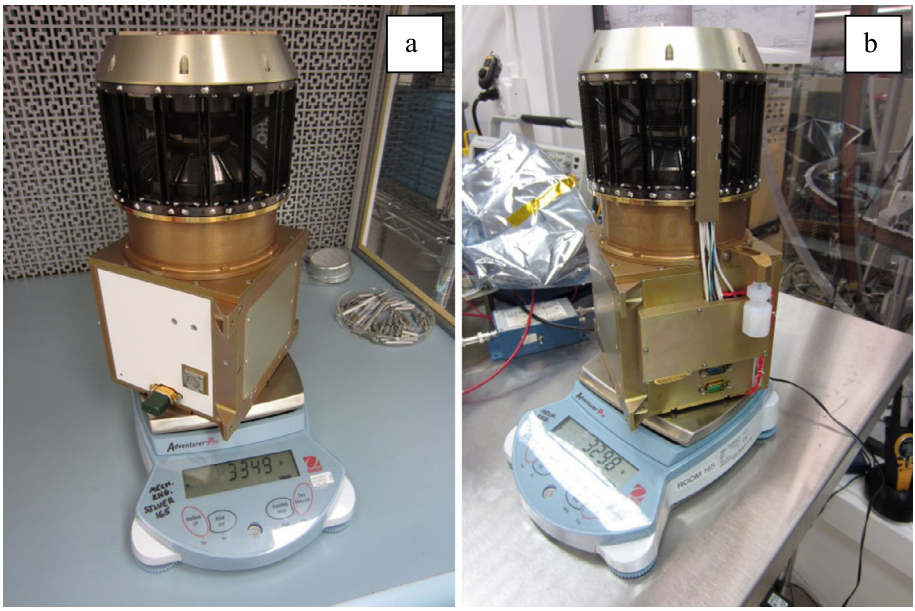

Fig. 8 STATIC sensor. *Left* pic shows the HV enable plug and vent hole. *Right* pic shows the purge connection, electrical interface, and harness to the deflectors and attenutor/cover actuators. Harness blocks anode 12 entrance window. The mass difference was due to additional bracing added to the electronics box

to resolve < 1 eV ions) from the surrounding HV pins, the TOF and MCP HV outputs were heavily filtered.

The final board in the STATIC assembly is the Low Voltage Power Supply (LVPS). It receives isolated and regulated $+28$ V from the PFDPU. The LVPS generates all the internal voltages for the sensor: $+5$ VD, $+3.3$ VD, $+1.5$ VD, $+5$ VA, $+12$ VA, -5 VA, $+28$ VA (where VD and VA stand for Voltage Digital and Voltage Analog inputs). The $+28$ V generated by the LVPS is used to power the HV boards described above. This voltage is controlled by the FPGA so that it remains off when STATIC is powered on, and requires two key commands, and an enable plug, before it can be turned on. This protects STATIC from accidental HV turn-on in air. The fully assembled STATIC sensor, and its mechanical and electrical subsystems, are shown in Figs. 8, 9 and 10, respectively.

3 STATIC ground calibration and testing

The STATIC calibration was performed in the University of California, Berkeley, Space Sciences Lab (UCB/SSL) plasma sensor calibration chamber. The facility (Fig. 11) includes a ~ 0.6 m $\times$ 2 m cylindrical vacuum chamber with Helmholtz coils for electron and low energy ion calibrations. The cryopumped chamber straddles a wall between a clean room and the calibration room allowing sensors to be assembled and inserted into the chamber while most of the chamber equipment (pumps, gauges, and power supplies) remains accessible in the outer anteroom. The facility allowed STATIC to maintain cleanliness standards required by NASA for planetary protection. The chamber has a manipulator for mounting the sensor that allows 360° motion about the sensor symmetry axis, $+/-50°$ rotations in the plane

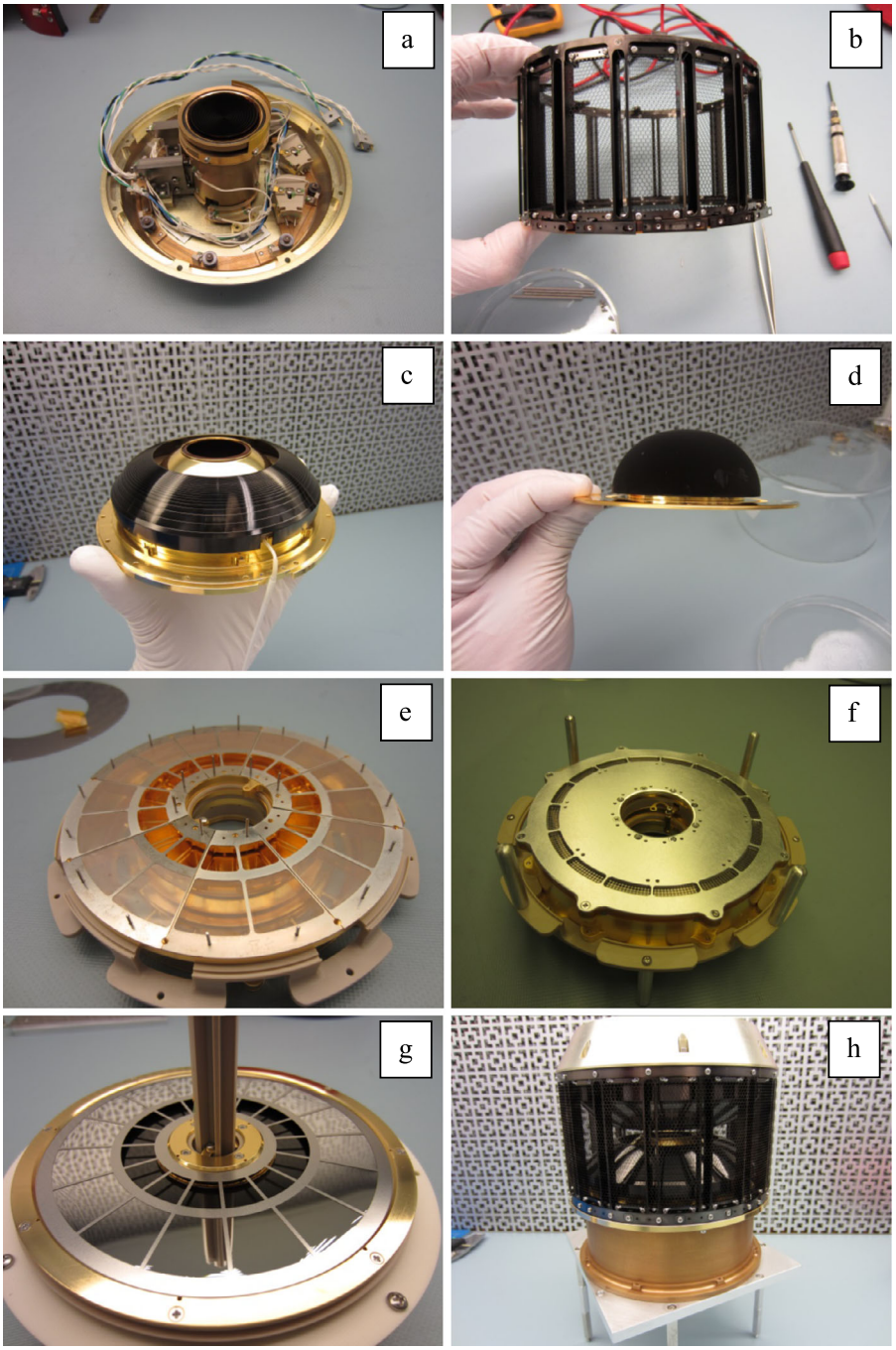

Fig. 9 STATIC mechanical subsystems: (**a**) mechanical attenuator and cover actuator, (**b**) electrostatic attenuator grids and bypass slits, (**c**) outer hemisphere with deflector, (**d**) toroidal inner hemisphere, (**e**) TOF exit, (**f**) TOF entrance, (**g**) MCPs with thick foils, and (**h**) fully assembled ESA and TOF

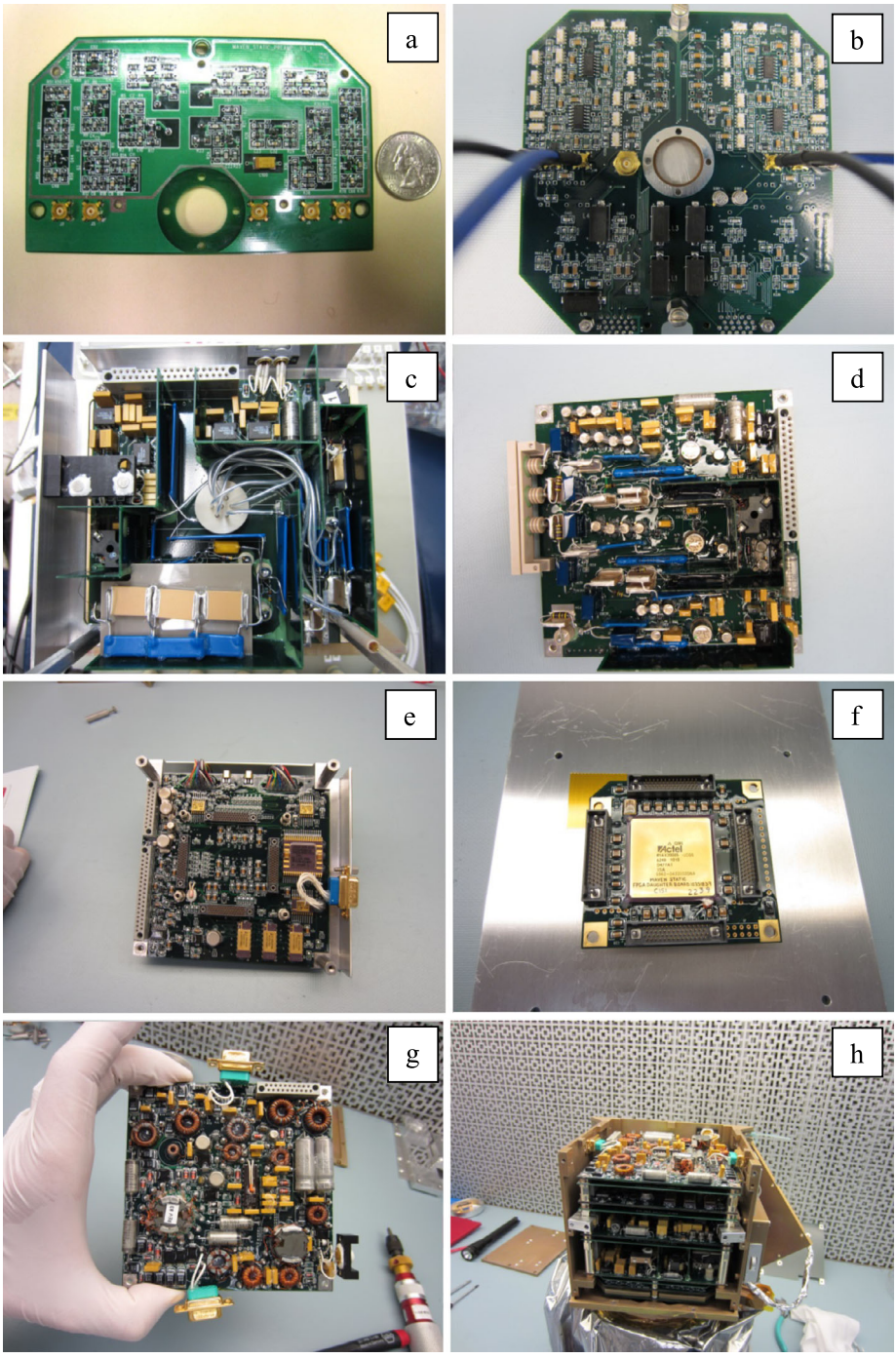

Fig. 10 STATIC electronic subsystems: (**a**) Preamplifier, (**b**) Time-to-Digital Converter, (**c**) TOF-MCP HV supply, (**d**) SWP HV Supply, (**e**) Digital Interface Board, (**f**) FPGA daughter card, (**g**) Low Voltage supply, and (**h**) fully assembled electronics

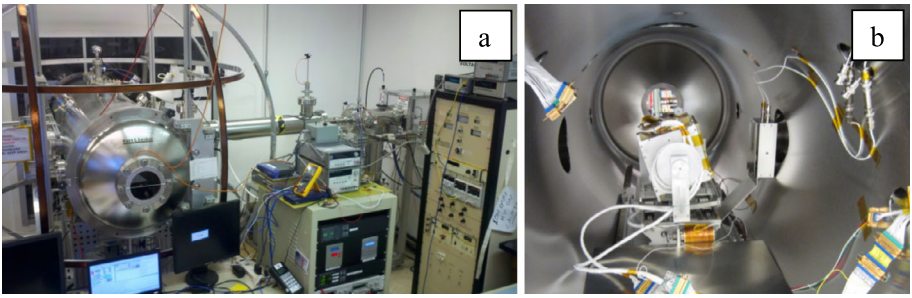

Fig. 11 (**a**) UCB/SSL plasma sensor calibration facility. STATIC was assembled in a clean room located through the window at the far end of the chamber. Helmholtz coils reduce Earth and stray magnetic fields to less than 1 %. Colutron ion gun extends to the right in the picture. (**b**) Static Flight Model mounted on the manipulator in the vacuum chamber with the box-gun located to the *right* and Colutron gun port to the *left*

normal to nadir, and linear motions along the long chamber axis to align the sensor's aperture with the beam. Most of the STATIC calibration tests were performed at pressures $< 10^{-6}$ torr. However, testing on the engineering model demonstrated that STATIC can operate at full HV, and with relatively low background, at pressures as high at 5×10^{-4} torr. These tests demonstrated that STATIC will be able to handle estimated pressures of $\sim 10^{-5}$ torr during deep-dip maneuvers into the Martian atmosphere.

STATIC was tested using two different ion guns. Most calibrations were performed using our small "box-gun" which was located in the chamber close to the sensor. This gun accelerates filament electrons through a grid and into the side of a small "acceleration-box" which can be biased at high voltage. Residual chamber gas is ionized in the acceleration-box and ejected perpendicular to the filament electron beam through the "acceleration-box exit grid" (grid is at acceleration-box voltage), followed by a grounded grid. The acceleration-box and filament are enclosed in a grounded container. Fringing fields through the acceleration-box exit grid draw ions out of the box forming the beam. The proximity of the two exit grids result in fringing fields that broaden the angular width of the beam to $\sim 3°$, adequate for most testing. In order to test STATIC down to 1 eV, the acceleration-box required a "delta-box" planar electrode, opposite the exit grids, to facilitate production of a low energy beam. The delta-box electrode was biased $+1$ V positive relative to the acceleration-box to repel ions out of the box. This was needed at low energies (low acceleration box voltage), when fringing fields were too small to draw ions out of the box. One drawback to this simple design is that scattered electrons are able to ionize some residual gas between the exit grids, forming a weak low-energy tail on the distribution which can be observed in the sensor. This low-energy tail is more prominent at smaller ion beam energies because the pre-acceleration of filament electrons (~ 150 eV) required to ionize residual gas allows these electrons to penetrate through the acceleration-box exit grids. As will be shown in Sect. 3.5, ion measurements down to 1 eV were achieved with this gun.

The "box gun" produces a multi-component beam of residual gases whose primary components are water products (H^+, O^+, OH^+, H_2O^+). However H_2^+, N_2^+, O_2^+, and CO_2^+ (and their components N^+, O^+, CO^+, C^+) are also observed, albeit at lower intensities. In order to calibrate the carbon foil secondary electron production efficiency as a function of ion mass, STATIC calibrations required a mass-selectable beam. A Colutron Model G-2-D Ion Gun System, which includes a Wien filter, provided a mass-selectable ion source. The Colutron gun uses a plasma discharge ignited by high filament current to ionize gas fed through a needle valve into the discharge chamber. The pinhole exit of the discharge chamber emits

ions that are accelerated and focused through a Wien filter. The Wien filter is followed by a 1.5 m drift tube which includes a Faraday cup for beam monitoring and a 0.1 mm pin-hole attenuator (adjacent to the Wien filter) which is used to reduce fluxes to acceptable levels. The pin-hole attenuator produced a very narrow pencil beam that made alignment difficult. The plasma discharge was at times unstable, developing both coherent (60 Hz) and incoherent flux modulations which impacted foil efficiency measurements. The gun could also be operated without the plasma discharge, in filament mode with much lower ion flux. In filament mode the beam develops a low energy tail from charge exchange between ions and escaping neutral gas in the acceleration portion of the gun. Problems with installation and operation of the Colutron gun delayed its use until the end of the third round of calibrations. Efficiency measurements were made with beams of H^+, H_2^+, He^+, N^+, N_2^+, Ar^+, and CO_2^+. The gun includes a turbopump which allowed the use of He, which does not freeze out in the cryopump. Several different gas mixtures were used during testing: "H_2-He-Ne-Ar", "H_2-Ar", "He-Ar", N_2, and CO_2. One of the more interesting features of the gun was the production of unexpected molecular ions such as H_3^+, HeH^+, HeH_2^+, and HeH_3^+ when using the "H_2-He-Ne-Ar" mix. These results, discovered during engineering model testing, will not be discussed here but are mentioned so that future instrument developments are made aware of this feature of plasma discharge guns, and can therefore take advantage of multi-component gas mixtures that include H_2.

STATIC underwent three rounds of calibration testing: (1) prior to instrument environmental testing, (2) post instrument environmental testing, and (3) post spacecraft-level environmental testing. Post-environmental testing was deemed essential in determining that STATIC suffered no damage to the carbon foils or MCP detectors. All calibrations showed the same sensor response, with no measured degradation from these tests.

3.1 Subsystem testing

In addition to standard functional tests, ground testing of the STATIC sensors and electronics included several subsystem optimizations prior to assembly and calibration. Critical components were individually tested for response including delay line chips, fast transistors, and TDC capacitors. The flight mechanical attenuator was tuned and cycled 200 times prior to integration into the sensor. It used a design tested with $> 12{,}000$ cycles on the engineering model, and 4,100 cycles on the flight spare. Carbon foils were screened for coverage using an optical scanner, subjected to vibration testing, followed by rescreening to determine any changes in foil coverage. Foils were also subjected to ion beam testing in the engineering unit to estimate foil thickness based on shifts in TOF mass peaks and stop efficiencies. MCPs were matched for bias currents and tested for low background and gain uniformity. MCP background event rates, although higher after exposure to air, generally settled down to < 100 Hz (~ 1 Hz/cm^2) after several days of high vacuum. These background events (due to radioactive decay in the MCP glass and cosmic rays) do not represent a real "event rate" since nearly all these counts are eliminated by coincidence requirements in the TOF electronics.

The anode board was tested for uniform delay-line response between anodes. Testing showed only a ~ 1 ns difference in total delay between the Start and Stop chains due to a longer signal path and larger capacitance for the Stop chain. Onboard calibration tables correct for these small differences. The four preamplifiers were tuned and checked for uniformity of response (gain and pulse shaping). TDC circuits were tested for timing-jitter, linearity and temperature dependence. In addition to bench testing, high voltage supplies were tested and characterized in high vacuum. The inner hemisphere SWP HV was also

tested and shown to be free of capacitive noise pickup from other sources, and to behave linearly at low output voltages. The digital board HV DAC analog control outputs were also tested for noise. Lastly, standard subsystem testing of FPGA control of the TDC, Test Pulser, housekeeping, and interface to the PFDPU were performed.

3.2 Analyzer energy-angle response

Figure 12 shows the energy-angle response for STATIC toroidal ESAs. The calibration data are shown for both H^+ and O^+ (includes N^+, O^+, H_2O^+, OH^+ combined) in order to identify features that reflect the non-ideal behavior of the ion gun. The figure shows the measured response for 2 keV ions without attenuation (Figs. 12a and 12b), 2 keV ions with mechanical attenuation (Figs. 12c and 12d), and 11.5 eV ions with electrostatic attenuation. The analyzer energy-angle response should be independent of gun energy unless there are surfaces that charge or if the sweep high voltage has noise that impacts low energy measurements. The gun energy was fixed at the indicated value and the sensor energy was sweeping over a limited energy range centered on the indicated ion beam energy. With this configuration, the sensor's FOV was rotated in 0.5° increments to measure the out-of-plane response. Comparing Figs. 12a and 12b shows virtually identical behavior for both H^+ and O^+ at 2 keV, with differences primarily statistical (less protons in the beam). When the mechanical attenuator is engaged (Figs. 12c and 12d), the energy and angle response narrow as expected from simulations. However, the H^+ curves show a slightly broader response indicating the proton beam is warmer than the O^+ beam. This is addressed below. Lastly, Figs. 12e and 12f show the measured response with the electrostatic attenuator engaged and an 11.5 eV beam. The broader response, particularly the high energy tail observed in the protons (Fig. 12f), is due to the ion gun, which produces a broader-energy low-energy beam, particularly for protons.

The variations in energy-angle response shown in Fig. 12, that deviate from expected ideal response such as mass-dependent and energy-dependent variations, are entirely explained by the ion source. Gun ions are produced from electron impact ionization and dissociation of residual chamber gas, primarily H_2O. This dissociation conserves momentum, therefore nearly all the dissociation energy goes into the protons (variable energy depending on ionization chemistry, and extending to > 5 eV). This results in a high energy H+ beam tail rather than the more mono-energetic water group (O^+, OH^+, H_2O^+) ions. In addition, some of the ions in the O^+ mass range are due to dissociation of N_2 and O_2, producing a broader peak in the O^+-group measurement, which is only observed at low energies where the thermal spread is appreciable compared to the beam energy. Lastly, three other features of the ion gun can result in deviations from simulated response and measured response. First, fringing fields at the exit grids result in a $\sim 3°$ wide beam rather than a purely parallel beam. Second, the gun produces a tenuous, low-energy ion tail from gas ionized between the gun's exit-grids by filament electrons scattered into this region. Penetration of filament electrons between exit grids is greater at low energies because 150 eV filament electrons (the filament is biased at -150 V) are not impacted by the small gun potentials ($+11$ V) used to accelerate the ions. Third, the ion beam, though wider than the 2 cm sensor aperture, is not uniform over aperture which can result in some skewing of the measurements. The combination of the above effects explains the small deviations of the measured response from the simulated response (Halekas et al. 2013).

Figure 13 shows the average energy and angle response of STATIC with and without the attenuators. Data in these plots use the O^+-group since the protons are intrinsically broader in energy-angle. The FWHM energy response of ~ 13 % (Fig. 13a) and angle response of $\sim 6°$ (Fig. 13b) agree with simulation values for the no-attenuation case. Calibration runs at

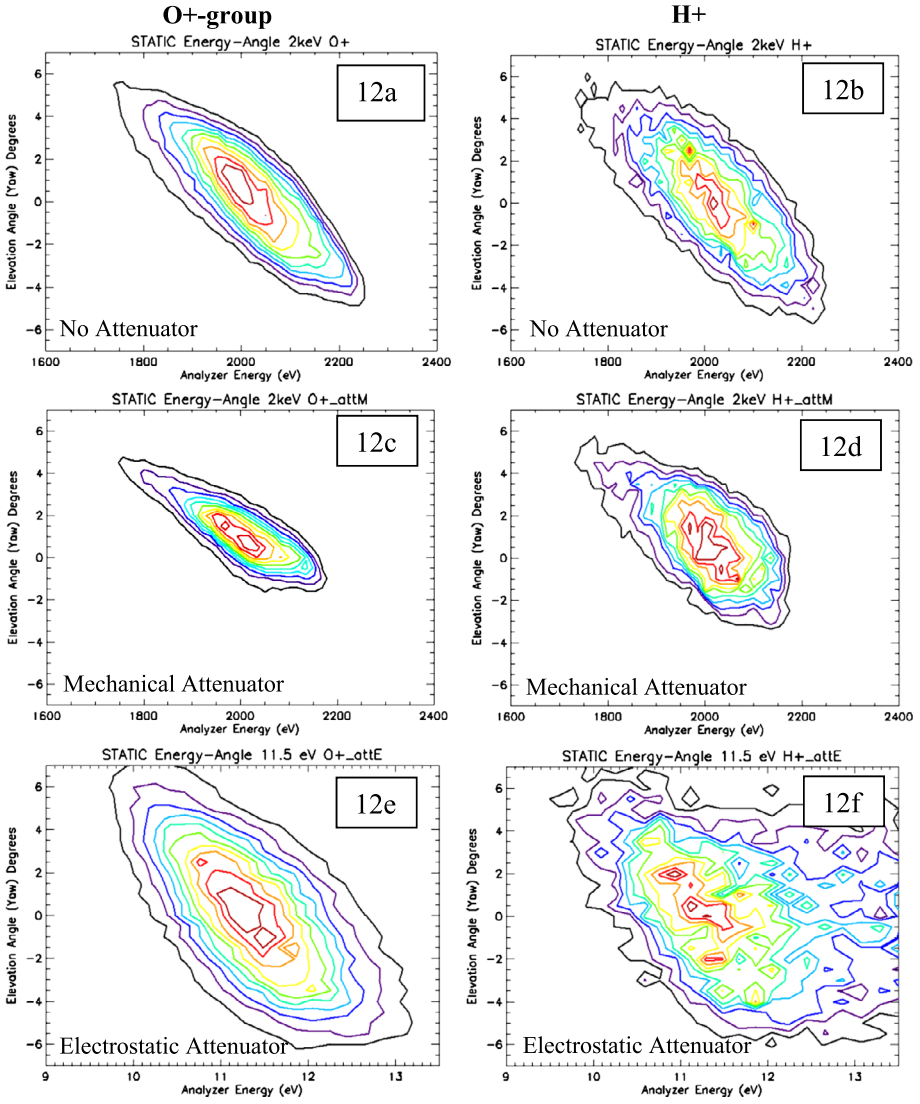

Fig. 12 Energy and angle response of STATIC's toroidal ESA to a multi-component ion beam. (**a**) O+ with no attenuation. (**b**) H+ with no attenuator, (**c**) O+ with mechanical attenuator, (**d**) H+ with mechanical attenuator, (**e**) O+ with electrostatic attenuator, (**f**) H+ with electrostatic attenuator. Mechanical attenuation narrows the energy and angle response. The low energy O+ beam (Fig. 12e) had larger dE/E due to properties of the gun. The low energy proton beam (Fig. 12f) had a high energy tail due to dissociation energy as residual water in the chamber was ionized in the ion gun. Contours are linearly spaced normalized counts

11.5 eV with no attenuation (not shown) had the same $\sim 6°$ angle response as observed at 2 keV, but had a slightly broader energy response (~ 15 %) indicating a warmer beam. With mechanical attenuation (Figs. 13c, 13d), the energy and angle responses narrow to ~ 9 % and $\sim 4°$, respectively, with a slight broadening from the expected 3° angle response due to the beam width discussed above. Figures 13e and 13f show the electrostatic attenuator produces an average response that is slightly broader in energy (~ 16 %) and angle ($\sim 8°$), than

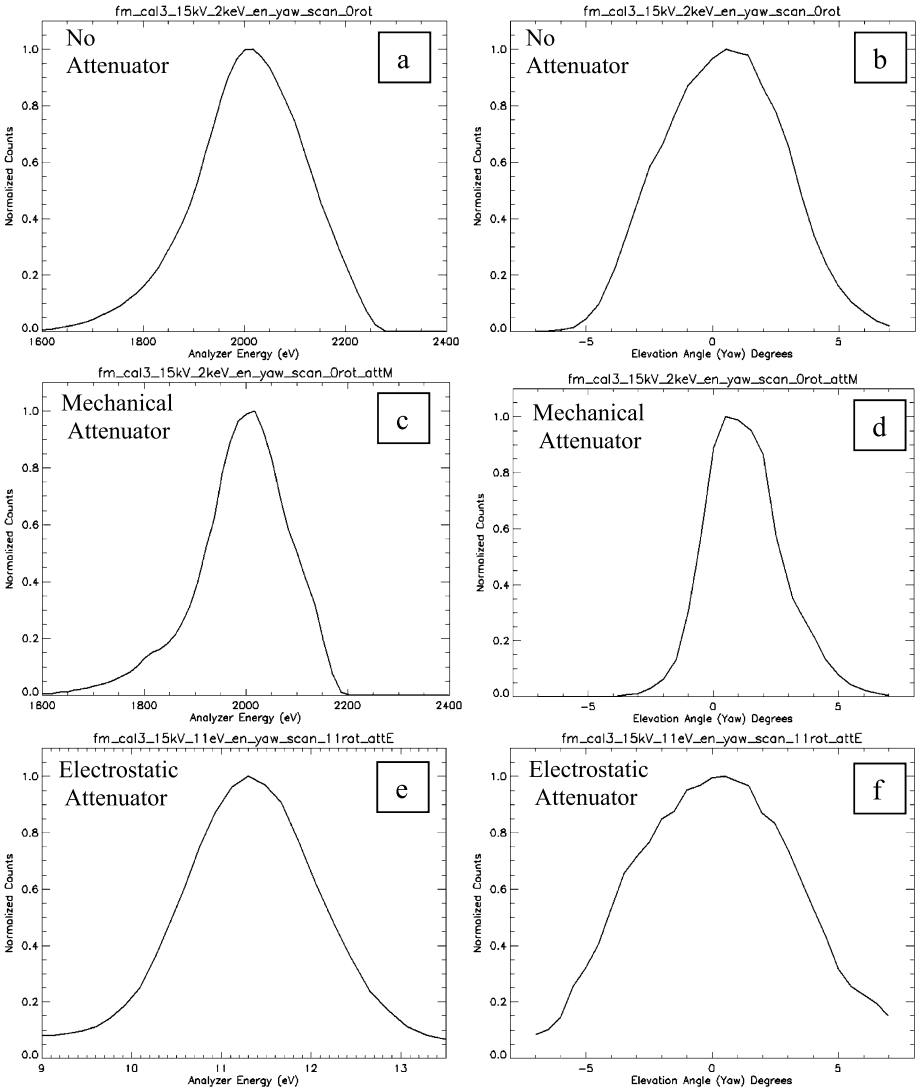

Fig. 13 STATIC toroidal ESA response to an ion beam (**a**) energy response, no attenuation, (**b**) angle response, no attenuation, (**c**) energy response with mechanical attenuator, (**d**) angle response with mechanical attenuator, (**e**) energy response with electrostatic attenuator, (**f**) angle response with electrostatic attenuator. All plots are for O^+ or water group ions. Mechanical attenuator reduces both energy and angle response. Electrostatic attenuator response is slightly broader then the nominal response

the non-attenuation case. These instrument responses are more than adequate to resolve cold thermal ions during MAVEN's periapsis encounters and, as will be shown below, are generally adequate to resolve most features of the solar wind which has a smaller temperature to drift beam energy ratio.

We note that both the energy and angle response of 11.5 eV O^+-group, with electrostatic attenuator engaged, did not go to zero at the edges of the beam (Figs. 13e, 13f). This is due to intrinsic properties of the gun, not the sensor. As mentioned above, the gun produces a low-

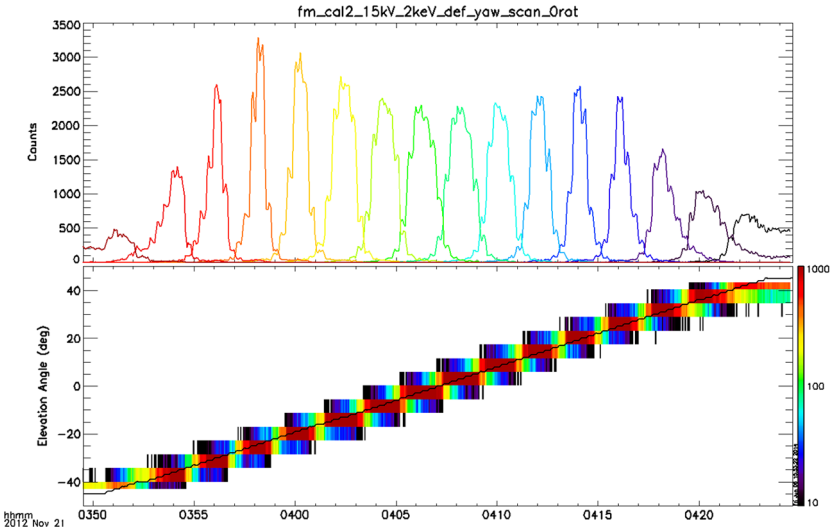

Fig. 14 STATIC deflector calibration illustrates response of the sensor to a beam rotated through its FOV. The sensor is sweeping deflectors over its full angle range, with 16 deflection steps separated by $\sim 6°$. The *upper plot* (**a**) shows counts in individual deflection angle sectors, while the *lower plot* (**b**) shows the same data plotted in spectrogram form. The manipulator was stepped in angle, rotating the sensor relative to the beam as indicated by the overlaid *black curve*. The test was performed with the beam centered on the ram direction

energy ion tail due to accelerated filament electrons penetrating between the gun's exit grids. The high energy tail, and broad angle response, results from scattered $\sim$ 150 eV filament electrons ionizing residual gas between the sensor attenuator grid (biased at +25 V) and the nearby grounded grid. These latter ions are directly accelerated into the sensor producing a background in the calibration. This background is eliminated when either the grid voltage is turned off or when the filament is turned off. Sputtered ions from the attenuator grid are also present. These backgrounds were not expected be observed at Mars because residual gas pressures are small and because thermal electrons should not have adequate energy to sputter ions from the electrostatic grid. However, during the first sunlit deep dip orbits, ion sputtering from the grids, and/or impact ionization of neutrals by electrons (thermal or photo-electrons) accelerated by the grids, did introduce spurious background. This occurred because the grid was operated at a voltage where it could produce ions in the ESA bandpass. Sweep table changes will correct this on future deep dips.

The STATIC sensor's deflector-verification and calibration are illustrated in Fig. 14. The beam was rotated through the out-of-plane FOV of the sensor while the deflectors were sweeping back and forth over their nominal deflection range ($+/-45°$). The lower plot shows the linear relationship between deflection angle (black line) and measured deflection response, validating that the response conforms to that predicted by simulations. The upper plot illustrates that the out-of-plane response, with nominal $\sim 6°$ deflection steps, contains holes in the response where sensitivity is diminished. For very narrow beams rotating through the FOV, modulation can be expected. For beams whose angular width is 6° or larger, this modulation should be negligible. For measurements of cold ionospheric plasma near periapsis, even ram ions as cold as 0.01 eV will have beam widths $> 6°$. In addition, at periapsis the sensor deflection range will be confined to $+/-22°$, giving 3° resolution. This is more than adequate to resolve ram ions even when the mechanical attenuator, which

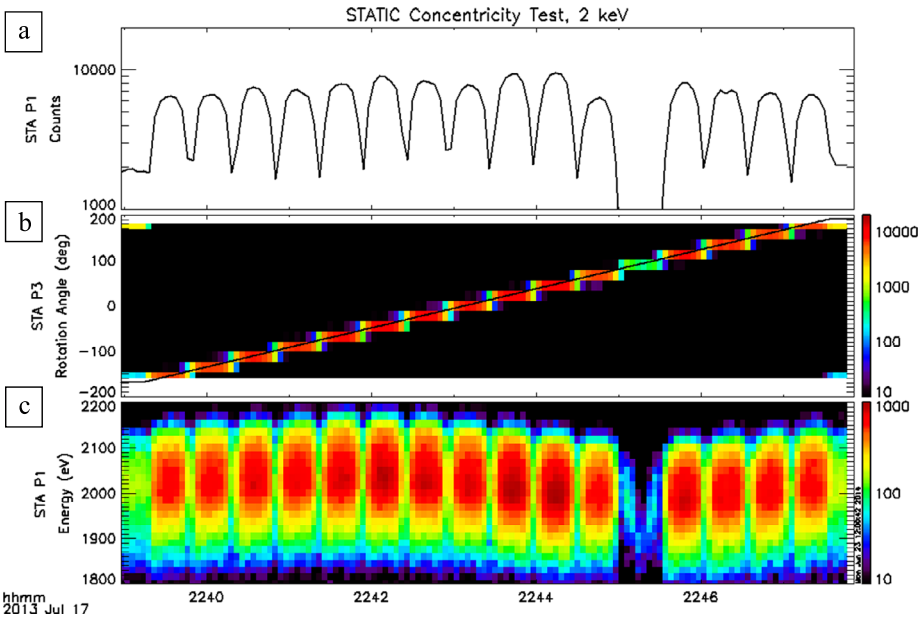

Fig. 15 STATIC sensor, sweeping in energy from 1.5 to 2.5 keV, was rotated about its symmetry axis while a 2 keV ion beam was centered in its FOV. The lowest panel demonstrates ∼ 1.5 % variation in analyzer energy response with look direction, corresponding to ∼ 18 μm alignment error. The drop in sensitivity every 22.5° is due to ESA exit posts and TOF mechanical structure at anode boundaries. One ESA entrance aperture is blocked by harnessing

narrows the angular acceptance (Fig. 13d) is engaged. One exception where such modulation might be observed would be in the undisturbed, cold solar wind. The solar wind is often narrower than 6° and significant decreases in measured solar wind density were observed occasionally during the MAVEN cruise phase when a cold solar wind beam fell into the gaps in response at large deflection angles. However, MAVEN has a separate solar wind instrument (SWIA) to provide this measurement (Halekas et al. 2013). Lastly, pickup ions are expected to have a relatively broad angular width due to an extended ion source, and therefore we do not expect modulation as these beams move through STATIC's FOV.

3.3 Concentricity tests

Analyzer concentricity calibrations are used to confirm that the analyzer was properly constructed and the hemispheres properly aligned. For STATIC a 1 % variation in energy response corresponds to ∼ 12 μm alignment error of the hemispheres. Figure 15 illustrates STATIC's response to a fixed energy beam (2 keV) as the sensor is rotated about its symmetry axis while sweeping in energy. Deflector voltages are off for this test. Panel (a) shows the valid events during each 4 second sweep. Peaks correspond to the beam being centered on the anodes. Panel (b) shows the change in anode response (Anodes 0–15 illuminated left-to-right) using sensor coordinates with 0° in the nominal ram direction for periapsis passes. The overlaid black curve in panel (b) is the rotation angle of the ion beam. Anode 11 is blocked by the harness to the mechanical attenuator. The energy spectra in panel (c) demonstrate that the variation in energy response with look direction is < 1.5 %. Therefore STATIC has a < 18 μm alignment error, better than expected from machining tolerances.

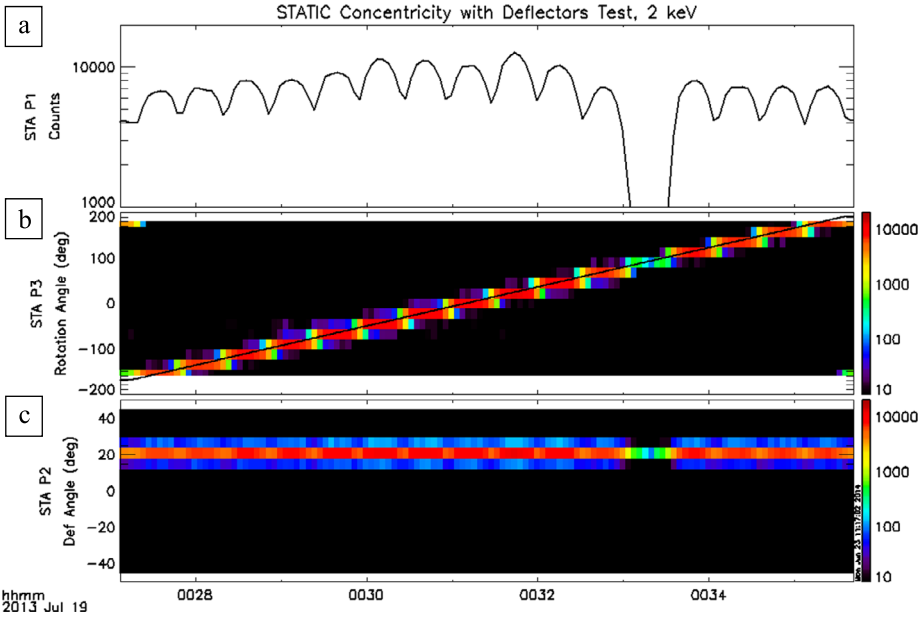

Fig. 16 STATIC sensor with beam energy fixed at 2 keV and the analyzer energy centered on the beam. The beam is directed at a 21° angle out of the analyzer's planar FOV. Deflectors are sweeping $+/-45°$ as the sensor was rotated about its symmetry axis. This test demonstrated that the deflectors were concentric with the analyzer

The drop in event rate at anode boundaries is due to a combination of beam blockage by ESA and TOF entrance and exit posts, and event rejection due to Start-Stop anode mismatch (resulting from TOF electron scattering). The residual factor of ~ 1.5 variation in peak sensitivity centered on each anode reflects efficiency variations in the carbon foils. The test depicted in Fig. 15 was performed both before and after environmental testing, giving identical results. The 1.5 % variation in energy response with rotation angle is much smaller than the analyzer's intrinsic energy resolution (~ 13 %), therefore concentricity variations can be ignored and the analyzer energy response assumed to be a constant.

Deflector concentricity tests were used to verify the alignment between the deflectors and the energy analyzer. Figure 16 shows measurements for a 2 keV beam directed 21° out of the plane of the analyzer's 360° FOV. The sensor is fixed at the beam energy and the deflectors are sweeping. The sensor is then rotated about its symmetry axis to demonstrate that variations in measured deflection direction (panel (c)) are not observed. Panel (a) shows the total counts in 4 second accumulations. Note that the drop in counts at anode boundaries is smaller for the deflected case than for the undeflected case in Fig. 15. This is the result of a small azimuthal defocusing of the beam by the deflectors, increasing the number of trajectories that miss the ESA and TOF entrance and exit posts when the beam is centered on these posts. Panel (b) shows the change in anode response as the sensor is rotated, using sensor coordinates with 0° in the nominal ram direction for periapsis passes at Mars. The overlaid black curve in panel (b) is the rotation angle of the ion beam. Panel (c) shows no significant change in the measured deflection angle of the beam (i.e. no significant counts in adjacent deflection bins) when the sensor is rotated indicating good concentricity.

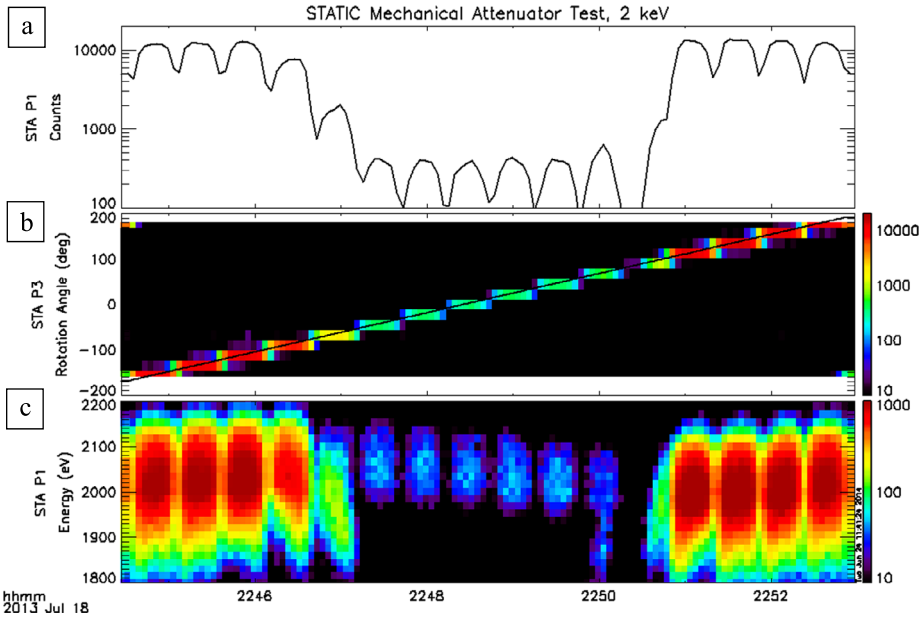

Fig. 17 STATIC sensor with the mechanical attenuator engaged, sweeping in energy from 1.5 to 2.5 keV, was rotated about its symmetry axis while a 2 keV ion beam was centered in its FOV. See text for further details

3.4 Attenuator calibrations

As mentioned earlier, STATIC was designed with two attenuators to increase its flux dynamic range by 3 orders of magnitude. The mechanical attenuator is a multi-pinhole attenuator that can be moved into and out of the main aperture (Fig. 4). The pinholes reduce the flux by a factor of 100 centered on the ram direction. The attenuator only wraps around half of the aperture, leaving the anti-ram direction at full sensitivity. Partial coverage was chosen for the design so that if the mechanical mechanism failed in the closed position, STATIC would retain half its full sensitivity for detecting pick-up ions. The mechanical attenuator should only be needed at periapsis where the ions are well collimated in the ram-direction. In contrast, the electrostatic attenuator provides a uniform attenuation factor of 10 over the entire 360° of FOV.

Figure 17 shows test results for the mechanical attenuator. The gun energy was fixed at 2 keV while the analyzer swept over a small energy range (deflectors off) centered on the beam. The sensor was then rotated about its symmetry axis. The drop in peak count rate centered on 0° (anode 7) in panel (a) is a factor of ~ 33 rather than the design factor of 100. This is due to the test setup, not an error in the design, and results from a narrow energy-angle source which does not fill the analyzer FOV. In-flight cross-calibrations of the solar wind density with SWIA confirm the design factor of 100 reduction in flux. We note that the 100 attenuation factor only corresponds to the five anodes centered on 0°. The adjacent anodes, even though their angular width is within the 180° attenuator, still see un-attenuated ions due to the finite entrance aperture width. The asymmetry of the adjacent anodes is also due to the aperture blocked by harnessing centered on anode 11(90°). This look direction will generally be blocked by the spacecraft. We also note that there is no significant shift in the

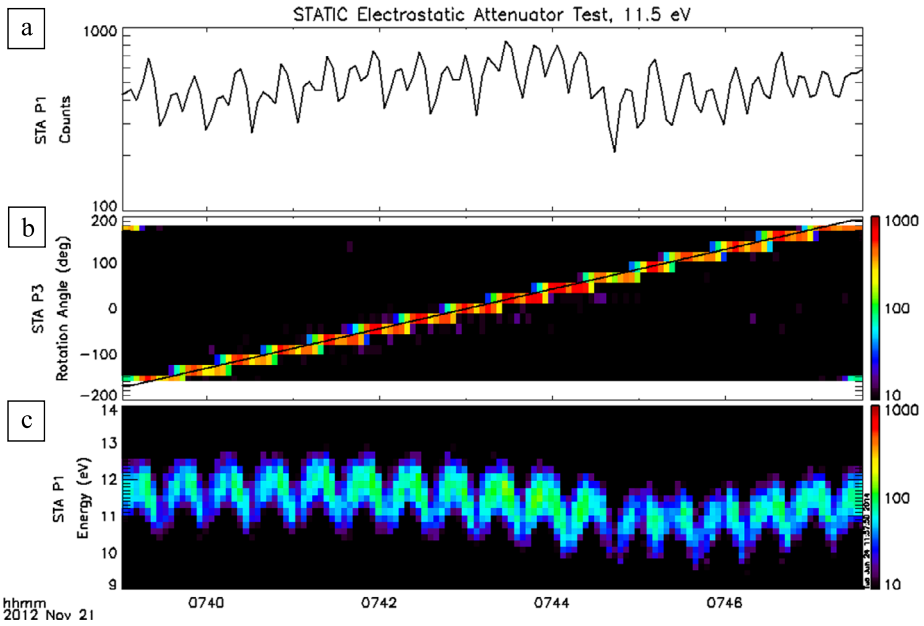

Fig. 18 STATIC sensor with the electrostatic attenuator engaged, sweeping in energy from 7 to 20 eV, was rotated about its symmetry axis while a 11.5 eV ion beam was centered in its FOV. See text for further details

measured peak energy of the beam between attenuated and non-attenuated ions demonstrating that the attenuator does not introduce a change in the energy constant. A few hundred micron error in attenuator location would have been noticeable in this plot and produced a measureable skew in energy across the attenuator boundary.

Figure 18 shows early test results for the electrostatic attenuator. The gun was set at 11.5 eV while the analyzer was swept over a limited energy range (deflectors off) centered on the beam. The sensor was then rotated about its symmetry axis. The order of magnitude drop in flux centered on anode 11 in Figs. 15 and 16 is not observed because the harness does not block the by-pass slits in the aperture posts (Fig. 5). The factor of 2 modulations in count rate across the apertures (panel (a)) result from two sources: (1) blockage by the ESA and TOF mechanical structure at anode boundaries (see Figs. 15–17) and (2) from a relatively narrow energy-angle source which does not fill the analyzer FOV. Such modulations were expected from simulations, The ~ 7 % variation in measured beam energy as the sensor is rotated, with a minimum centered near anodes 11–12($\sim 100°$), is larger than the ~ 1.5 % variation in concentricity measured at 2 keV. The same variation was observed with an 11.5 eV beam with no electrostatic attenuation indicating the measured energy shift was not due to the attenuator. A review of the sensor mounting revealed exposed insulators near the aperture where the energy dipped low suggesting charging of exposed harness was the culprit. Insulator charging by 150 eV filament electrons would deflect the low energy ion beam, changing the angle that ions entered the sensor. The small shift to lower measured energy is consistent with the energy-angle skew illustrated in Fig. 12. Instrument configuration on the spacecraft has no insulators near the aperture.

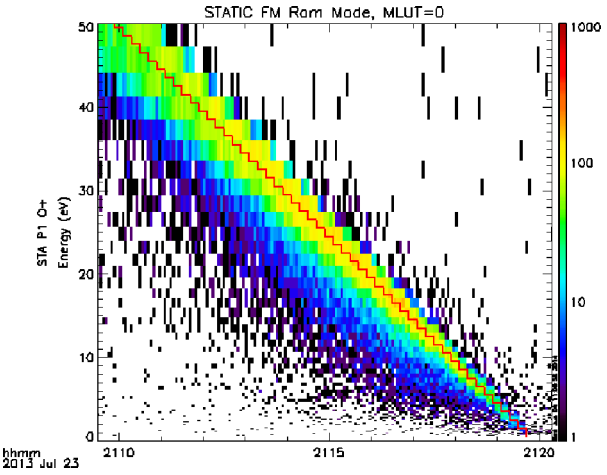

Fig. 19 Testing of the STATIC sensor (sweeping in energy from 0.7 to 50 eV) with a low-energy ion beam (*red curve*) demonstrates that STATIC can measure down to ram ion energies in the Martian ionosphere

3.5 Dynamic energy range

Most of STATIC's testing was carried out with beam energies between 100 eV and 10 keV. For these beam energies, beam deflections in the Earth's magnetic field and insulator charging of vacuum chamber harnesses can be neglected. However, to verify that STATIC's dynamic energy range could also resolve ions at < 1 eV, a test gun was developed that could produce a low energy beam (see Sect. 3). Figure 19 illustrates this low energy testing using a flight-like energy sweep table that extended from 0.7 eV to 50 eV. The sensor was sweeping logarithmically in energy while the gun was stepped through this energy range with 1 eV steps (red curve). Figure 19 demonstrates that STATIC tracks the gun energy down to at least 1.5 eV. As mentioned in Sect. 3, the low energy tail in the measured beam is a property of the gun (residual gas ionized between the gun exit grids). Measurements below 1 eV were not attempted due to inadequate ion fluxes. Since the primary measurements of low-energy ram ions at periapsis are O_2^+ at ~ 2.7 eV (for no spacecraft charging), STATIC was shown capable of these low energy measurements.

At Mars orbit insertion, flight energy sweep tables were extend down to 0.1 eV in order to look for thermal H^+ and H_2^+. Negative charging in the dense ionosphere was expected to produce spacecraft potentials of about $-6T_e/e$ (-0.2 V) which would help with these low energy measurements. The primary limiting factor was expected to be residual noise on the sweep HV voltage. The design went to great efforts to keep noise and offsets on the control voltage input to the HV supply below 10^{-5} V so that the temperature of O_2^+ could be resolved. Low noise and offset levels were demonstrated by board level testing, but could not be confirmed at by sensor level testing. Ground calibrations were not adequate to confirm this capability with a relatively warm beam (~ 0.5 eV), therefore "in situ" measurements in the Martian ionosphere were needed to determine whether this goal was achieved in the full flight configuration. Early measurements at Mars have shown STATIC capable of resolving O_2^+ temperatures as low as 0.01 eV, and measuring protons down to 0.2 eV indicating ESA performance met the specification. Lastly, voltage offsets in the OpAmps that are internal to sweep the HV supply may drift over time. These are zero-drift OpAmps that are supposed to automatically null offsets (though not bias current-induced offsets). As described in Sect. 2, STATIC includes hardware to trim away any drift in these offsets. These offsets were measured and zeroed out during cruise phase and have remained stable over the first seven months at Mars.

3.6 TOF efficiency response

The efficiencies of STATIC's carbon foils were measured using a Colutron Model G-2-D Ion Gun System (see Sect. 2) which provided a mass-selectable ion source. To prevent saturation of the sensor, the beam was collimated with 0.1 mm pin-hole aperture following the Wien filter. When combined with the small exit hole of the discharge chamber, the resulting beam was a very narrow pencil beam at the sensor estimated to be < 1 mm based on blockage by exit posts. When combined with sensor optics, the pencil beam focused to very small width estimated to be < 0.1 mm allowing small holes or tears in the Start carbon foil to be observed. The small area illumination of the Start foil resulted in secondary electrons being focused on a very small portion of the MCPs, causing detector saturation and loss of events when the flux was too high. Lastly, an asymmetrical azimuthal response was observed due to the pencil beam not being centered on the aperture. Despite these problems the testing provided adequate measurements of efficiencies at several masses and energies so the various foil dependent efficiencies could be estimated.

Foil-efficiency scans were performed for beam energies of 1, 2, 5, and 10 keV, and with TOF acceleration potentials between 10 kV and 15 kV, typically with 1 kV steps. The sensor was rotated about its symmetry axis for each scan, with the ESA energy selection centered on the beam energy. Scans were performed with H^+, H_2^+, He^+, N^+, N_2^+, Ar^+, and CO_2^+. Not all combinations were performed for all masses due to problems stabilizing the beam. The purpose of these tests was to determine the ion species dependence and energy dependence of the TOF detection efficiency. Carbon foil efficiencies are determined from the following formulas:

$$\text{Start Efficiency} = (\text{Valid Event rate})/(\text{Valid Stop rate}) \tag{1}$$

$$\text{Stop Efficiency} = (\text{Valid Event rate})/(\text{Valid Start rate}) \tag{2}$$

We include in this discussion an analysis of the various problems we experienced so that future instrument builders will have a reference when testing a new design. First, as mentioned above, Start efficiencies were observed to drop, due to detector saturation, when the event rate exceeded ~ 20 kHz. This was due to MCP charge pulse droop caused by foil electrons illuminating a small portion of the MCP, coupled with insignificant time to recharge the MCP pores due to high event rates, resulting in event pulses that fell below detection threshold. Ion scattering in the carbon foil is large enough to spread out the pencil beam and eliminate any MCP droop in Stop events. (Note: inflight measurements of efficiency will not experience saturation problems until rates exceed ~ 200 kHz because naturally occurring beams are much broader in angle.) Second, typical background event rates due to cosmic rays and radioactive decay in the MCP were observed at ~ 100–200 Hz. These events should not be included in the Valid Start & Stop rates used in efficiency calculations. If included, they can result in calculated efficiency errors of 10–20 % if actual event rates drop to < 1 kHz. This primarily impacts Start efficiencies since most of the background events are in the Stop sectors (due to larger MCP area). However, Stop rates can also be impacted by this background. The net result was that event rates between 10 and 20 kHz produced the best estimates for Start and Stop foil efficiencies. Even in this narrow event rate range, modulations of the event rates were observed to correlate with efficiencies indicating both of the above processes were still operating.

Figure 20 shows a slow rotation scan across 4 anodes with a 1 keV proton beam and -15 kV TOF acceleration. Panel (a) shows the total event rate, with 4 ms sampling and a 0.25 second box-car smoothing window, resulting in several thousand events per sample.

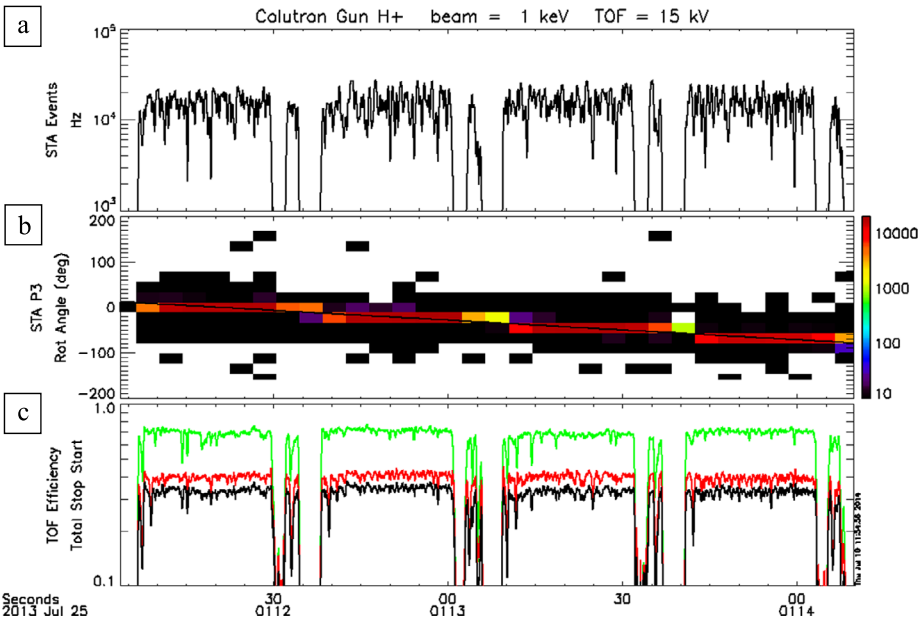

Fig. 20 Carbon foil efficiency of four 22.5° sectors with 1 keV proton beam and −15 kV TOF acceleration. Panel (**a**) event rate, (**b**) beam angle relative to Ram sector (0°), (**c**) Start (*green*), Stop (*red*) and total (*black*) efficiency

Panel (b) illustrates the rotation across 4 anodes, and panel (c) shows the Start (green), Stop (red) and total event efficiency (black), with 0.25 second averaging. There are several features of figure that should be addressed. First, the dropout of events at the anode boundaries is due to entrance and exit posts in the sensor. The dropouts are not centered on the anode boundaries because the beam was narrow and not centered on the ESA aperture. For purposes of efficiency calculations, we can ignore these features. A second feature are the narrow drops in event rate (panel (a)), sometimes with periodic spacing. These are primarily temporal modulations of the beam due to gun instabilities, although some modulation by ESA exit grids may also be present. Third, because the beam is so narrow, these measurements represent a 1-D slice across the foil and therefore cannot be just averaged to get the foil efficiency. With these caveats in mind, Fig. 20 shows that the Start foil efficiencies are ~ 0.7 and Stop efficiencies are a bit higher than ~ 0.4 for a 1 keV proton beam and -15 kV of TOF acceleration.

Figure 21 shows a similar rotation scan for the same foils and beam energy, but this time with a -11 kV TOF acceleration. Start efficiencies are roughly the same ~ 0.7, as expected, however Stop efficiencies have dropped to ~ 0.2. The reason for this drop involves the probability of Stop foil electrons penetrating and/or scattering in the thick foil (Table 2). Similar behavior can be seen in Figs. 22 and 23 for 5 keV and 10 keV proton beams and a TOF acceleration of -15 kV. Note that for Figs. 22 and 23, the event rates exceeded 20 kHz resulting in detector saturation and an underestimate of Start efficiency. This is particularly true toward the center of anode sectors due to focusing of foil electrons in the TOF optics. Examining times where the event rates are not producing saturation effects, we find that the proton Start and Stop efficiencies have only a small energy dependence, increasing by < 10 % as the beam energy increased from 1 keV to 10 keV. The variation

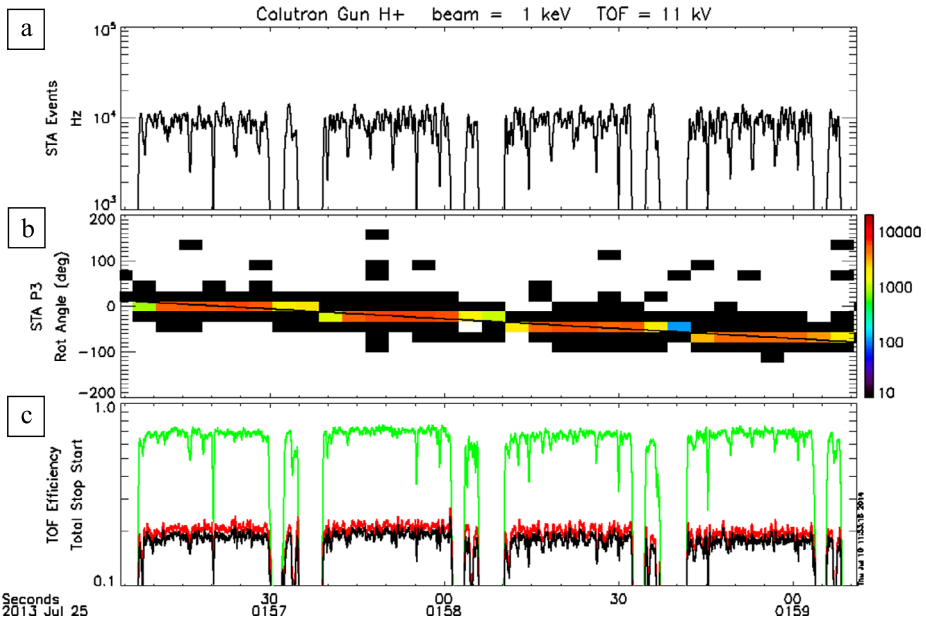

Fig. 21 Carbon foil efficiency of four 22.5° sectors with 1 keV proton beam and −11 kV TOF acceleration. Panel (**a**) event rate, (**b**) beam angle relative to Ram sector (0°), (**c**) Start (*green*), Stop (*red*) and total (*black*) efficiency

between different foils was larger, with Start foil efficiencies varying between 0.67 and 0.75 and Stop foil efficiencies varying from 0.40 and 0.47, for 1 keV proton beam and −15 kV TOF acceleration.

We can estimate typical secondary electron yields from the foils using the above efficiencies and estimates of detection efficiency from the literature. The Start foil electrons will strike the MCP at ∼ 12.3 keV (−15 kV TOF, −2.7 kV MCP). Using an estimated absolute detection efficiency of ∼ 82 % (Muller et al. 1986) and relative energy dependent efficiency of 0.56 for 12.3 keV electrons (Goruganthu and Wilson 1984), we estimate the protons are yielding ∼ 2 electrons from the foils.

$$0.7 = 1 - (1 - 0.82 \times 0.56)^n \quad \Rightarrow \quad n \sim 2 \tag{3}$$

This is consistent with the measured Stop efficiency of ∼ 44 %, where we use the 62 % Stop foil transmission of the foil support grid, 90 % foil coverage, 87 % thick foil transmission of Stop foil electrons (see Table 2 at 11 keV, thick foil voltage was −4 kV), absolute detection efficiency of ∼ 82 %, and relative energy dependent efficiency of 0.59 for 10 keV Stop electrons (which lose ∼ 2.4 keV passing through the stop foil).

$$0.43 = 0.9 \times 0.62 \times \left[1 - (1 - 0.87 \times 0.59)^n\right] \quad \Rightarrow \quad n \sim 2 \tag{4}$$

This result is in rough agreement with Ritzau and Baragiola (1998), who estimate proton yields ∼ 2.5 for the same energy range. Differences are likely due to electron scattering at the MCPs and event rejection when Start and Stop positions do not match. Variations in foil efficiencies were observed to be ∼ 15 % between different foils.

Figures 24 through 29 illustrate a variety of foil efficiency dependencies for heavier mass ions, although we note that for many of these figures the event rate is not optimal. Figure 24

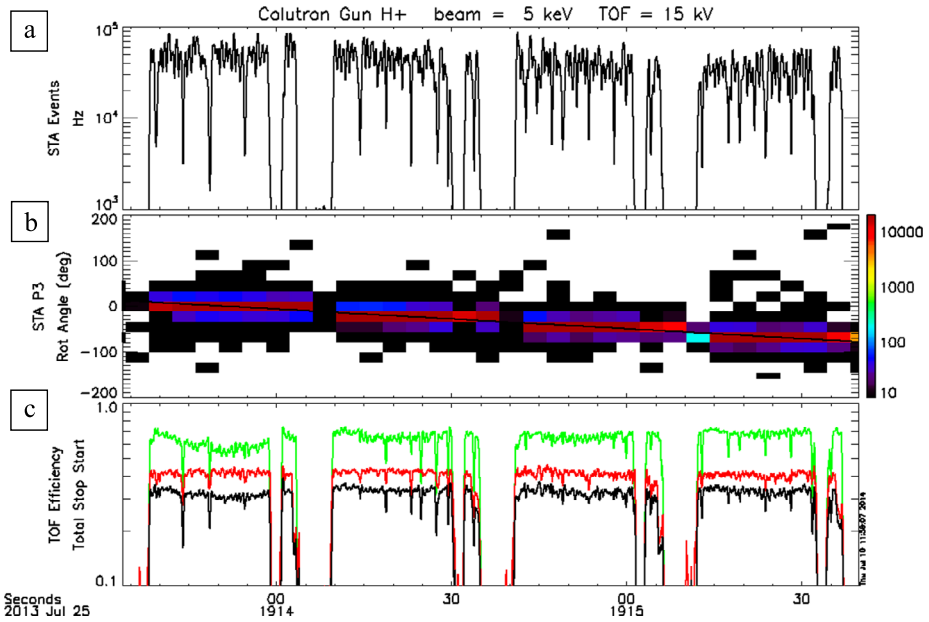

Fig. 22 Carbon foil efficiency of four 22.5° sectors with 5 keV proton beam and −15 kV TOF acceleration. Panel (**a**) event rate, (**b**) beam angle relative to Ram sector (0°), (**c**) Start (*green*), Stop (*red*) and total (*black*) efficiency

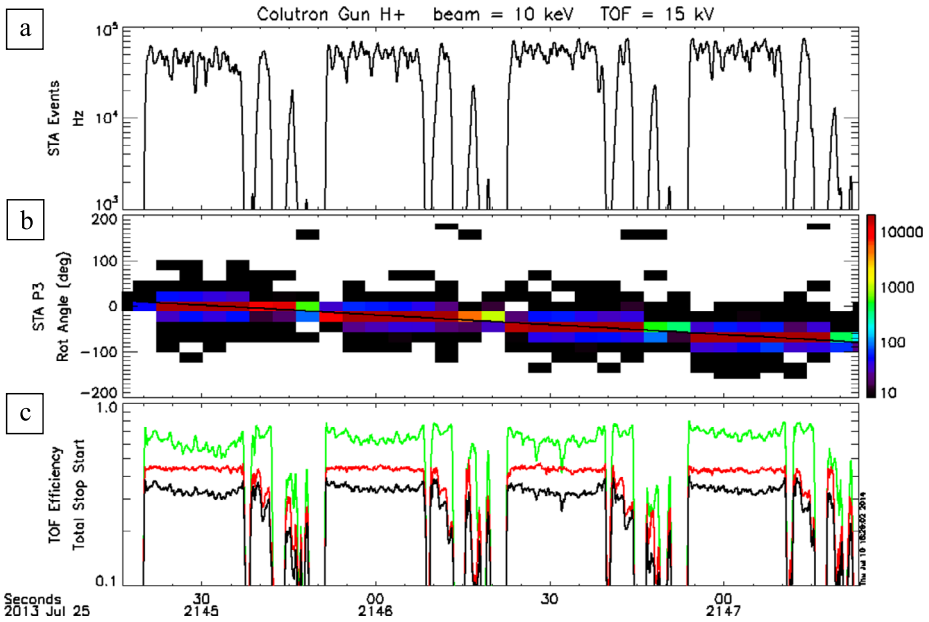

Fig. 23 Carbon foil efficiency of four sectors with 10 keV proton beam and −15 kV TOF acceleration. Panel (**a**) event rate, (**b**) beam angle relative to Ram sector (0°), (**c**) Start (*green*), Stop (*red*) and Total (*black*) efficiency

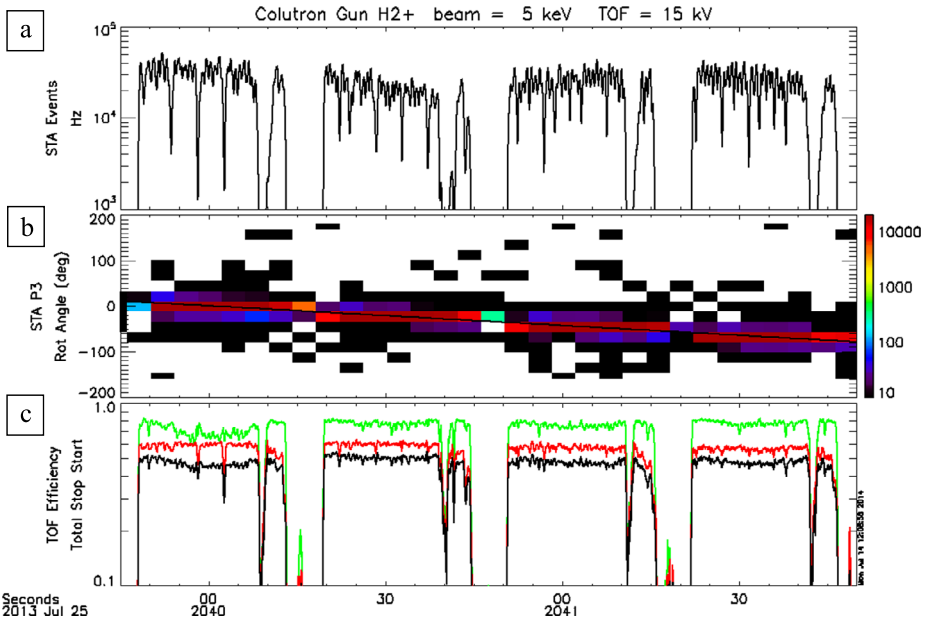

Fig. 24 Carbon foil efficiency of four sectors with 5 keV H_2+ beam and −15 kV TOF acceleration. Panel (**a**) event rate, (**b**) beam angle relative to Ram sector (0°), (**c**) Start (*green*), Stop (*red*) and Total (*black*) efficiency

shows that the Stop efficiency is 50 % higher for H_2^+, as compared to H^+, because the molecules break up in the Start carbon foil and therefore have higher probability that one of the two components penetrates the 62 % transmission Stop foil support grid and produces a stop signal. Start efficiency is also a bit higher for molecular hydrogen. Figure 25 illustrates that He^+ has about the same Start (~ 0.7) and Stop (~ 0.4) efficiency as protons. Since nuclei quickly reach a charge equilibrium state penetrating foils, we can expect similar efficiencies from alphas. Figures 26 and 27 illustrate that the efficiencies for N^+ and N_2^+ ions are similar to protons. Although most N^+ ions at these energies penetrate both carbon foils, a significant fraction of the lower energy components of the N_2^+ molecules are stopped by the second foil. At higher energies (not shown) the N_2^+ Stop efficiency approaches 0.6, similar to the H_2^+ Stop efficiency, since two molecular components have a greater combined probability of penetrating the Stop foil. Figures 28 and 29 show the efficiency of CO_2^+ at 2 keV and 5 keV. Ignoring times with MCP saturation, one can see slightly higher Start efficiencies as compared to protons. However Stop efficiencies are seen to be generally lower than for protons despite the presence of multiple ion components. At these low energies the probability of any one CO_2 component penetrating the second foil is low. Therefore a mass and energy dependence for TOF detection at Mars will be observed with heavier ions (O_2^+, CO_2^+) at low energies. As will be shown below, one of the Stop foils (anodes 10 & 11) was so thick as to reduce CO_2^+ detection efficiency to < 10 % at low energies.

For purposes of calibrations, we assume all mechanical attenuations of particles, including the 62 % transmission of the start foil mounting grid, are part of the mechanical geometric factor. The Start efficiency can also be broken into two parts: (1) the secondary electron production and detection efficiency, EFF1, which may depend on ion species and

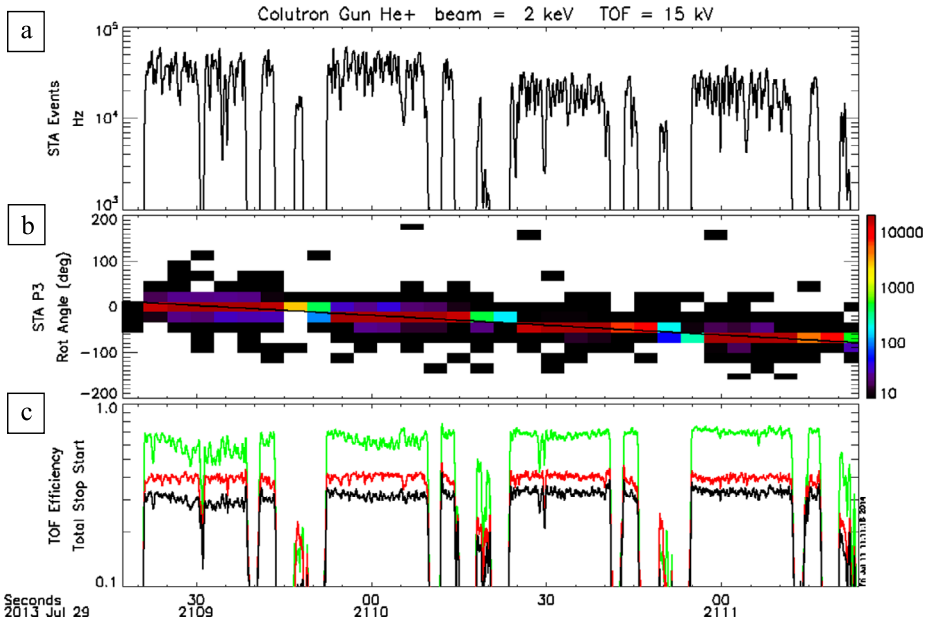

Fig. 25 Carbon foil efficiency of four sectors with 2 keV He+ beam and −15 kV TOF acceleration. Panel (**a**) event rate, (**b**) beam angle relative to Ram sector (0°), (**c**) Start (*green*), Stop (*red*) and Total (*black*) efficiency

energy, and (2) the foil coverage, COV1, (the fraction of the foil that is intact, i.e. without holes, which is independent of ion mass and energy). Breaking the Start efficiency into two parts simplifies the calibration because the former can be determined from the distribution of efficiencies measured across a foil, while the latter can be treated as a relative efficiency between foils and determined from broad, multi-ion component beam as seen in Fig. 15. EFF1 was determined from the upper cutoff in an efficiency distribution measured across a foil. Figure 30 illustrates this distribution of Start and Stop efficiencies for protons at 1 keV and −15 kV TOF acceleration. The low efficiency tail of the Start distribution (Fig. 30a) is primarily due to holes in the foil. The width of the primary peak is both statistical and the result of detector saturations. The Stop efficiency distribution (Fig. 30b) is narrower since its width primarily statistical (no detector saturation effects). The Stop efficiency, EFF2, is determined solely from these efficiency distribution measurements. It is hoped that with proper operation of MCP detectors that the energy and mass dependence of the foil efficiencies will remain constant during the mission. However, inflight calibrations will be used to check efficiencies during the mission and verify this assumption.

Figure 31 illustrates the response of the 8 flight Start and Stop carbon foil pairs (two anodes each share the same foil) for a multi-component ion beam of residual chamber gas. Each curve represents a different sector or foil pair. Five peaks are observed: H^+, H_2^+, $N^+/O^+/H_2O^+$, N_2^+/O_2^+, and CO_2^+/O_3^+. The general alignment of the peaks demonstrates relatively uniform response. The one outlier occurs in anodes 10–11, the sector partly blocked by the harness. The Stop foil for this sector was larger than the others producing much lower efficiency for detection of heavy ions at low energy.

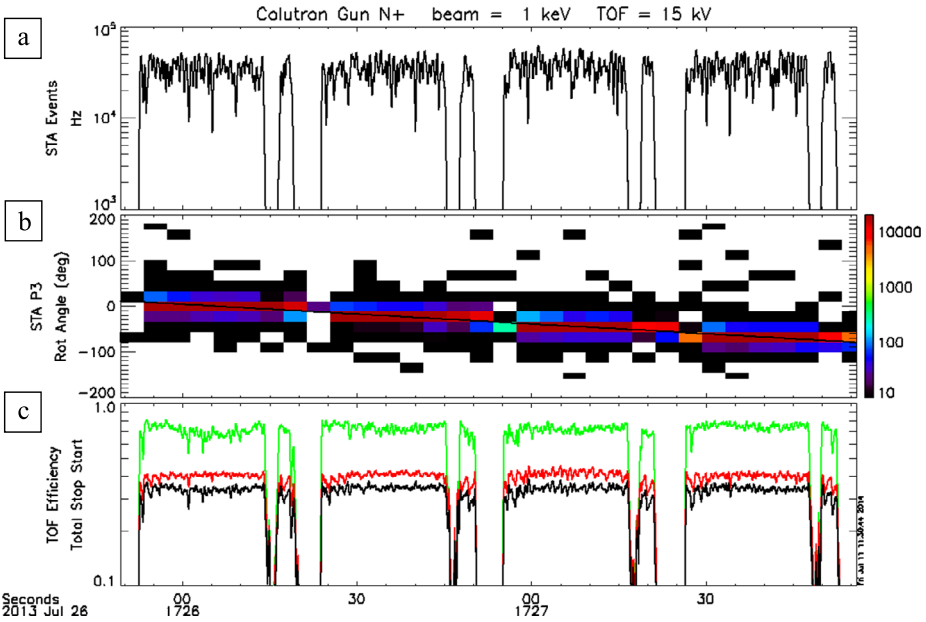

Fig. 26 Carbon foil efficiency of four sectors with 1 keV N+ beam and −15 kV TOF acceleration. Panel (**a**) event rate, (**b**) beam angle relative to Ram sector (0°), (**c**) Start (*green*), Stop (*red*) and Total (*black*) efficiency

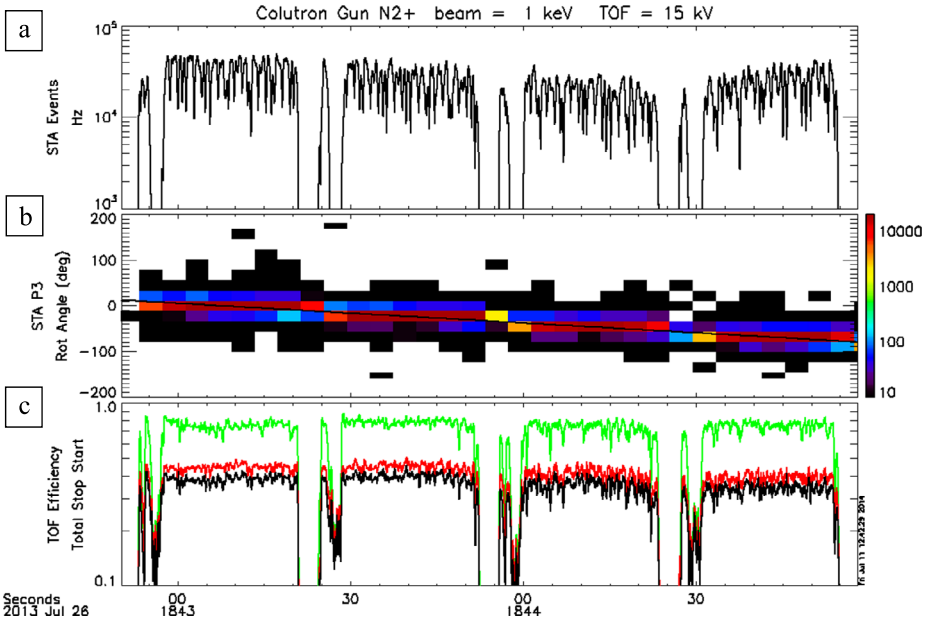

Fig. 27 Carbon foil efficiency of four sectors with 1 keV N_2+ beam and −15 kV TOF acceleration. Panel (**a**) event rate, (**b**) beam angle relative to Ram sector (0°), (**c**) Start (*green*), Stop (*red*) and Total (*black*) efficiency

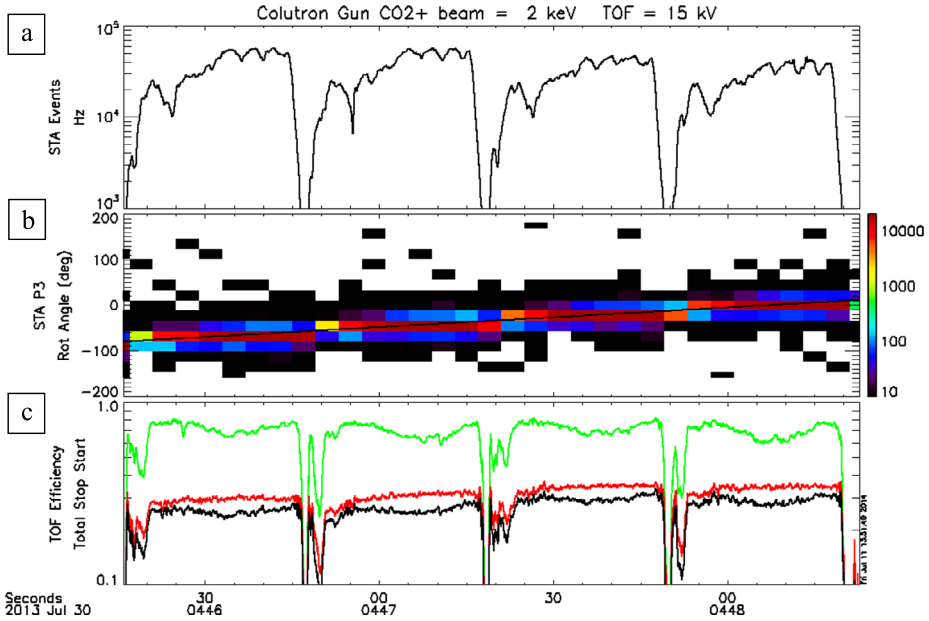

Fig. 28 Carbon foil efficiency of four sectors with 2 keV CO_2+ beam and −15 kV TOF acceleration. Panel (**a**) event rate, (**b**) beam angle relative to Ram sector (0°), (**c**) Start (*green*), Stop (*red*) and Total (*black*) efficiency

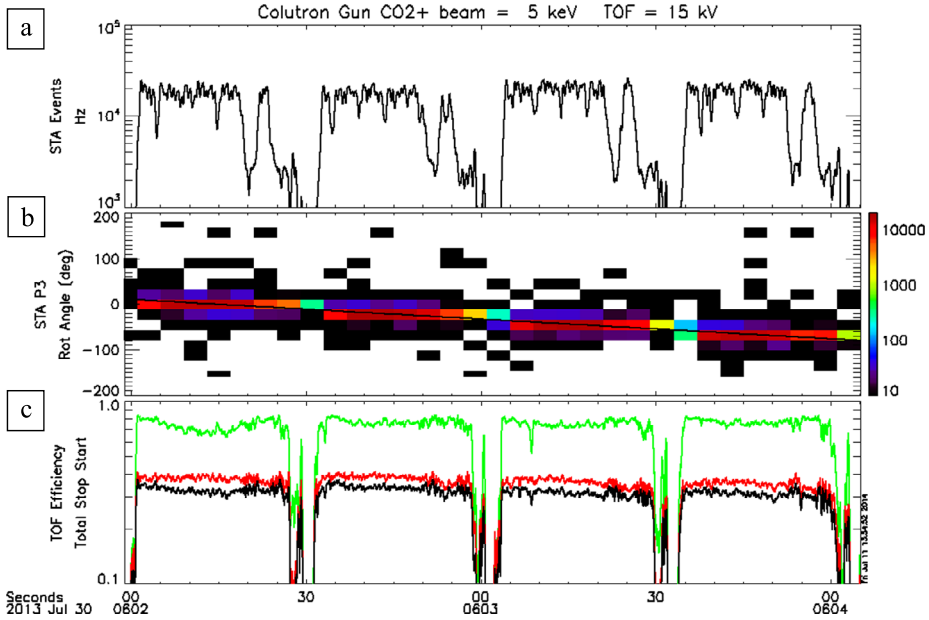

Fig. 29 Carbon foil efficiency of four sectors with 5 keV CO_2+ beam and −15 kV TOF acceleration. Panel (**a**) event rate, (**b**) beam angle relative to Ram sector (0°), (**c**) Start (*green*), Stop (*red*) and Total (*black*) efficiency

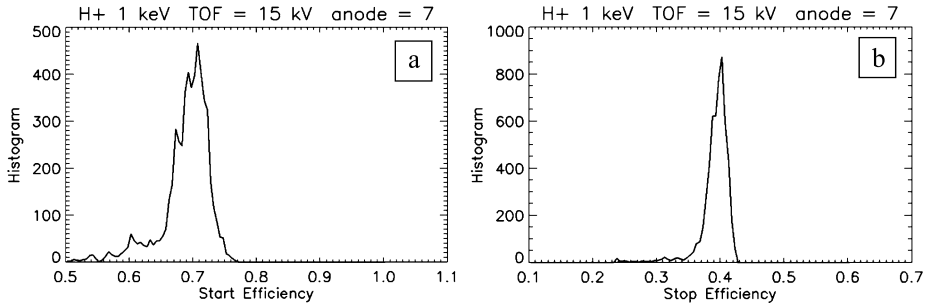

Fig. 30 Carbon foil efficiency distribution across a single 22.5° sector with 1 keV proton beam and −15 kV TOF acceleration. (**a**) Start efficiency, (**b**) Stop efficiency

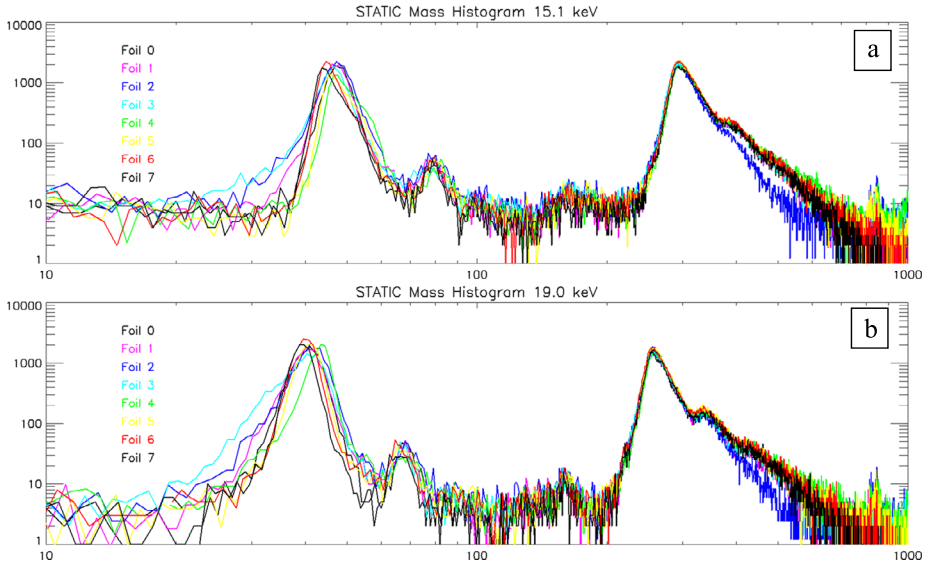

Fig. 31 Mass histogram measurements for a multi-component ion beam of residual chamber gas for 8 different Start-Stop carbon foil pairs, each with a different color. Panel (**a**) is for 100 eV ions and −15 kV TOF acceleration. Panel (**b**) is for 4 keV ions and −15 kV TOF acceleration

3.7 Sources of measurement error

Sources of error in the STATIC measurement include detector dead-time, background counts, coincident events, electronics induced errors, energy straggling, sensitivity variations with source populations and energy uncertainties at low energies. Ghost peaks (anomalous mass peaks) can also be a source of error, but will be discussed separately in Sect. 3.8 since they can also provide additional information about molecular ions. Most of these sources of error were well understood during the design phase which allowed an instrument development where measurement errors could be minimized, and where data products were designed to allow removal of background during ground analysis. The planned operation of STATIC should provide observations with relatively clean mass separations and accurate absolute calibration once these sources of measurement error are removed.

Detector and electronic dead-time determines the sensitivity and accuracy of an instrument during high event rates. For a TOF instrument, this dead-time takes two forms: (1) the "detector dead-time" which characterizes the MCP detector's loss of sensitivity at high event rates, and (2) the "electronic dead-time" required to process an event, which prevents subsequent events from being detected.

STATIC's detector dead-time stems from a droop in the amplitude of MCP charge pulses at high event rates. MCPs produce a near-Gaussian distribution of charge pulse amplitudes, known as the pulse height distribution (PHD), with the peak in the PHD much larger than the FWHM. This peak can be increased by increasing the bias voltage on the MCP detectors. To prevent loss of events, the bias voltage is selected so the peak of the PHD is several times the electronic detection threshold. However at high count rates, the current through the MCPs is not adequate to completely replenish the charge extracted from previous events, causing the PHD to droop. At high event rates, some events will fall below detection threshold. For STATIC, MCP droop is almost entirely due to loss of Start events below threshold. This is because the Start event rate is about a factor of 2 higher than Stop event rates and because Start events are more focused onto a smaller MCP detection area. For STATIC, the MCP gain is ~ 20 times the threshold, depending upon the anode, and therefore even a factor of 2 drop in gain should not be observed. For prelaunch values of MCP bias voltage, a drop in Start efficiency was observed at event rates > 100 kHz for beams $\sim 3^\circ$ wide. For the broader beams at Mars periapsis passes, STATIC handles ~ 200 kHz with no significant loss of events. In addition, STATIC attenuators are be operated so that event rates above ~ 200 kHz will normally trigger an automatic factor of 10 attenuation to prevent any detector saturation. Detector droop may also occur when STATIC measures cold, unshocked solar wind. The attenuators will not be operated at high altitudes since STATIC's goals are to resolve tenuous pickup ions, not the solar wind. Therefore a small window of energy at the peak of the solar wind may require detector dead-time corrections if meaningful measurements are to be extracted. Lastly, after arrival at Mars, data analysis software was developed to correct for detector droop which occurs shortly before attenuator activation.

For STATIC, there are separate electronic dead-times for qualified and invalid events. Qualified events must meet a detection logic criteria prior to TDC event processing. This criteria generally means that all four preamplifier signals are above threshold. However, the sensor is programmable to allow sensor operation if a single Preamp-TDC channel failed, albeit with degraded background event rejection. Dead-time for qualified events is set to 500 ns (± 20 ns digitization jitter). Invalid events, where a preamp signal is missing or where Stop occurs before Start (StopNoStart), have a dead-time of 740 ns (± 20 ns). In principle these invalid events could have a shorter dead-time than qualified events since TDC processing would not be required, but ground testing revealed an electronic problem, discussed below, which necessitated a longer pause before the electronics were reset for the next event. Dead-time correction will require monitoring both the qualified and invalid event rates separately. These two rates can be determined from the total event rate and the valid-event rate that appears in science data products. Routine science data processing will include these corrections.

Background counts in the MCP detectors can be a source of noise in plasma data. This background results from a combination of radioactive decay in the MCP glass, cosmic ray background through the MCPs, field emission in the TOF (possibly triggered by cosmic rays), and from sputtered ions created by the TOF field emission. Although the background event rate could be several kHz after an initial vacuum pump-down, these rates decayed to ~ 100 Hz after about 7 days of operation, about what is expected for detectors with an area of ~ 50 cm^2. The vast majority of these events are rejected by the coincidence rejection

leaving $\ll 1$ Hz of qualified events (both Start and Stop in the same angle sector). Most of these qualified events are further rejected as occurring in an invalid mass bin (TOF ~ 0), likely caused by cosmic ray induced field emission of an electron coupled with scattering at the detector resulting in near simultaneous Start and Stop events. During the last cycle of thermal vacuum testing, qualified background events with valid mass were observed at a rate of ~ 0.01 Hz. Of course this background will increase in the presence of significant penetrating radiation, as might be found during a Solar Energetic Proton (SEP) event.

Even though detector background counts will generally contribute negligible valid events by themselves, these events can couple with real events to create a background floor of invalid events that depends on the valid event rate. This background stems from events where detector background creates the Start or the Stop signal, rather than the incident particle. With background rates of ~ 100 Hz, and a TOF window of ~ 180 ns, the probability of a background event during an incident particle event window is $\sim 1.8 \times 10^{-5}$. For a peak count rate in the detector of ~ 100 kHz, and accounting for events where the valid Start and Stops occur before the background event (~ 40 %), we can expect uncorrected background events at about ~ 1 Hz, or at $\sim 10^{-5}$ of the valid event rate. However, since these events also require coincidence in the same anode sector, and since background is uniformly distributed in anode, the actual background event rate is only $1/16 \times 10^{-5}$. These events will be randomly distributed in TOF bin (with a slightly smaller rate above the primary mass peak) and therefore represent a negligible impact on the mass spectra.

A more important source of background events is coincident particles in the sensor rather than detector background. For a TOF window of 180 ns, and accounting for valid events (~ 40 %) where part of the TOF window is excluded, one can expect a coincident background rate (CBR) given roughly by:

$$\mathrm{CBR} = (1 - 0.4) \times (180\ \mathrm{ns}) \times (\mathrm{Rate})^2. \tag{5}$$

For a peak event rate for STATIC, ~ 100 kHz, coincident rates of ~ 1 kHz could be expected, or ~ 1 % of the events. If these high rates are uniformly distributed over the 16 anodes, than one can expect a factor of 16 reduction in this background due to coincidence rejection. However, these high rates are only expected during perigee passes where the cold ram ions will predominantly appear in a single anode or from cold solar wind which will be allowed to saturate the sensor. For the single anode case, the signal-to-noise ratio (SNR) of the primary mass peak (PMP) rate to the coincident background rate is given roughly by

$$\mathrm{SNR} \sim (\mathrm{PMP\ rate})/\mathrm{CBR} \times (\mathrm{PMP\ FWHM})/1024. \tag{6}$$

For a 100 kHz peak rate of O_2^+, whose TOF width is ~ 8 % of the TOF window, one could expect a background rate floor of ~ 0.3 % of the peak. For protons or alphas at 100 kHz, the SNR should be ~ 0.01 % since these peaks are much narrower. Since this SNR scales with the rate, for a more nominal 10 kHz event rate this background should be negligible.

There are two sources of electronics-produced errors in the STATIC TOF data. The simpler of these two errors is timing jitter in the TDC board which converts analog signals to digital signals. Approximately 1 ns timing jitter is present in the data and determines the FWHM of the low mass peaks (H^+, He^{++}, He^+). For a proton time-of-flight of ~ 12 ns, this jitter does not impact the sensor's ability to separate protons and alphas. The high-mass wing of the proton peak is down by almost 3 orders of magnitude at the alpha peak, which should allow the sensor to easily resolve solar wind alphas.

The second source of electronic noise is due to a poor choice of a transistor switch in the TDC circuit. Recall that the TDC timing circuit uses a constant current source to charge a capacitor for an interval between the Start and Stop signals. The voltage on the capacitor is

then measured to determine the TOF. At the end of an event, the circuit is reset and a transistor switch discharges the capacitor. The capacitor is held in the discharge state until the next event comes along. The circuit sets a minimum 160 ns for the discharge for fully qualified event. This was expected to be adequate for the anticipated 20 ns RC time of the circuit. Unfortunately the selected transistor does not act as a good switch, with internal capacitance slowing the discharge. As measured in the lab, the capacitor experiences a complex charge-decay, with multiple time constants. After an initial rapid charge drain, the discharge slows and ~ 7 % of the charge still remains after the 160 ns reset pulse. This charge continues to drain after the reset, but any event that occurs shortly after a reset will add this residual charge to the actual event charge. The net result is that at high count rates (~ 1 MHz) for a single-mass ion flux, a shift in the mass peak could be observed. For the ~ 100 kHz count rates expected for STATIC (because of its attenuators), the mass peak does not shift but some broadening occurs on the high-mass side. This broadening does not significantly impact resolving low mass ions. For high mass ions, the mass peak broadening due to energy straggling in the carbon foils dominates over any electronic broadening.

The incomplete drain of the TOF capacitor introduces several additional minor problems. Fortunately instrument settings, and nature, allow mitigation. First, since the Stop efficiency is only ~ 40 %, while the Start efficiency is ~ 75 %, roughly 45 % of events have a Start without a Stop (StartNoStop). These events will fully charge the TOF capacitor and therefore will have a residual charge after reset that can be significant. For calibrations, the reset pulse duration was set to 200 ns (380 ns dead-time), resulting in a ~ 5.7 % residual charge which was about as large as the charge deposited for a proton. Therefore those proton events that directly followed a StartNoStop event were shifted far off the nominal mass peak. Figure 32a illustrates this broadening of TOF measurements for protons at 200 kHz (black), compared to 10 kHz (red). The broader tail for the 200 kHz TOF peak, with a sharp cutoff just above TOF bin 100, is caused by the non-linear capacitor decay. Ground testing confirmed elimination of the shoulder by increasing the invalid-event dead-time to 740 ns, resulting in only ~ 1 % of residual charge remaining after a reset. Even at the highest rates, this introduces only a very small broadening of the proton peak which will not impact resolving tenuous alphas. (Note: the secondary peak between TOF bins 200 and 300 in Fig. 32a is associated with N + /O + /H2O+ and appears to be ion sputtering off surfaces at the exit of the ESA.)

A second type of anomalous TOF event occurs when a StartNoStop event is followed closely by a "cross-talk event", where both Start and Stop are detected nearly simultaneously. Cross-talk events are due to internal scattering of a Start (or Stop) electron into the nearby Stop (Start) portions of the detector. These events represent 3 % to 7 % percent of all valid events. Simultaneous Start and Stop would normally mean that these events could be easily rejected, however the residual charge from a previous StartNoStop results in a finite value for the TOF. These events produce a background shoulder at TOF values below the proton peak. The impact of this form of background was again minimized by the increased reset pulse duration for the StartNoStop events.

A third source of anomalous TOF events occurs when a high mass ion is followed closely by a low mass ion. In this case, the residual charge from the high mass ion event can be significant compared to the charge deposited by the low mass ion. For example, if an O_2^+ ion (TOF ~ 68 ns) is followed immediately by a proton event, then residual charge can add ~ 5 ns (7 % $\times$ 68 ns) to a 12 ns proton TOF. For typical maximum count rates of ~ 100 kHz for a O_2^+ dominated plasma, only a small fraction (~ 1 %) of protons events will occur in the first 100 ns after an O_2^+ event. Therefore the proton peak will not be shifted, but it will have a high-mass shoulder at a low intensity that could extend out to the alpha peak. Fortunately nature acts in our favor to minimize this problem. The only time STATIC will

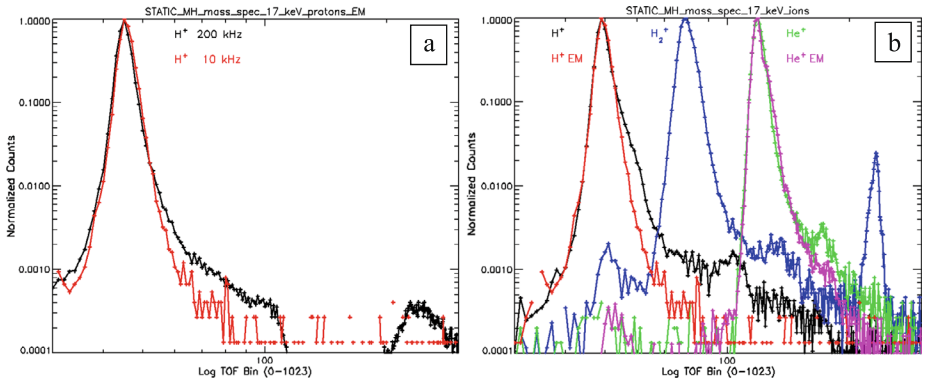

Fig. 32 (**a**) Mass histogram measurements from the engineering model (EM) sensor of protons at 200 kHz (*black*) and 10 kHz (*red*). The shoulder on the 200 kHz proton peak between TOF bins 60 and 110 results from too short a reset pulse (see text) and can be corrected by increasing the reset time for StartNoStop events. The secondary peak between bins 200 and 300 appears to be sputtering of ions at the analyzer exit. (**b**) Comparison of mass histogram measurements from the flight model (FM) and EM sensors. Although the various mass peaks are well separated, the FM spectra (*black*, *blue*, *green*) manifest high-TOF shoulders not observed in the EM sensor (*red*, *magenta*). The ghost peak at TOF bin ~ 230 results from dissociation of H_2^+ in the foils. See text for analysis

observe large fluxes of high-mass ions will be near periapsis where cold ion energies are primarily determined by the spacecraft ram velocity. In this case, low mass ions are never observed simultaneous with high mass ions, so this broadening of the proton peak should not be observed.

Flight unit testing revealed an additional source of low-level TOF overlap between different mass ions. Figure 32b shows flight model (FM) TOF spectra for H^+ (black), H_2^+ (red), and He^+ (green) at event rates ~ 20 kHz. The cross-over between low-mass ion spectra occurs at about the 0.3 % level. All three FM spectra show a high mass (high TOF) shoulder at the 0.2–0.4 % level, higher than those observed in the engineering model (EM—red and magenta). The primary difference in the two sensors was the addition of a "field suppression grid" in front of the Start foils on the FM unit. Both sensors had field suppression grids in front of the Stop foils. Suppression grids were included in the design to reduce the electric field gradients at the carbon foils, where small foil tears could be a source of field emission. It was hoped that the Start suppression grid would not be needed since it could reduce sensitivity and broaden the measurements. During the course of testing, the FM sensor initially experienced severe background noise caused by field emission from the TOF analyzer when at high voltage. Adding the Start foil suppression grids did not eliminate the field emission problem in the FM unit and the source of the noise was eventually identified as a very small carbon foil fiber on the side of the TOF. However, it was deemed prudent to leave the suppression grid in place so that any future foil tears would not field emit. This difference suggests that energy loss by ions scattering off the Start suppression grid may be causing these extended tails, although definitive identification of the source cannot be made. As will be shown below, these tenuous high-mass tails were also observed during the cruise phase to Mars. Preliminary measurements indicate that they scale with the primary beam flux, and can therefore be modeled and subtracted from the mass distribution. The ghost peak at TOF bin 230 in Fig. 32b will be discussed in Sect. 3.8.

Another source of measurement error involves sensitivity variations with sensor FOV, coupled with uncertainties in sensor geometric factor with look direction. As shown in

Fig. 14, STATIC has holes in its response over its nominal 360° × 90° FOV. These gaps can lead to errors in both the measured flux and the direction of narrow beams. Fortunately, most ion fluxes are expected to be larger than ∼ 6° so this is generally not expected to be a problem. However, STATIC's measurement resolution in its 360° FOV (phi) is only 22.5°, therefore the velocity component of beams much narrower than ∼ 10° may be poorly resolved in the phi direction. In addition, STATIC's FOV only covers about 70 % of 4π steradians. Of that 70 %, up to 30 % may be blocked by the spacecraft depending upon the orientation of the APP. Therefore scientists should use caution when calculating bulk parameters of the measured distributions, especially with automated routines. We strongly suggest that scientists test assumptions about the FOV impacts on the analysis. Finally, measured parameters will also be impacted by instrumental uncertainties in detection sensitivity with look direction. At this early phase of the mission we are fairly confident that relative measurement errors between different look directions can be maintained at < 10 %, and perhaps much better. Inflight data is being collected to allow monitoring of efficiency variations over time. Absolute calibrations are expected to be maintained at better than ∼ 20 % level, and may be much better depending upon data available from other instruments for cross-calibrations.

For low altitude measurements, where cold ions enter the sensor at the spacecraft velocity, the primary measurement uncertainty is the energy resolution of these ions. As shown in Fig. 19, and discussed in the associated text (Sect. 3.5), STATIC demonstrated its ability to measure down to at least ∼ 1.5 eV during ground calibrations, and its ability to trim its HV sweeps to account for any offset drifts that might prevent its energy sweep from approaching zero. This offset control was tested during cruise phase is expected to correct any offset drifts with an estimated offset error of ∼ 10 mV on a 4 kV supply. This corresponds to an energy error < 0.1 eV. No drift of these offsets was observed during one year of operations. At the energy where the bulk of ionospheric O_2^+ is measured (∼ 2.7 eV), this offset should not impact the measurement.

What was not known at launch was the level of noise on the HV sweeps, which could impact ion temperature measurements, and whether any additional small systematic offsets were present in the instrument (for example work function differences). Inflight calibrations at Mars have since revealed the level of noise to be negligible since O_2^+ temperatures down to 0.01 eV could be resolved. Protons were observed down to 0.2 eV total energy suggesting any additional systematic offsets are very small. These observations will be published with first results papers.

Spacecraft charging can also play a role in these low energy measurements. Near periapsis (where T_e is expected to be ∼ 300 K or ∼ 0.03 eV), charging to $-6\ T_e/e$ (−0.2 V) was expected to introduce a small offset to the ion energy measurements (∼ 0.2 eV). However, inflight measurements at Mars have shown spacecraft charging is generally −1 V to −2 V, and can be in the range of −5 V to −20 V depending upon spacecraft orientation and plasma density. This charging appears to be the result of non-conducting solar panel surfaces and poor ion current collection in specific spacecraft orientations relative to the ram direction. Software is expected to account for spacecraft charging using Langmuir probe measurements, but inclusion is awaiting LPW inflight calibration efforts.

Lastly, we point out that at these low energies, surface contact potentials of different materials in the sensor may play role. There are indications that some surfaces have changed after four months at Mars, perhaps due to interactions between atomic oxygen and surface materials, or the monolayers of surfaces gases on these surfaces. Investigations of these changes are just beginning and these changes may complicate the lowest energy measurements. Any future users of low energy STATIC ions should wait until data validation is complete.

3.8 Mass resolution and ghost peaks

Ghost peaks in TOF mass spectrometers are spurious time-of-flight signals with peaked m/q values other than those expected for ideal analyzer response to a given incident beam. Unlike sensor noise and background, ghost peaks are correlated with the incident beam. Ghost peaks result from internal scattering of ions, from variations in charge states when particles exit the carbon foils, and from molecular breakup. Examples can be found in Young et al. (2004).

A key feature of the STATIC sensor design was the introduction of a thick foil (Sect. 2) to eliminate ghost peaks from light ions that emerge from the Stop foil. For the STATIC design, ions have a finite probability ($\sim$ 20–30 %) of penetrating the Stop carbon foil without producing a Stop electron. These particles could produce a delayed Stop signal, and therefore an invalid TOF, should the particle strike the MCP detector or reflect and strike the carbon foil a second time. Most of the particles emerging from the Stop foil are neutrals ($\sim$ 90 %) and could therefore reach the MCP detectors producing a delayed Stop pulse. Smaller ghost peaks could result from ions emerging with negative charge and accelerating to the MCP detector, or from ions emerging with positive charge, reflecting, and producing a delayed strike on the carbon foil. A method of suppressing these penetrating ions was essential to eliminating measurement contamination from ghost peaks. The thick foil eliminates all neutral and negatively charged ions, but can reflect positively charged ions. The potential on the thick foil was selected so most positively charged light ions (H^+, He^+) will also strike the thick foil since their energy loss in the carbon foils is less than the voltage difference between TOF and thick foil, times q. For heavier ions, this is not the case and reflected O^+ and O_2^+ could be expected to produce small ghost peaks. However, since these ions have a significant high mass tail, ghost events do not form a measureable peak.

The one light ion expected to produce a ghost peak is H_2^+, as illustrated in Fig. 32b (blue curve, TOF bin $\sim$ 230). The hydrogen molecule will breakup when penetrating the Start carbon foil, resulting in components that exit the second carbon foil with energy given roughly by the initial energy plus TOF acceleration energy, less foil losses ($\sim$ 4 keV), divided by 2. For low initial energies, the components emerge with only $\sim$ 5–6 keV of energy. If they emerge positive, they will reflect before striking the thick foil, producing a delayed strike on the Stop foil. A small fraction of H_2^+ events ($\sim$ 3 %) produce this ghost peak, which could potentially be used to distinguish He^{++} from H_2^+. The ghost peak is centered near the O^+ mass peak (mass 11–12), therefore at the energy measured the O^+ flux could not be large or it might mask the ghost peak. For periapsis passes at Mars, where particle energy is determined primarily by (ram velocity)^2 $\times$ mass/2, this should be the case. STATIC periapsis data shows evidence of tenuous H_2^+ in the upper ionosphere, however detection of a weak ghost peak has not been attempted.

STATIC's response to heavy ions is illustrated in Figs. 33, 34 and 35. Figure 33 demonstrates that N^+ and N_2^+ (which serve as proxies for O^+ and O_2^+) are well separated by the TOF analyzer. The figure shows mass separation at (a) 15 keV and (b) 20 keV total ion energy for N^+ (black) and N_2^+ (red). In both cases, the N_2^+ spectra exhibits a low-mass (low-TOF) shoulder at the $\sim$ 1 % level which extends below the lower cutoff of the N^+ spectral peak. The fraction of events in this shoulder is $\sim$ 1.5 %. This shoulder shifts in energy with the beam energy indicating it is not internally produced by sputtering. The amplitude of this shoulder is much larger than would be expected for known ghost peak scenarios that can produce a shorter TOF signature.

For example, if one assumes 75 % foil electron production efficiency and uses 62 % transmission for foil frames, one can estimate the relative fraction of ghost events to valid events for the case where an N_2^+ produces no Start signal, but Start-Stop cross talk combined

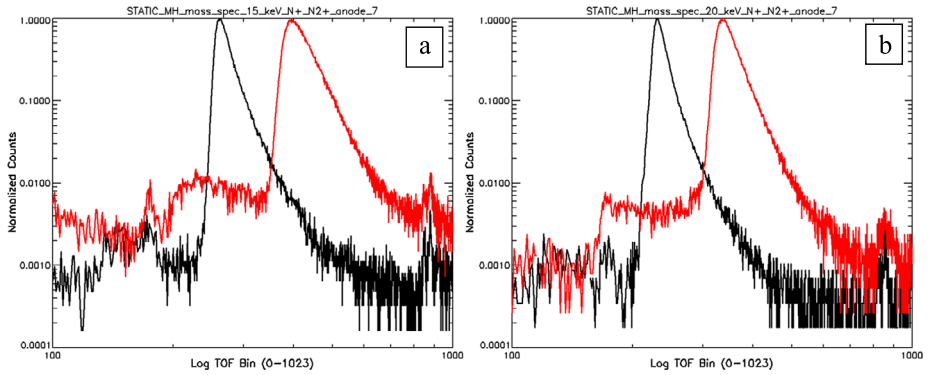

Fig. 33 (**a**) Mass spectra for 15 keV N^+ and N_2^+ ions. (**b**) Mass spectra for 20 keV N^+ and N_2^+ ions. TOF voltage is −14 kV for 15 keV ions (1 keV initial ion energy), and −15 kV for 20 keV ions (5 keV initial ion energy)

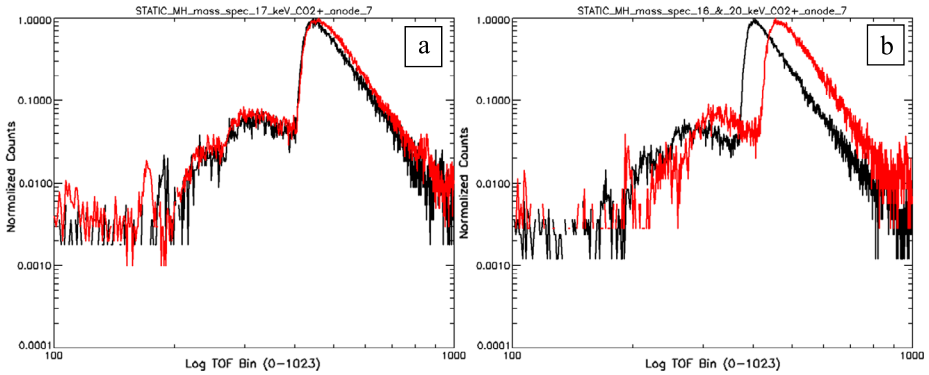

Fig. 34 (**a**) Mass spectra for 17 keV CO_2^+ ions. The *black curve* consists of 5 keV ions and −12 kV TOF acceleration, whereas the *red curve* has 2 keV ions and −15 kV TOF. The slightly broader *red peak* is due to high event rates (see text). (**b**) Mass spectra for 20 and 16 keV CO_2^+ ions for a 5 keV beam and −15 kV (*black*) and −11 kV (*red*) TOF accelerations

with ion reflection results in a shortened TOF. The fraction of events where the N_2^+ has no signal from the Start carbon foil is ~ 0.25. The fraction of events where one atom of the N_2 molecule produces a Stop foil electron, which subsequently scatters to the Start sector is given by $(0.62 \times 0.75 \times 0.07)$, where 0.07 was an observed cross-talk rate. This factor should be multiplied by the probability that the other N_2 component does not produce a Stop, $(1–0.75 \times 0.62)$, times 2 to account for swapping ions. Lastly, we include the probability for the ion emerging with a positive charge (~ 0.1, Burgi et al. 1990), reflecting and producing a delayed Stop event (0.75). The total probability is then $\sim 7 \times 10^{-4}$. This should be compared to valid event probability, ~ 0.4, to get a ratio of ghost events to valid events of ~ 0.16 %. This estimated ghost event rate is about an order of magnitude smaller than the observed rates in Fig. 33.

We suspected that the extended shoulder might be an artifact of the ion gun. However, once STATIC reached Mars, similar shoulders were observed for O_2^+. We now believe that the shoulder may be due to dissociation and charge exchange at the ESA exit grid, producing

lower mass and higher charge state ions. For data analysis purposes these shoulders will be treated as ghost peaks and algorithms will be developed for removal of this background.

We point out that there are small secondary peaks in Fig. 33, at TOF $\sim$ 180 and $\sim$ 860, which do not shift with beam energy. The former peak ($\sim$ 180) does shift with TOF voltage (see discussion below) suggesting a weak ghost peak due to sputtering at the ESA exit. The latter peak at TOF $\sim$ 860 is not understood but believed to be electronic and associated with internal event timing since it was observed in the tail of all heavy mass ions. This latter peak is not included in science data products which are generated using MLUTs, which filter the mass resolution down to 64 mass bins and throw away events in the high mass tail.

Figure 34a illustrates anomalous, ghost-peak-like behavior of STATIC when exposed to 17 keV CO_2^+ from the Colutron gun in discharge mode (red) and filament mode (black). The black curve consists of ions with an initial energy of 5 keV and -12 kV of TOF acceleration, whereas the red curve has 2 keV initial energy and -15 kV of TOF acceleration. The primary CO_2^+ peak is at bin 540 and matches for the two cases. The slightly broader red curve is due to a high beam flux which broadens the mass peaks as discussed earlier. The two small peaks seen just below TOF bin 200 appears to be sputtered ions (or dissociated ions that have lost their primary energy when striking the exit grids) since their time-of-flight scales with the square root of the TOF voltage. Similar sputtered ions are present in Fig. 33 for N_2^+. Sputtered ions may be produced by the primary ions striking the grids, or by secondary electrons generated at the Start foil and accelerated back to the ESA. These latter 12–15 keV electrons can sputter residual gas from surfaces, which accelerates into the TOF. The location of the peaks is consistent with O^{++}.

The more important feature in Fig. 34a is the broad, double humped shoulder between TOF bin 200 and 400. Since the two curves are coincident and do not shift with TOF accelerations of -12 kV (black) and -15 kV (red), these events are not sputtered ions. Figure 34b shows mass spectra of a 5 keV CO_2^+ beam with TOF accelerations of -11 and -15 kV. The shoulders shift with the total ion energy, again suggesting these events are tied to the beam energy as might be expected for ghost peaks. At the time of this publication we have no definitive explanation of the shoulders, although they appear to be similar to the N_2^+ shoulders seen in Fig. 33. As with N_2^+, we suspect they are due to dissociation and charge exchange at the ESA exit grid, producing lower mass and higher charge state ions. The observed rate for these low mass shoulder events are about 6 % to 7 % of the total rate.

4 Measurements and data products

STATIC cycles through its entire 64 energy step range once every four seconds. At each energy step, STATIC pauses and sweeps the deflectors over their full angular range (16 deflection steps). At each of the 1024 energy-deflector steps, raw particle events are decoded by their values of bA, bB, bC, bD, TA > TB, TC > TD, TA-TC, TB-TD, |TA-TB|, |TC-TD|, and recorded in a set of intermediate arrays in the instrument's SRAM. bA, bB, bC, bD are digital bit signals (0/1) signifying an event in preamp A, B, C, D (see Fig. 2) during a programmable timing interval (typically set to 160 ns) after the first timing event. TA, TB, TC, TD are event times for preamps. TA > TB and TC > TD are digital bit signals (0/1) recording which signal arrived first, and TA-TC, TB-TD, |TA-TB|, |TC-TD| are the actual TOF and Position timing signals generated by the TDC circuits (Fig. 2). The decoding of raw events is programmable, typically rejecting any event where bA, bB, bC, or bD are missing or where TOF values (TA-TC and TB-TD) and Position values (|TA-TB| and |TC-TD|) signals do not agree within a programmable difference (typically $\sim$ 1 ns). The

programming is also flexible enough to allow measurements should one of the preamplifiers or TDC circuits fail, albeit with poorer noise rejection.

Once an event is validated, its TOF and Position values are used to increment a series of arrays in the instrument. The arrays are double-buffered allowing a complete 4 second measurement to be completed while the previous measurements are read out. The TOF timing circuits have 10-bit resolution (1024 TOF bins), event Position is 4 bits (16 anodes), and there are 16 deflection steps at each of the 64 energy steps. This results in a measurement array that is 16 Mbytes – too large to transmit. Instead, the instrument sorts these data into smaller arrays by averaging in various dimensions before transmission to the PFDPU. This compression includes a mass look-up table (MLUT) which reduces the 1024 TOF bins to 64 mass bins. The result of this latter compression is "mass", not TOF, since the MLUT accounts for the changes in ion transit time that vary with a particle's initial energy. This allows the instrument to sum over energy without blurring the mass resolution. Upon transmission to the PFDPU, these measurement arrays are further sorted and summed over dimensions before being packaged and transmitted to the spacecraft, or recorded in a PFDPU burst memory.

STATIC can produce 22 different data products, or APIDs (Application Identifiers), with each product tailored to resolve a particular feature of the required measurement set. Column 2 of Table 3 lists the measurement arrays (E = energy, M = mass, D = deflection, and A = anode) that make up the various data products. Depending upon location in the orbit, and the data allocation given by the spacecraft, different combinations of data products and time resolutions can be selected. STATIC's data allocation can vary during the mission depending upon distance from Earth to Mars. Current data rates are characterized as multiples ($\times 1$, $\times 1.5$, $\times 2$, $\times 3.25$, $\times 4.0$, $\times 4.5$) of STATICs baseline rate of 2.2 kbit/s uncompressed. Data compression of this "survey data" is typically a factor of 3 or more, which provides bandwidth for the transmission a similar quantity of higher time resolution "burst data". Even at the lowest data allocation rate ($\times 1$), STATIC will be able to transmit 2 dimensional energy-mass spectra and 3-dimensional energy-angle (22.5°) distributions at the highest cadence (4 seconds) during ionospheric encounters. At higher data allocations, STATIC's 4 second resolution can be maintained for these products at all altitudes. Higher dimensional survey data products (APIDs CC, CE, D0, D2) are always summed over time, and at any one time, only one of these products can be produced. Higher time resolution for these products is achieved with burst data (APIDs CD, CF, D1, D3), where only one of the four APIDs can be recorded at any one time.

Columns 3 to 8 in Table 3 lists anticipated time resolution in seconds for STATIC data products during $\times 1$ and $\times 4.0$ data allocation rates. Cruise phase data was collected at $\times 1$ and $\times 3.25$ rate, and data rates were increased to $\times 4.0$ at Mars. These are preliminary time resolutions. Data products selections will likely evolve over time as the mission proceeds and as we attempt to optimize the science for our limited data return. At the present, we anticipate maintaining a relatively high data rate of $\times 4.0$ for all of the prime mission. Data product resolution is always 4 seconds $\times 2^{\mathrm{N}}$, where N is a non-negative integer. A subset of data products are sent that depend on the operating mode (Ram, Conic, and Pickup), and modes are selected by altitude and/or location during the orbit. Ram mode is used at periapsis (typically < 200 km), Conic mode adjacent to periapsis ($\sim$ 200–800 km), and Pickup mode for the majority of the orbit. The software is flexible allowing new modes with different data product combinations and different time resolutions to be developed.

Data that are not continuously collected include events packets (APID D6), which contain a set of raw event data (event timing codes) used for diagnosing the sensor, and Fast housekeeping (APID D7), which is used for diagnosing high voltage sweeps and offsets.

Table 3 Typical STATIC Data Products (APIDs) and time resolution (sec)

APID	Description	×1 rate			×4 rate		
		Ram	Conic	Pickup	Ram	Conic	Pickup
2A	Housekeeping	32	32	32	32	32	32
C0	64E × 2M	4	4	16	4	4	4
C2	32E × 32M						
C4	4E × 64M						
C6	32E × 64M	4	4	64	4	4	4
C8	32E × 16D	4	4	64	4	4	4
CA	16E × 4D × 16A	4	4		4	4	4
CC	32E × 32M × 8D	64			16		
CD	32E × 32M × 8D	4			4		
CE	16E × 16M × 4D × 16A		64			32	
CF	16E × 16M × 4D × 16A		4			4	
D0	32E × 8M × 4D × 16A			512			128
D1	32E × 8M × 4D × 16A			16			16
D2	32E × 8M × 16A						
D3	32E × 8M × 16A						
D4	2M × 4D × 16A			16			4
D6	Events	2700	2700	2700	2700	2700	2700
D7	Fst Hkp						
D8	Rate1	4	4	4	4	4	4
D9	Rate2	128	128	128	128	128	128
DA	Rate3	4	4	4	4	4	4
DB	1024M	64	64	256	4	4	64

Rate packets (D8, D9, D10) are used for dead time and MCP droop corrections and to determine TOF efficiency. Mass histograms (DB) are used for evaluating sensor operations and for high resolution TOF observations. We anticipate the most useful science data products to be APID C0, C6, C8, CA, CC, CE, D0 and D4. Most other data products are either diagnostic (2A, D6, D7, D8, D9, DA, DB) or are not expected to be used (C2, C4, D2, D3). APID CD, CF and D1 are just higher time resolution versions of APID CC, CE, and D0 that come down during selected burst intervals.

5 Operational modes

Due to the flexibility built into STATIC's design, operational modes become a complex matrix that depend on spacecraft data allocation (×1, ×1.5, ×2, ×3.25, ×4, ×4.5), on data product selection (APIDs), on data product time resolutions, on energy sweep tables, on attenuator state, and on instrument pointing as determined by the APP. The data product arrays listed in Table 3 are independent of energy sweep and deflection sweep, which are programmed with Look Up Tables (LUTs) that are loaded into the instrument by the PFDPU. These LUTs vary with instrument mode (Ram, Conic, and Pickup) and will likely change over time as operations are refined. Preliminary energy sweep tables for Ram, Conic and Pickup modes have logarithmic sweeps spanning energy ranges of 0.1–50 eV, 0.1–500 eV,

and 0.2–30000 eV, respectively. Preliminary deflection ranges are $+/-22.5°$ for Ram mode, and $+/-45°$ for Conic and Pickup modes. Other modes include Scan and Eclipse modes (variations on Pickup mode), and a Protect mode (25–30000 eV) used to prevent detector saturation during telemetry contacts where the APP is not pointed.

Data products are independent of the attenuator states of the sensor, which are used to reduce ion fluxes and prevent detector saturation as the spacecraft passes through periapsis. STATIC has a mechanical (M) and electrostatic (E) attenuator, which have factors of 100 and 10 for levels of attenuation, respectively. The mechanical attenuator extends over 180° centered on the ram direction, and the electrostatic attenuator only operates at low energies (< 15 eV). The four attenuator states ME = 00, 01, 10, &11, produce four different levels of attenuation in the ram direction (1., 1/10, 1/100, 1/1000) at low energy and are expected to be primarily used during Ram and Conic modes. The attenuator is controlled by the PFDPU which monitors the count rate and increments the attenuation up or down by factors of 10 as peak count rate exceeds, or drops below, programmable thresholds. The nominal peak count rate for increasing attenuation is ~ 200 kHz, and attenuation is reduced when the peak rate drops below ~ 8.4 kHz. The attenuator algorithm in the PFDPU includes two parameters, an averaging parameter to add hysteresis, and a cadence parameter to determine how often to test against the thresholds. In addition, mechanical attenuator changes are limited to no more than once every 5 minutes.

Information about the energy and deflector sweeps, the attenuator state, and data product time resolution are encoded into the APID headers to allow proper decoding of data on the ground. The headers also include information to designate diagnostic mode operations, the state of the test pulser (on/off), and packet number when multiple packets are assembled to make a product.

During normal operations, STATIC operates continuously throughout the orbit. The STATIC EM unit was demonstrated to operate properly, with full high voltage, at a pressure of 5×10^{-4} Torr during vacuum chamber tests. This provides an order of magnitude margin over the highest pressures anticipated during deep dips into the Martian ionosphere (125 km altitude). STATIC operates autonomously with a redundant 3 wire command-data-clock interface to the PFDPU, redundant power (+28 V and 28 Return), and mechanical actuator power. STATIC also contains heaters and thermistors which are controlled and monitored by the spacecraft, and a one-time cover opening circuit that was actuated a few months after launch.

STATIC is powered-on by a spacecraft command to the PFDPU, which provides low voltage (LV) regulated +28 V to STATIC. The PFDPU then runs STATIC's LV (low voltage) RTS (relative time sequence) initialization that commands the experiment, loads tables, and leaves STATIC in a low data rate mode. The initialization sequence begins with a "disable STATIC HV RTS" command to prevent high voltage turn on while the LV initialization sequence is running, and ends the command sequence by enabling STATIC's HV RTS. The initialization sequence also arms the PFDPU logic that controls STATIC's attenuator. High voltage is turned on by sending a command to the PFDPU to arm STATIC's HV. The HV RTS consists of a command sequence that brings up the three HV supplies (Sweep-Deflector HV, MCP HV, −15 kV TOF HV) to nominal voltage over a ~ 3 minute sequence. STATIC is then commanded into a nominal mode (typically Protect mode).

The various operational modes of STATIC are controlled by mode RTSs stored in the PFDPU. A mode RTS command will initiate is a sequence of commands that configure STATIC and determine which data packets are sent, the time resolution of those data packets, the energy-deflector sweep table to be used, and the attenuator thresholds. During an orbit, the spacecraft will initiate mode RTS commands to configure STATIC to Ram, Conic

and Pickup modes, with timing of the commands depending upon the phase of the orbit. During a mode command sequence, data products may be corrupted as the instrument configuration is changed. Mode RTS commands have been organized to minimize these problems, and should result in the loss of no more than a single 4 second measurement. Mode RTSs will be modified over the mission to account for changes in link margin data rates ($\times 1$, $\times 1.5$, $\times 2$, $\times 3.25$, $\times 4.5$) and to optimize science return as we learn more about the Martian environment.

6 Ground data processing

MAVEN level zero (L0) raw data files are processed by automated ground software to generate level 2 (L2) files in Common Data Format (CDF). The naming convention is "mvn_sta_l2_id_yyyymmdd_vxx_rxx.cdf", where "id" is an identifier that includes the APID and a measurement descriptor (for example: id = 'c6-32e64m', for APID C6 which has 32 energies and 64 masses), and where vxx and rxx are software version and data revision number. L2 files are compressed CDF files that not only contain the calibrated data in physical units, but also the raw data (counts), the calibration arrays, background event arrays, dead time correction arrays (including corrections for detector droop), FOV blockage arrays, and information about instrument mode and attenuator state. Inclusion of all the raw data means that no information is lost in the L2 production allowing users to evaluate statistics, check for measurement errors, and/or separately develop their own calibration code. The files also include some generally useful information about spacecraft position and orientation, spacecraft potential, and average magnetic field during a measurement interval.

We note that for data products that sum over FOV (APIDs C0, C2, C4, C6, C8, CC, CD), assumptions must be made about the geometric factor used in calculating fluxes (physical units) from count rate. Since the attenuators are not uniform over look direction, and because the sensor FOV has time varying blockage by the spacecraft, assumptions must be made about the primary direction where the ions originate. For Ram mode, the assumption will be that events originate in anode 7 which looks in the spacecraft ram direction. For Conic mode, where ions are a bit hotter and where flows may be present, the assumption will be that events originate in anodes 6, 7 and 8, and within 23° of the ram direction. For Pickup mode, ground software will use the full FOV-summed geometric factor. For data products that contain no mass information (APIDs C8, CA), the mass assumption will be protons for data collected in the solar wind or magnetosheath, and O_2^+ for ions below the ionopause. These assumptions will be the basis of automated ground data processing, at least at the beginning of the mission. However, it should always be possible for a data analyst to use measurements from another data product to refine or change the assumptions, if warranted.

MAVEN data analysis software is available to the entire community for analyzing L2 files. The software is IDL (Interactive Data Language) based and requires the SSL UC Berkeley "general" library of routines which were developed for the NASA Wind-3DP mission by Dr. Davin Larson, and adopted by the NASA FAST, THEMIS, and MAVEN missions. The software package is built around a plotting routine called 'tplot', which is a flexible data analysis tool for displaying time series data. The software package also includes routines for a variety of other plotting functions and data calculations such as density and flows. We note that the STATIC data are incomplete because there are holes in the sensor FOV, including blockage by the spacecraft. This means that scientists should use caution when analyzing data, especially when calculating moments. The burden will be on individual scientists to determine whether particle populations of interest completely reside within

the sensor FOV. This may require using other data sets or modeling to test whether the dominant ion populations are fully measured. The data also include quality flags which indicate known problems or limits to the data.

7 Cruise-phase observations of sensor response and background

STATIC's three high voltage (HV) supplies (SWP, MCP, TOF) were exercised two months after launch over a 3 day period. The initial HV turn-on cycled each supply separately up to a working voltage to confirm operation. At the end of the first contact, the −15 kV TOF supply was left on for a 12 hour period to enhance the clean-up of any field emission and ion feed-back due to residual gas on TOF surfaces. The following day, the supplies were slowly cycled up to nominal voltages. The MCPs had initial background rates of ∼ 5 kHz, an order of magnitude larger than expected, however this background cleaned up over several hours to more nominal ∼ 200 Hz rates as the MCPs scrubbed. Residual bursts of enhanced background counts were observed over the first few weeks of operation as the MCPs continued to scrub. Following the second day's HV turn-on, the MCPs were again turned off and the −15 kV supply left on for the 12 hours between contacts. On the third day, after the supplies were slowly initialized, the spacecraft was oriented to point STATIC's ram FOV (mechanical attenuator closed) toward the sun where it detected the solar wind for several hours. After this initial turn-on, STATIC was shut down while MAVEN spacecraft testing was completed. Two months after this initial turn-on, STATIC was activated using the automated onboard turn-on sequence planned for Mars which ramps each high voltage to its nominal value in about 1 minute. STATIC was then operated for several months detecting solar wind ions. Results of this inflight testing, and the resulting knowledge gleaned from these data, are described in this section.

Figure 35 shows a five day period early after the second high voltage turn-on while STATIC was pointed into the solar wind. The mechanical attenuator was closed to prevent sensor saturation. The upper 4 panels show (a) proton (blue) and alpha (green) density, (b) solar wind speed, (c) proton temperature in the flow direction, (d) proton pressure. These calculated solar wind parameters were derived from the energy-mass spectra (no angle information) using preliminary calibrations. Data were smoothed with a two minute averaging. Panel (e) shows typical valid events rates were only ∼ 100 per 4 second sweep interval. The majority of these events were observed in one or two 3.8 ms samples with peak count rates of ∼ 10 kHz. Panels (f) and (g) are energy and mass spectrograms that show prominent proton peaks. The bottom panels illustrate that the solar wind events occur in a single 22.5° anode bin and single 22.5° deflection bin.

The early inflight calibrations were used to diagnose and characterize proton and alpha straggling. This characterization is important because tenuous pickup ions will be measured in the presence of intense solar wind fluxes both in the Martian magnetosheath and in the unshocked solar wind. Cruise phase solar wind observations, with the mechanical attenuator closed, provided a low-count-rate, energy-separated proton beam that allowed long periods of integration to extract measurements of the high mass tail of straggled counts. Figure 36 illustrates proton and alpha straggling observed after launch, similar to that observed during ground calibrations seen in Fig. 32b. The cut through the straggled protons on March 20, 2014 at 457 eV (black) is virtually identical to a similar cut through 1115 eV protons 4 days later (red). The curves are scaled by the total counts in the proton peak for comparison. The green and cyan curves show a similar straggling behavior in alphas after contributions from protons have been removed. The small secondary peaks at mass 3 in the protons, and

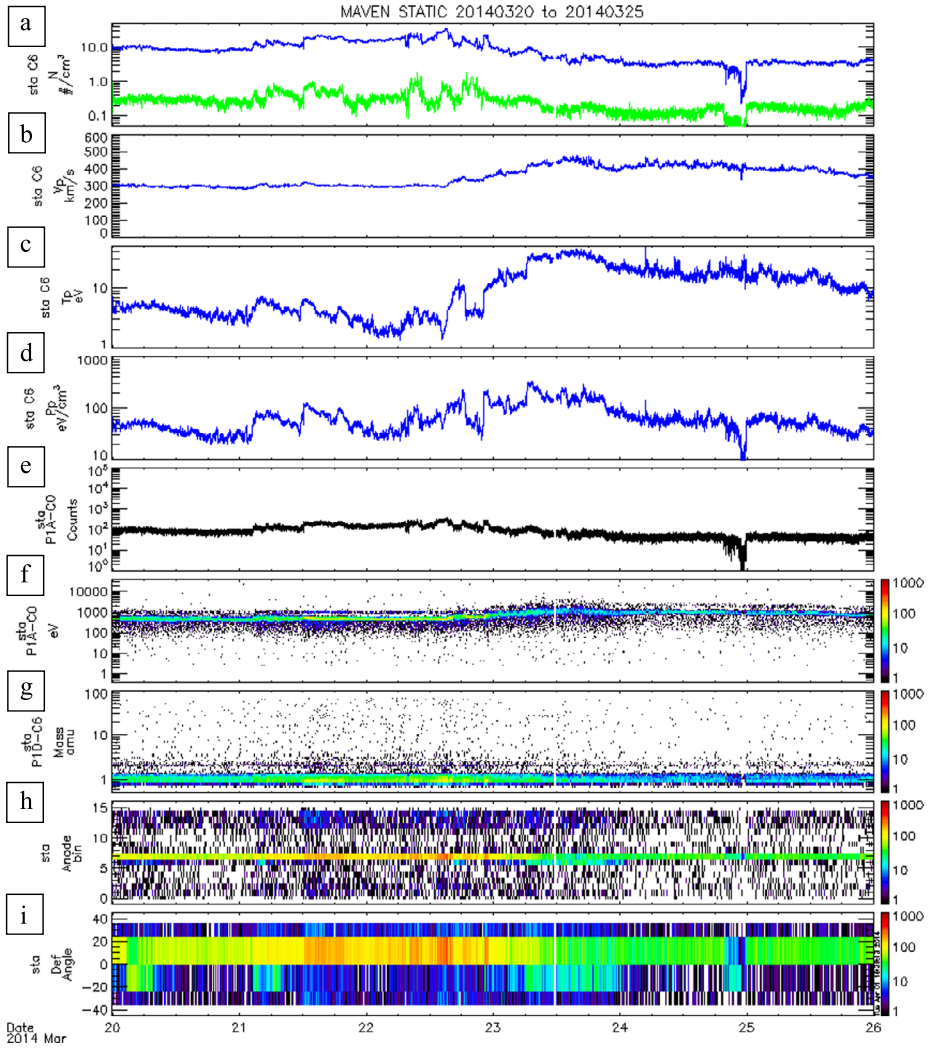

Fig. 35 STATIC cruise phase data with preliminary calibrations. (**a**) density protons (*blue*) and alphas (*green*), (**b**) proton velocity, (**c**) proton temperature in the flow direction, (**d**) proton pressure, (**e**) counts per 4 second sweep, (**f**) energy spectrogram, (**g**) mass spectrogram, (**h**) anode bin spectrogram, (**i**) deflection spectrogram. The top 4 panels include 2 minutes averaging

mass 5 in the alpha curves, match those observed during ground calibrations (Fig. 32b) and discussed in Sect. 3.7. As shown in the figure, the shape of the high-mass tail appears to be independent of count rate and initial ion energy indicating a background subtraction algorithm could be used to further reduce any cross-contamination.

A background subtraction algorithm to remove straggling is illustrated in Fig. 37. Figure 37a shows energy-mass spectra averaged over a day, before background subtraction. Solar wind protons form the prominent peak centered at mass ~ 1 and energy ~ 500 eV. The vertical finger of counts that spans masses 2 to 60 at energy ~ 450 eV are due to proton straggling. Note that the color scale spans 5 orders of magnitude in counts per TOF bin.

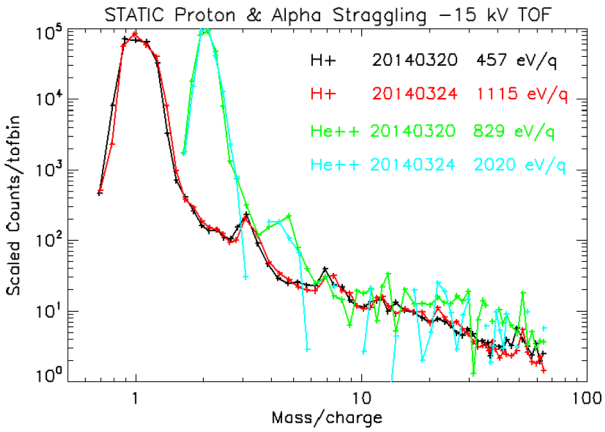

Fig. 36 Proton and alpha TOF straggling in the solar wind, similar to ground test data in Fig. 32b. Energy straggling creates a non-physical high-mass tail in the ion mass distribution. Counts are normalized by the number of time-of-flight bins per measurement bin to provide equal time interval binning, and curves are scaled so that the number of events in the primary peak are equal. About 1 % of the nominal proton events fall outside the main peak and into this high-mass tail. *Black* and *red curves* show observed mass distributions from solar wind protons on two different days illustrating the straggling is repeatable and independent of ion energy. *Green* and *cyan curves* illustrate alpha straggling

About 1 % of proton events are stragglers. Figure 37b shows the same distribution after applying a background subtraction algorithm that assumes proton straggling is independent of initial proton energy, and independent of event rate. A similar algorithm was then applied to the alphas producing the corrected mass-energy spectra in Fig. 37b. The successful removal of straggling events indicates that background removal should be possible at Mars for long integrations in the shocked solar wind.

Figure 37b also illustrates several other features of solar wind data and sources of background. Besides the prominent proton peak, alphas and heavy solar wind ions form a diagonal in the plot as expected for flowing cold ions. The finger of protons that extends to the right of the primary peak is a suprathermal proton tail, which can be very prominent near shocks. The low energy protons that extend from 20–300 eV are protons that scattered off the spacecraft. These energy degraded protons entered STATIC from roughly the anti-solar wind direction (see below) and are not attenuated by the mechanical attenuator. The flux of spacecraft scattered ions is ~ 4 orders of magnitude lower than the solar wind; however care may still need to be taken to remove this background. Lastly, the ions below 20 eV are sputtered ions off the spacecraft.

In order to identify the sources of scattered and sputtered ions seen in Fig. 37b, we examined the solid angle distribution of these ions. Energy-degraded and scattered solar wind protons can result from both the spacecraft and analyzer surfaces, including posts and grids in the sensor aperture. The angular distribution of < 250 eV ions is shown in Fig. 38 with a linear scale (a) and log scale (b). The solar wind (not shown) is roughly centered on the plot. The largest background appears on the right side of the plot, where spacecraft surfaces block STATIC's FOV, indicating spacecraft scattered ions dominate. These scattered ions contribute counting rates that are $\sim 3 \times 10^{-3}$ of the peak solar wind rate per anode, or $\sim 3 \times 10^{-5}$ of the solar wind flux when accounting for the 10^{-2} mechanical attenuator. This flux varies with spacecraft orientation and should decrease significantly when the APP boom is deployed. (For these measurements, STATIC was stowed adjacent to spacecraft blankets.)

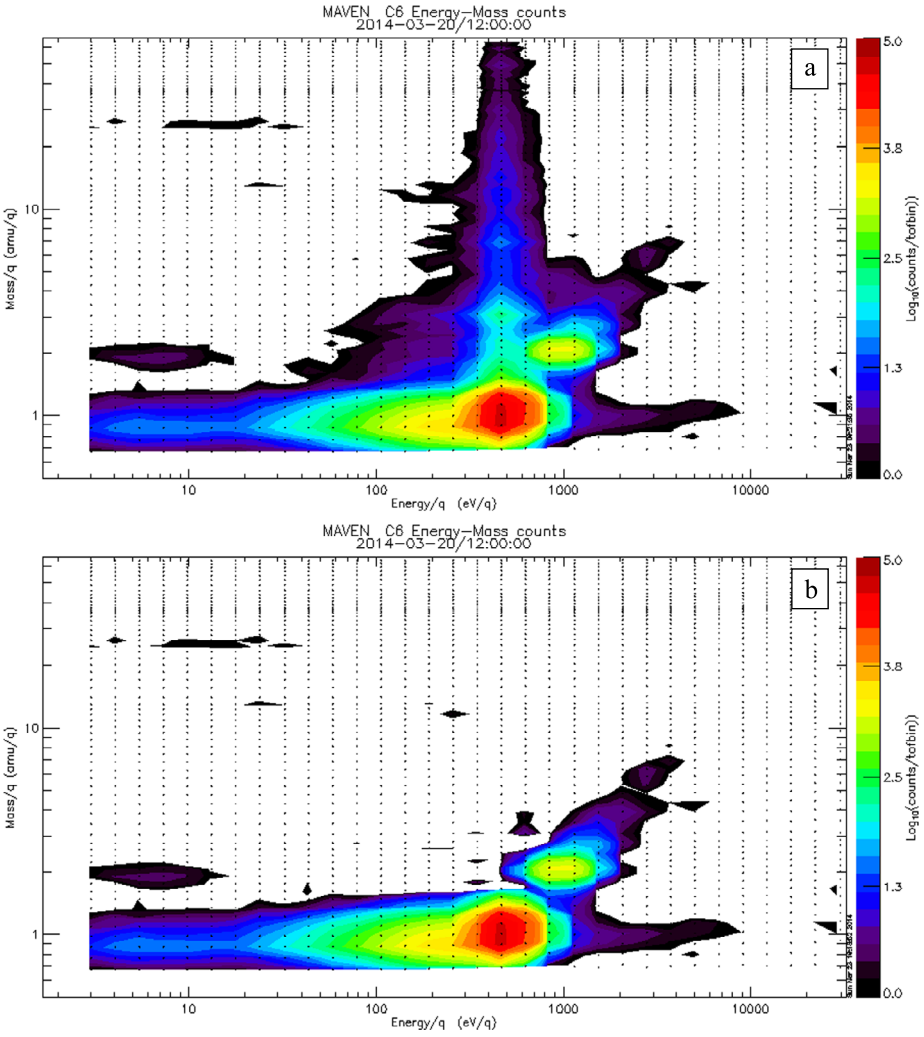

Fig. 37 STATIC mass-energy spectra before (**a**) and after (**b**) subtraction of background due to proton and alpha energy straggling. Such subtractions will be essential to remove invalid events and resolve tenuous pickup ions from the Martian ionosphere. Note that the dynamic range for normalized counts is 10^5. Heavy solar wind ions ($C^{+3}C^{+4}$, $O^{+4}O^{+5}$, Fe^{+10}) extend along a diagonal of constant velocity. Also present is a tenuous suprathermal population of protons extending to 10 keV. Protons between 20 and 200 eV are energy-degraded scattered solar wind protons, and protons below 20 eV are sputtered from surfaces. Sputtering of H_2^+ and heavier ions (not shown, N^+, O^+, N_2^+, O_2^+) was also observed

The second largest contributors to scattered ion background are the aperture posts and grids. These should produce a symmetric left-right backscatter of ions over the figure. Scattered ions from aperture posts and grids are primarily backscattered, with velocities 110°–160° from the solar wind direction. These fluxes are a factor of 3 to 10 times smaller than the largest spacecraft scattered fluxes, or $< 10^{-5}$ of the solar wind flux when accounting for the attenuator. Identification of post/grid scattering is also deduced by a 1–2 order of

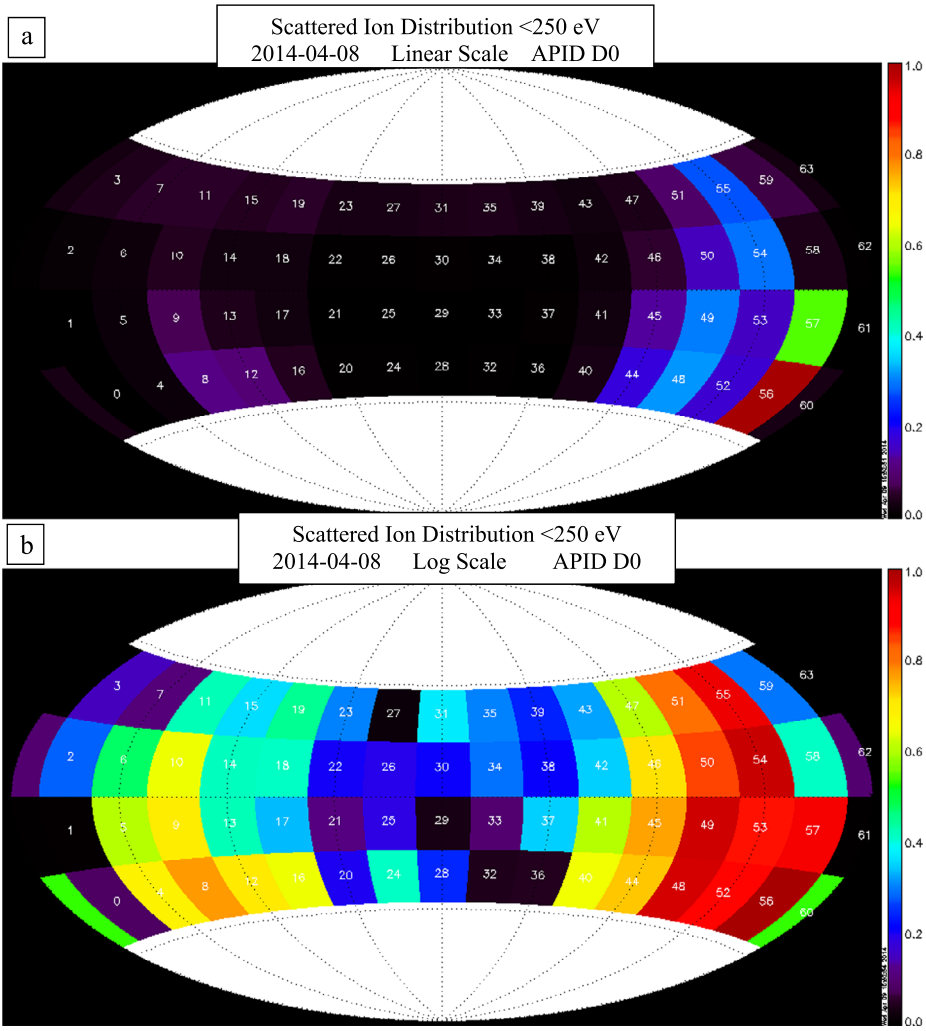

Fig. 38 Angular distribution of scattered solar wind protons into the sensor at energy < 250 eV with STATIC in the stowed on the APP during the cruise to Mars. The solar wind is centered on solid angle bin 30 in the plots. Plots have normalized (**a**) linear and (**b**) log scales. The bulk of the scattered ions are from spacecraft surfaces (*right side* of the plots) and are 4 orders of magnitude lower than the proton peak. Counts on the *left side* result from backscattered ions off the entrance posts and grids and are 5 orders of magnitude below the solar wind peak flux

magnitude drop in backscattered flux in the sector whose post-grids are shadowed from the solar wind by the mechanical attenuator.

A third contributor to energy-degraded protons in Fig. 38 results from forward scattering off internal analyzer surfaces. These energy-degraded ions appear in look directions near the solar wind direction (0°–90°) and include angles where scattering off aperture posts, grids or the spacecraft should be negligible. The counts from these forward scattered ions are only slightly smaller than those from the backscattered posts/grids. These ions appear to be relatively isotropic in anode-look-direction for a given deflection angle, consistent with

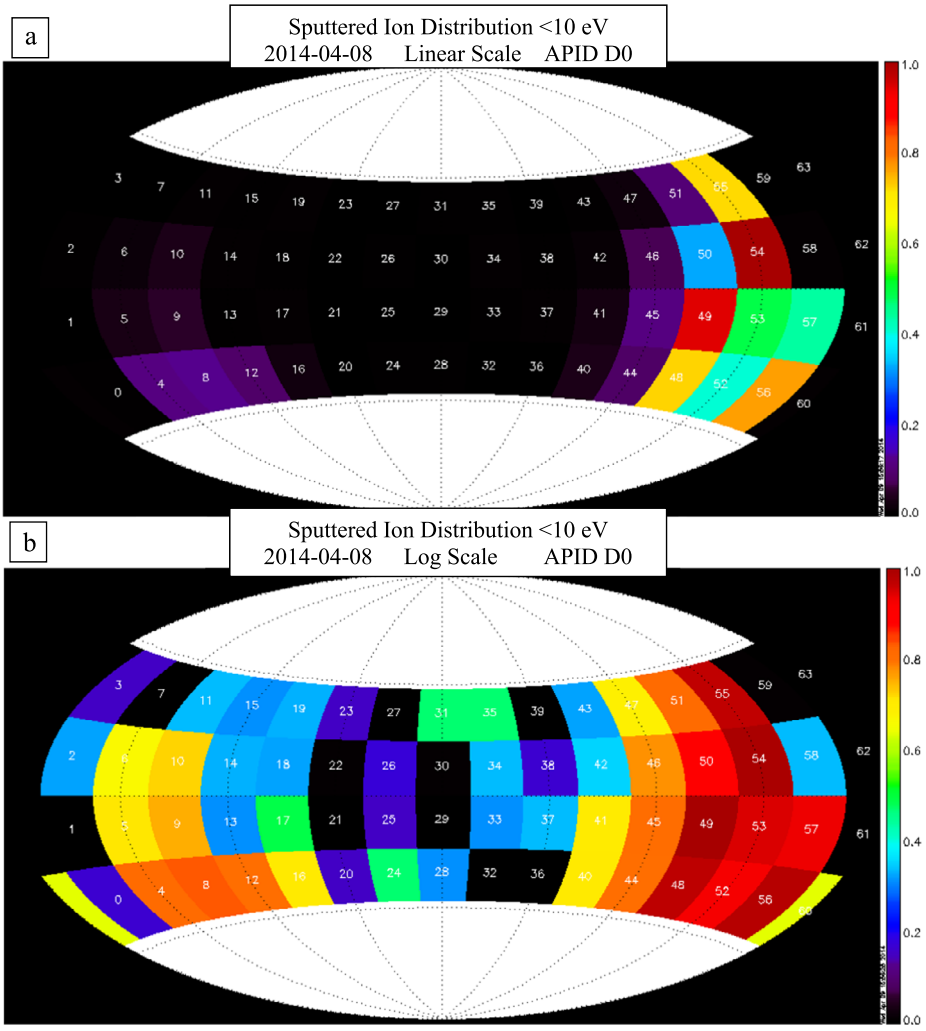

Fig. 39 Angular distribution of sputtered ions at < 10 eV with STATIC in the stowed configuration on the APP boom. The solar wind is centered on *solid angle* bin 30 in the plots. Plots have normalized (**a**) linear and (**b**) log scales. Most of the sputtered ions are protons from spacecraft surfaces (*right side* of plots). Total sputtered ion counts per energy bin are 5 orders of magnitude lower than the solar wind beam, and expected to be 6 orders of magnitude lower once the APP boom is deployed. Sputtered heavies off spacecraft surfaces are 1.5 orders of magnitude lower. The angular distribution and magnitude of sputtering changes with solar wind direction

relatively isotropic scattering of solar wind primaries off internal analyzer surfaces. These ions also have a strong dependence on deflector voltage at energies within factor of 5 of the proton peak. This is again consistent with internal scattering, with deflector voltage affecting which internal surfaces are impacted by primary solar wind ions. At small analyzer energies (10–50 eV), where deflection voltages are small compared to primary proton energies, little or no dependence in flux with deflector sweep phase is observed, again consistent with internal scattering. The fluxes are largest at solar wind incident angles that illuminate the

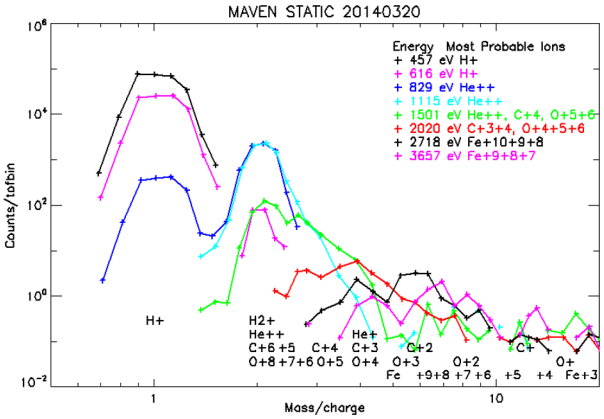

Fig. 40 Constant energy slices through the energy-mass spectra in Fig. 37b for 2014-03-20. Heavy solar wind ions and pickup He+ were observed during transition phase

top-cap. If these ions are produced by internal scattering, then their flux, relative to the measured solar wind, will not decrease when the mechanical attenuator is opened. These ions have a power law count rate spectra between 20 and 200 eV that varies as $\sim E^2$.

The last source of non-solar-wind background is from sputtered ions which are observed at energies less than $\sim$ 20 eV. Sputtered ions should produce a flat count rate up to some characteristic energy (Wurz et al. 2007). They are primarily produced from spacecraft surfaces, not from sensor posts-grids, as deduced from their angular distribution (Fig. 39). Sputtered ions are detected at mass/charge values of 1, 2, and in a tenuous band of 14–32 (not shown in Fig. 37). Mass 2 is likely H_2^+, rather than He^{++} since there is no He^+ signature. Higher mass ions are likely from gases absorbed on surfaces prior to launch (N^+, N_2^+, O^+, O_2^+). Once the APP boom is deployed, and as surfaces clean up with exposure to the solar wind, these sputtered ions are expected to decrease to negligible levels.

STATIC's ability to detect heavy ions in the solar wind is illustrated in Fig. 40. The figure is a set of mass spectra at the indicated energies through the distribution of Fig. 37b. The total heavy ion (M/q > 3) density is $\sim 7 \times 10^{-4}$ cm^{-3}, or $\sim$ 0.07 % of the proton density. Legend along the bottom of the plot indicates locations of various solar wind heavy ions and their charge state. Fitting that includes freeze out temperature could be used to model relative ion densities.

8 Conclusion

The MAVEN STATIC time-of-flight sensor has been operating at Mars for nearly 8 months at the time of this paper's submission. STATIC makes ion composition and distribution function measurements of the cold Martian ionosphere, the suprathermal escaping plasma, and the energetic pickup ions accelerated by solar wind electric fields. STATIC meets its design specification, operating over an energy range of 0.1 eV up to 30 keV, with a base time resolution of 4 seconds, and resolving H^+, H_2^+, He^{++}, He^+, O^+, O_2^+, and CO_2^+ ions. STATIC includes mechanical and electrostatic attenuators which increase its dynamic range by a factor of 10^3, preventing detector saturation when measuring cold ram ions at periapsis, while maintaining adequate sensitivity to resolve tenuous pickup ions. This paper provides an overview of the instrument hardware and the ground calibration of the sensor, discusses sources of non-ideal behavior that contribute to background, describes the data products and operating modes of the experiment, and presents some early measurements during cruise phase to Mars.

Acknowledgements The development of the MAVEN STATIC sensor was supported by NASA NNG-08EK33C. Analysis of cruise phase data was supported by NASA UCO-100001316. We thank Dr. Davin Larson for developing the IDL "tplot" software used to plot STATIC data in this paper, and for all the data analysis tools that he has selflessly provided to the scientific community to support MAVEN and other NASA missions.

References

L.A. Andersson, R.E. Ergun, G.T. Delory, A. Ericksson, J. Westfall, H. Reed, J. McCauly, D. Summers, D. Meyers, Space Sci. Rev. (2015). doi:10.1007/s11214-015-0194-3

S. Barabash et al., Space Sci. Rev. **126**, 113–164 (2006)

S. Barabash, A. Fedorov, R. Lundin, J.-A. Sauvaud, Science **315**(5811), 501–503 (2007). doi:10.1126/science.1134358

D.A. Brain, J.S. Halekas, L.M. Peticolas, R.P. Lin, J.G. Luhmann, D.L. Mitchell, G.T. Delory, S.W. Bougher, M.H. Acuña, H. Réme, Geophys. Res. Lett. **33**, L01201 (2006). doi:10.1029/2005GL024782

A. Burgi, M. Oetliker, P. Bochsler, J. Geiss, M. Coplan, J. Appl. Phys. **68**(6) (1990)

E. Carlsson et al., Icarus **182**, 320–328 (2006)

C.W. Carlson, J.P. McFadden, in *Geophys. Monog.*, vol. 102, ed. by R. Pfaff (Am. Geophys. Union, Washington, 1998)

J.E.P. Connerney, J. Espley, P. Lawton, S. Murphy, J. Odom, R. Oliversen, D. Sheppard, Space Sci. Rev. (2015). doi:10.1007/s11214-015-0169-4

E. Dubinin, R. Lundin, O. Norberg, N. Pissarenko, J. Geophys. Res. **98**, 3991–3997 (1993)

E. Dubinin, M. Fraenz, A. Fedorov, R. Lundin, N. Edberg, F. Duru, O. Vaisberg, Space Sci. Rev. **162**, 173 (2011). doi:10.1007/s11214-011-9831-7

E. Dubinin, M. Fraenz, J. Woch, T.L. Zhang, J. Wei, A. Fedorov, S. Barabash, R. Lundin, Geophys. Res. Lett. **39**, L01104 (2012). doi:10.1029/2011GL049883

J.P. Eastwood, D.A. Brain, J.S. Halekas, J.F. Drake, T.D. Phan, M. Øieroset, D.L. Mitchell, R.P. Lin, M. Acuña, Geophys. Res. Lett. **35**, L02106 (2008). doi:10.1029/2007GL032289

X. Fang, M. Liemohn, A.F. Nagy, J.G. Luhmann, Y. Ma, J. Geophys. Res. **115**, A04308 (2010). doi:10.1029/2009JA014929

A. Fedorov, E. Budnik, J.-A. Sauvaud et al., Icarus **182**, 329–336 (2006)

J.L. Fox, J. Geophys. Res. **108**, 1223 (2003). doi:10.1029/2001JA000203

J.L. Fox, J. Geophys. Res. **114**, E12005 (2009). doi:10.1029/2009JE003432

M. Fraenz, E. Dubinin, E. Nielsen et al., Planet. Space Sci. **58**, 1442 (2010). doi:10.1016/j.pss.2010.06.009

F. Gonzalez-Galindo, J.-Y. Chaufray, M.A. Lopez-Valverde, G. Gilli, F. Forget, F. Leblanc, R. Modolo, S. Hess, M. Yagi, J. Geophys. Res. **118**, 2105 (2013). doi:10.1002/jgre.20150

R.R. Goruganthu, W.G. Wilson, Rev. Sci. Instrum. **55**(12), 2030 (1984)

D.A. Gurnett, R.L. Huff, D.D. Morgan, A.M. Persoon, T.F. Averkamp, D.L. Kirchner, F. Duru, F. Akalin, A.J. Kopf, E. Nielsen, A. Safaeinili, J.J. Plaut, G. Picardi, Adv. Space Res. **41**, 1335–1346 (2008)

J.S. Halekas, E.R. Taylor, G. Dalton, G. Johnson, D.W. Curtis, J.P. McFadden, D.L. Mitchell, R.P. Lin, B.M. Jakosky, Space Sci. Rev. (2013). doi:10.1007/s11214-013-0029-z

H.B. Hanson, S. Sanatani, D.R. Zuccaro, J. Geophys. Res. **82**, 4351 (1977). doi:10.1029/JS082i028p04351

B. Jakosky, R.P. Lin, J. Grebowsky, J.G. Luhmann, D.F. Mitchell, G. Beutelschies et al., Space Sci. Rev. (2015). doi:10.1007/s11214-015-0139-x

D.M. Klumpar, E. Moebius, L.M. Kistler, M. Popecki, E. Hertzberg, K. Crocker, M. Granoff, L. Tang, C.W. Carlson, J. McFadden, B. Klecker, F. Eberl, E. Kunneth, H. Kastle, M. Ertl, W.K. Peterson, E.G. Shelly, D. Hovestadt, Space Sci. Rev. **98**, 197 (2001)

D.E. Larson, R.J. Lillis, C. Lee, P. Dunn, K. Hatch, M. Robinson, D. Glaser, J. Chen, D. Curtis, C. Tiu, R. Lin, J.G. Luhmann, B. Jakosky, Space Sci. Rev. (2015). doi:10.1007/s11214-015-0218-z

R. Lundin, E. Dubinin, Adv. Space Res. **12**(9), 255 (1992)

R. Lundin, A. Zakharov, R. Pellinen, S.W. Barabasj, H. Borg, E.M. Dubinin, B. Hultqvist, H. Koskinen, I. Liede, N. Pissarenko, Geophys. Res. Lett. **17**, 873–876 (1990)

P.R. Mahaffy, M. Benna, T. King, D.N. Harpold, M. Barciniak, M. Bendt et al., Space Sci. Rev. (2015). doi:10.1007/s11214-014-0091-1

M. Matta, P. Withers, M. Mendillo, J. Geophys. Res. **118**, 2681 (2013). doi:10.1002/jgra.50104
W. McClintock, N. Schneider, I. Stewart, G. Holsclaw, J. Clarke, F. Montmessin, R. Yelle et al., Space Sci. Rev. (2015). doi:10.1007/s11214-014-0098-7
J.P. McFadden, C.W. Carlson, in *Geophys. Monog.*, vol. 102 ed. by R. Pfaff (Am. Geophys. Union, Washington, 1998)
J.P. McFadden, C.W. Carlson, D. Larson, M. Ludlam, R. Abiad, B. Elliott, P. Turin, M. Marckwordt, V. Angelopoulos, Space Sci. Rev. (2008). doi:10.1007/s11214-008-9440-2
D.L. Mitchell, C. Mazelle, J.A. Sauvaud, D. Toublanc, J.J. Thocaven, J. Rouzaud, A. Federov, E.R. Taylor, M. Robinson, P. Turin, D.W. Curtis, Space Sci. Rev. (2015, submitted)
A. Muller, N. Djuric, G.H. Dunn, D.S. Belic, Rev. Sci. Instrum. **57**(3) (1986)
T. Penz, N.V. Erkaev, H.K. Biernat, H. Lammer, U.V. Amerstorfer, H. Gunell, E. Kallio, S. Barabash, S. Orsini, A. Milillo, W. Baumjohann, Planet. Space Sci. **52**, 1157 (2004). doi:10.1016/j.pss.2004.06.001
R. Ramstad, Y. Futaana, S. Barabash, H. Nilsson, S.M. del Campo, B.R. Lundin, K. Schwingenschuh, Geophys. Res. Lett. **17**, 873–876 (2013)
H. Rème, J.M. Bosqued, J.A. Sauvaud, A. Cros, J. Dandouras, C. Aoustin, J. Bouyssou, Th. Camus, J. Cuvilo, C. Martz, J.L. Médale, H. Perrier, D. Romefort, J. Rouzand, C. d'Uston, E. Mobius, K. Crocker, M. Granoff, L.M. Kistler, M. Popecki, D. Hovestadt, B. Klecker, G. Paschmann, M. Scholer, C.W. Carlson, D.W. Curtis, R.P. Lin, J.P. McFadden, V. Formisano, E. Amata, M.B. Bavassano-Cattaneo, P. Baldetti, G. Belluci, R. Bruno, G. Chionchio, A. DiLellis, E.G. Shelley, A.G. Ghielmetti, W. Lennartsson, A. Korth, H. Rosenbauer, R. Lundin, S. Olsen, G.K. Parks, M. McCarthy, H. Balsiger, Space Sci. Rev. **79**, 303 (1997)
S.M. Ritzau, R.A. Baragiola, Phys. Rev. B **58**(5), 2529 (1998)
P. Wurz, U. Rohner, J.A. Whitby, C. Kolb, H. Lammer, P. Dobnikar, J.A. Martin-Fernandez, Elsevier (2007). doi:10.1016/j.icarus.2007.04.034
Young et al., Space Sci. Rev. **114**, 1 (2004)